Ph.D. DISSERTATION

Tailored Nanostructures of Metal Oxides and 2D Materials for Selective Chemoresistive Gas Sensors

By

Jun Min Suh

August 2020

SEOUL NATIONAL UNIVERSITY

COLLEGE OF ENGINEERING

DEPARTMENT OF MATERIALS SCIENCE AND ENGINEERING

Tailored Nanostructures of Metal Oxides and 2D Materials for Selective Chemoresistive Gas Sensors

Advisor: Prof. Ho Won Jang

by

Jun Min Suh

A thesis submitted to the Graduate Faculty of Seoul National University in partial fulfillment of the requirements for the Degree of Doctor of Philosophy

Department of Materials Science and Engineering

August 2020

Approved

by

Chairman of Advisory Committee: Jin Young Kim

Vise-Advisory Committee: Ho Won Jang

Advisory Committee: Jeong-Yun Sun

Advisory Committee: Jong-Heun Lee

Advisory Committee: Chong-Yun Kang

Abstract

Tailored Nanostructures of Metal Oxides and 2D Materials for Selective Chemoresistive Gas Sensors

Jun Min Suh

Department of Materials Science and Engineering

The Graduate School

Seoul National University

The development of gas sensor technologies with high sensing performance with low power consumption is one of the most urgent tasks to bring precise gas detection to real life in the Internet of Everything (IoE) era. As the last remaining that has not been mimicked by any electronic devices with overwhelming performance over human sensing receptors among human five senses (touch, sight, hearing, smell, and taste), various efforts on developing electronic nose with gas sensors have been extensively on-going. Although various gas sensor principles have been suggested to mimick and electronically realize human smell senses, the chemoresistive type

gas sensors are the most appropriate candidate sensor principle due to their simple operating mechanism, easy fabrication, and small size which are the primary requirements for IoE applications, not to mention their promising gas sensing properties. Still, lacking gas selectivity and relatively high power consumption need to be overcome and various strategies have been suggested for solving the limitations, such as i) forming nanostructures, ii) catalysts decoration, iii) forming heterojunctions, iv) utilizing alternative materials (metal oxides, 2-dimensional (2D) materials, conductive polymers, or organic-inorganic hybrid perovskites), or v) utilizing alternative activation sources other than external heaters.

This thesis contains various strategies for improving gas selectivity and power consumption of chemoresistive gas sensors based on nanostructured semiconducting materials including metal oxides and transition metal dichalcogenides (TMDs). The nanostructures of semiconducting materials provide a significantly enlarged utilization of surface area in a limited active electrode area.

In Chapter 3, as one of the various strategies to improve gas selectivity of chemoresistive gas sensors, 1-dimensional (1D) nanostructured *p*-type metal oxides having heterojunctions with either *n*-type metal oxides (*p*−*n* heterojunctions of NiO and α-Fe_2O_3) or *p*-type metal oxides (*p*−*p* heterojunctions of Co_3O_4 and NiO) are presented. The multivalent electronic properties of *p*-type metal oxides are expected to exhibit unexpected gas selectivity to various volatile organic compounds. As a result, each heterojunction experimentally exhibited a promising gas selectivity to toluene (C_7H_8) and benzene (C_6H_6) with the extremely high value, respectively. These improvements can be attributed to i) highly porous nanostructures, ii) intrinsic

catalytic effects of the selected metal oxides, iii) depletion layers at the interfaces in each heterojunction, and iv) interesting changes in preferred crystallographic orientation after forming heterojunctions.

In Chapter 4, as one of the various strategies to improve the high power consumption of chemoresistive gas sensors, alternative materials of 2D materials to metal oxides, which do not require high operating temperatures have been adopted. Rather than relying just on the high surface energy of 2D materials for low-temperature operation, 1D nanostructured templates have been adopted for taking full advantage of 2D materials in a limited area. As the first strategy, TMDs including WS_2 and SnS_2 were synthesized on the 1D SiO_2 nanorods template. As the second strategy, already fabricated SnO_2 nanorods were treated with the sulfurization process using a chemical vapor deposition (CVD) system. The first study resulted in extremely sensitive and selective detection of nitrogen dioxide (NO_2) at room temperature, which can be attributed to more exposed edge-sites of TMDs when grown on SiO_2 nanorods template and highly porous nanostructures. The second study resulted in extremely sensitive and selective detection of NO_2 under the extremely humid condition at room temperature, which can be attributed to reduced highly dominant H_2O binding area on SnO_2 nanorods while securing competitive binding sites between H_2O and NO_2 on the sulfurized SnO_2 nanorods for promising NO_2 detection even at highly humid conditions.

In Chapter 5, as one of the various strategies to improve the high power consumption of chemoresistive gas sensors, alternative activation sources of light-emitting diode (LED) to external heaters have been adopted. Although there have

been various reports on the light-activated gas sensors, no studies have been reported on the systematic design of 3-dimensional (3D) nanostructures that can take full advantage of light irradiation on the semiconducting gas sensing materials to the best of the author's knowledge. In this study, 3D TiO_2 nanostructures were fabricated using the Talbot effect of incident light through phase mask and pre-fabricated photopolymer thin film, and successive atomic layer deposition (ALD) of TiO_2. The structural effect and optical effect of 3D TiO_2 nanostructures on the gas sensing properties have been studied with finite-difference time-domain (FDTD) simulation. As a result, extremely sensitive and selective detection of NO_2 at room temperature under ultra-violet (UV) LED irradiation was achieved which can be attributed to systematically designed 3D TiO_2 nanostructures for effective E-field enhancement under light illumination. Furthermore, visible light-activated gas sensing properties have been demonstrated thanks to the highly defective nature of the ALD system.

Keywords: Metal oxide, 2D material, Transition metal disulfide, TMDs, Nanostructure, Heterojunction, Chemoresistive, Gas sensor, Light activation, Room temperature, Selectivity, Power consumption

Student Number: 2014-22519

Table of Contents

List of Figures

List of Tables

Chapter 1

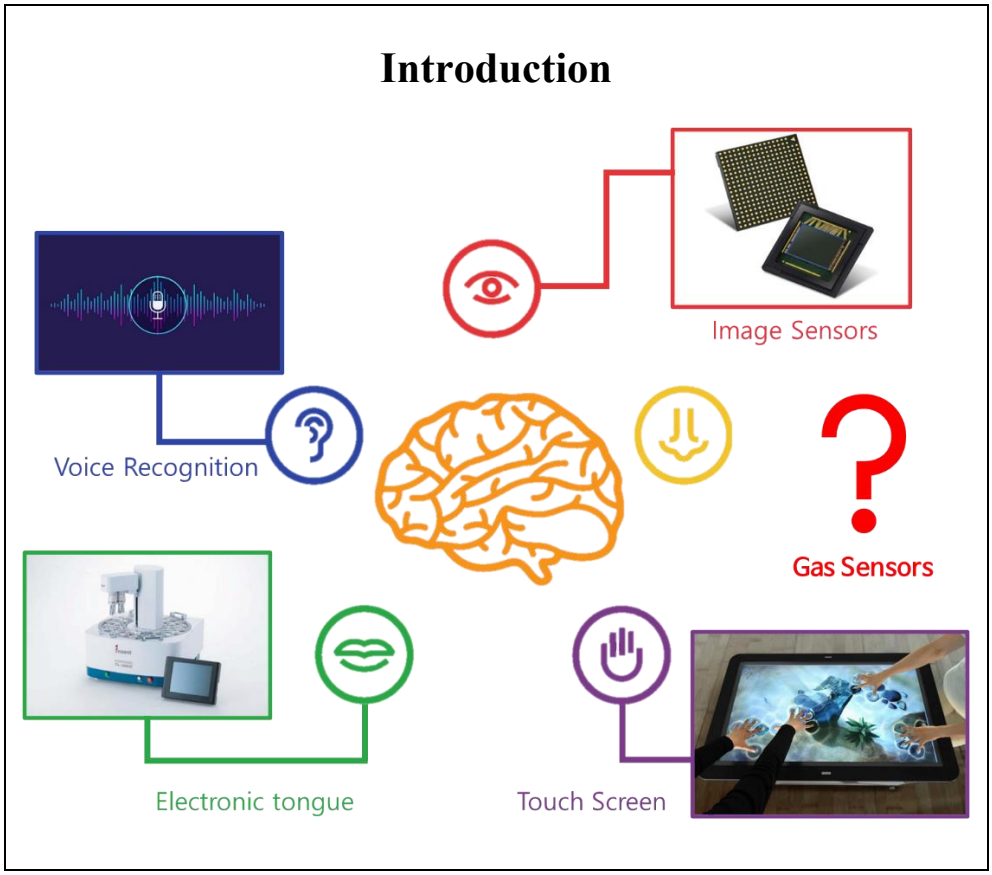
Introduction
Image Sensors
Voice Recognition
Gas Sensors
Electronic tongue
Touch Screen

1.1. Scope and objective of the thesis

For the last decades, a dramatic development in sensor technologies has brought unrealistic enhancement in modern quality of life. Especially, with the emergence of the Internet of Everything (IoE) era, all the sensors have been required to have a small size and low power consumption, not to mention an excellent sensing performance. Therefore, modern people are now surrounded by tons of various sensors and get provided a bunch of helpful information and corresponding functions. The input variables for the developed sensors include various environmental signals from numerous sources in varied conditions. The way the sensors detect those signals can be summarized into mimicking five human senses: touch, sight, hearing, smell, and taste. Among those five senses, touch, sight, and hearing have already been mimicked by cutting edge technologies and settled down as indispensable functions in modern life such as touch screen, image sensors, and voice recognition technologies, respectively.

While those three senses have been mimicked well with way-exceeding performance over receptors in the human body, human taste and smell senses have not yet been exceeded performance-wise by current sensor technologies. Although there have been enormous efforts on the development of the above two, they still lack requirements for the real application into human life compared to already real life-adopted three senses. For example, the taste sensors have actually been developed by several industrial companies with good sensor performance, but their size is far from a portable size and rather close to lab equipment. The smell sensors or the gas sensors are the farthest technology among those mimicking human five

senses from real application due to their complexity in achieving gas selectivity and IoE requirements at the same time. To overcome their limitation, there have been extensive studies on various gas sensor principles including cantilever-based gas sensors, acoustic wave gas sensors, capacitive gas sensors, thermometric gas sensors, optical gas sensors, field-effect transistor gas sensors, colorimetric gas sensors, solid-state electrochemical gas sensors, or electrical-based gas sensors (Figure 1.1).[1-10]

Although many kinds of gas sensor principles and their structures have been suggested, the electrical-based gas sensors are the most appropriate principle considering future applications into IoE devices. The electrical-based gas sensors are also called as chemoresistive gas sensors since their principle is based on changes in electrical resistance upon chemical adsorption and desorption of target gas molecules. The chemoresistive gas sensors have simple structures with easy fabrication method and low cost. They are also small-sized and compatible with existing electrical circuits, which are all the requirements for the IoE applications. Compared to the structure-wise advantages of chemoresistive gas sensors, there still need further efforts on low selectivity and high power consumption. Although there are several other gas sensors principles having strength in selectivity and power consumption, each of them has other critical disadvantages for IoE applications such as high cost in either fabrication or operation, or low stability. Possible strategies include i) forming nanostructures, ii) catalysts decoration[11], iii) forming heterojunctions[12], iv) utilizing alternative materials[13], or v) utilizing alternative activation sources[14] (Figure 1.2).

In this thesis, various nanostructures of semiconducting materials including metal oxides and 2-dimensional materials will be fabricated for the improvement of overall gas sensing performances. In addition, each limitation of chemoresistive gas sensors (low gas selectivity and high power consumption) will be overcome in two different strategies: i) forming heterojunctions (Chapter 3) and ii) utilizing alternative materials (Chapter 4) and activation sources (Chapter 5). The effective nanostructures realized in each case provided a maximized surface area in a limited active area on the electrode substrate for the application of the above strategies. Although improvement of gas selectivity and power consumption was still not achieved at the same time in the studies presented in this thesis, future studies on combining above strategies are certainly plausible and will contribute to the development of gas sensors that overwhelm human receptors for the completion of mimicking human five senses.

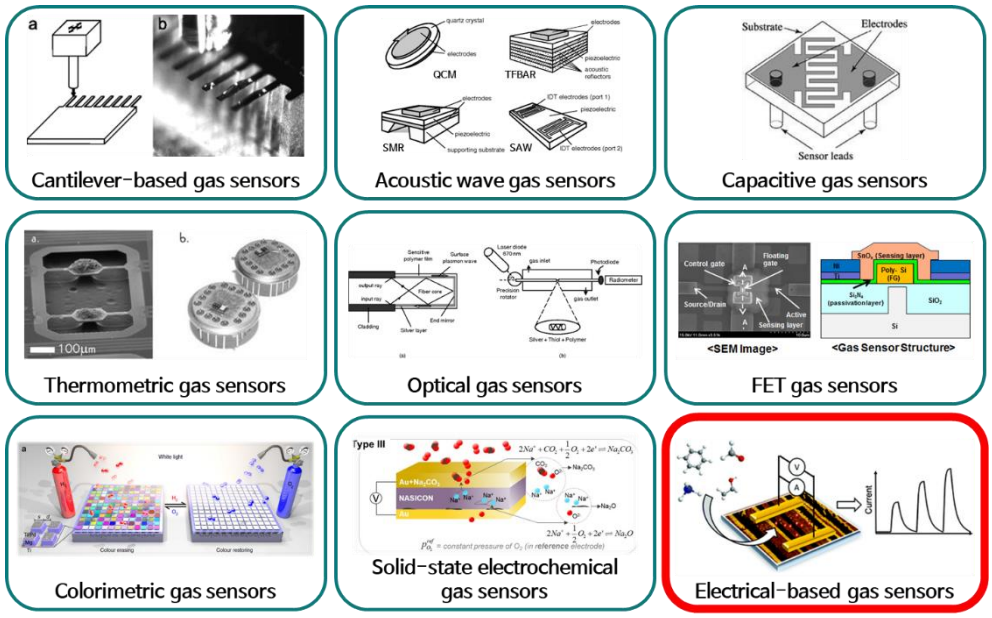

Figure 1.1. Various gas sensor principles and structures.[1-10]

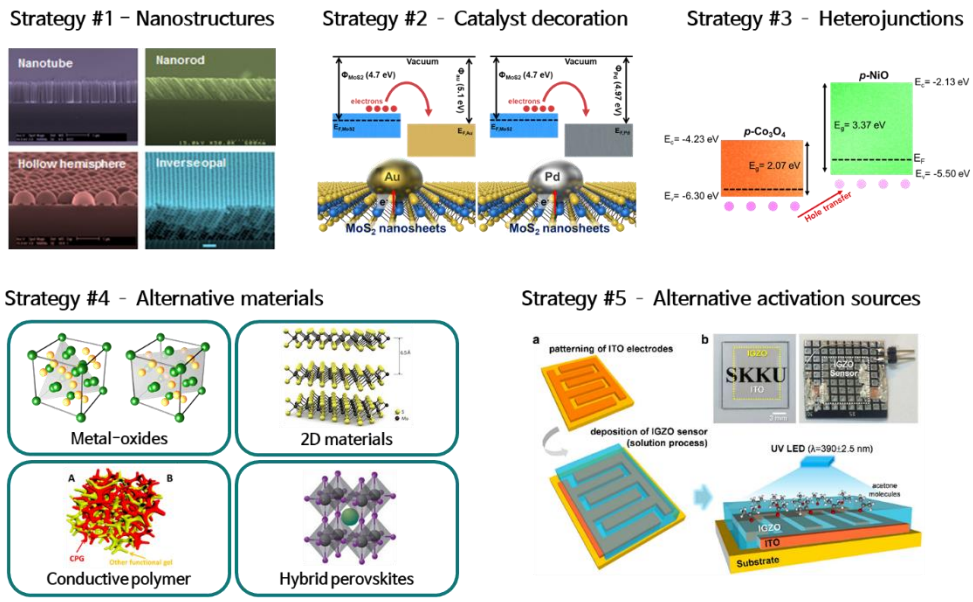

Figure 1.2. Various strategies toward better chemoresistive gas sensing performances.[11-14]

1.2. References

[1] E. Comini, G. Faglia, G. Sberveglieri, *Solid State Gas Sensing*, Springer, Boston, MA, United States **2009**, pp. 47-108.

[2] Y. Sadaoka, *Solid State Gas Sensing*, Springer, Boston, MA, United States **2009**, pp. 109-152.

[3] I. Cacciari, G. C. Righini, *Solid State Gas Sensing*, Springer, Boston, MA, United States **2009**, pp. 209-236.

[4] I. Bársony, C. Dücső, P. Fürjes, *Solid State Gas Sensing*, Springer, Boston, MA, United States **2009**, pp. 237-260.

[5] S. J. Ippolito, A. Trinchi, D. A. Powell, W. Wlodarski, *Solid State Gas Sensing*, Springer, Boston, MA, United States **2009**, pp. 261-304.

[6] H. P. Lang, *Solid State Gas Sensing*, Springer, Boston, MA, United States **2009**, pp. 305-328.

[7] X. Duan, S. Kamin, N. Liu, *Nat. Commun.* **2017**, 8, 14606.

[8] S. Mulmi, V. Thangadurai, *J. Electrochem. Soc.* **2020**, 167(3), 037567.

[9] L. Huang, Z. Wang, X. Zhu, L. Chi, *Nanoscale Horiz.* **2016**, 1, 383-393.

[10] C.-H. Kim, I.-T. Cho, J.-M. Shin, K.-B. Choi, J.-K. Lee, J.-H. Lee, *IEEE Electr. Device L.* **2013**, 35(2), 265-267.

[11] J. M .Suh, Y.-S. Shim, K. C. Kwon, J.-M. Jeon, T. H. Lee, M. Shokouhimehr, H. W. Jang, *Electron. Mater. Lett.* **2019**, 15(3), 368-376.

[12] F. Qu, W. Shang, D. Wang, S. Du, T. Thomas, S. Ruan, M. Yang, *ACS Appl. Mater. Interfaces* **2017**, 10(1), 1050-1058.

[13] F. Zhao, Y. Shi, L. Pan, G. Yu, *Acc. Chem. Res.* **2017**, 50, 1734−1743.

[14] R. Jaisutti, J. Kim, S. K. Park, Y.-H. Kim, *ACS Appl. Mater. Interfaces* **2016**, 8(31), 20192-20199.

Chapter 2

Theoretical Backgrounds

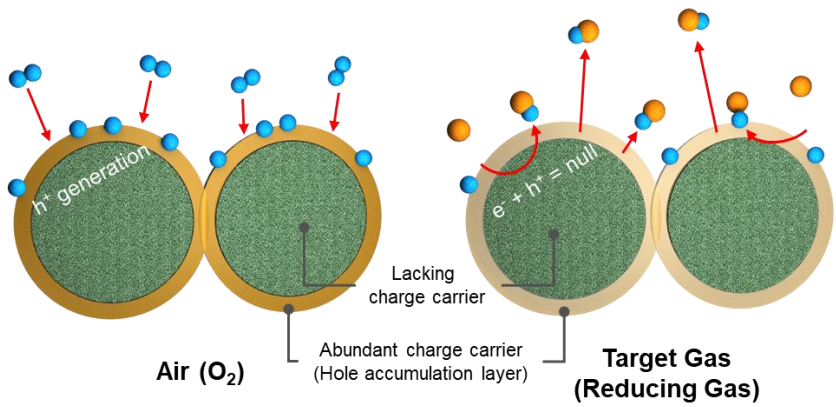

2.1. Principles of chemoresistive gas sensors

2.1.1. Sensing mechanism

The basic operation principle of chemoresistive gas sensors is their current level changes of semiconducting materials upon adsorption and desorption of target gas molecules under a constantly applied voltage. The detailed mechanism of the adsorption and desorption of the target gas molecules on the surface of sensing materials have been controversial, but pre-adsorbed oxygen molecules are widely believed to play a critical role in charge exchange between target gas molecules and the sensing materials. The oxygen molecules in ambient air get absorbed as ionized oxygen species in three different configurations (O_2^-, O^-, or O^{2-}) depending on the operating temperature on the surface of semiconducting sensing materials.[1] When oxygen species are adsorbed, energy band bending occurs at the interface between oxygen and semiconductors as shown in Figure 2.1.[2] Since the energy band bends upward, the electron depletion layer (electron depletion layer for *n*-type semiconductors and hole accumulation layer for *p*-type semiconductors, the further descriptions below assume *n*-type semiconductors) is formed at the interface.[3] When this model is brought to the most common form of sensing materials or granular polycrystalline semiconductors, each grain with an electron depletion layer form junctions at the interface to form double-Schottky barriers as illustrated in Figure 2.2.[2] The height of this double-Schottky barrier plays an important role in the conduction and heavily affect amount of electrical modulation upon gas molecule adsorption and desorption. Therefore, grain size and interfaces of semiconductors are very important and this importance can further be expanded to the nanostructures

of sensing materials (Figure 2.3).[4]

For *n*-type semiconductors, as mentioned before, electron depletion layers are formed at the semiconductor surface at ambient air because electrons are consumed during oxygen ionization and adsorption, leading to an increase in electric resistance. When *n*-type semiconductors are exposed to reducing gases like CH_3COCH_3, C_7H_8, H_2, CO, C_2H_5OH, NH_3, H_2S and CH_4, electrons are released from gas molecules to semiconductors and the degree of band bending decreases, resulting in a decrease of electric resistance. On the other hand, when *n*-type semiconductors are exposed to oxidizing gases like O_2, CO_2, Cl_2, NO and NO_2, electrons are further consumed by gas molecules and the degree of band bending further increases, resulting in expansion of electron depletion layers and increase of electric resistance.[5-6]

For *p*-type semiconductors, since main charge carriers are not electrons but holes, electron depleted environments at the interface are now hole accumulation layer. In other words, charge carriers become abundant as ionized oxygen adsorption happens, leading to a decrease in electric resistance. When *p*-type semiconductors are exposed to reducing gases, electrons are released from gas molecules and they recombine with a hole at the surface to yield an increase of electric resistance. On the other hand, when *p*-type semiconductors are exposed to oxidizing gases, electrons are consumed by gas molecules and a hole accumulation layer becomes thicker and larger to yield a decrease in electric resistance. Theses electric modulation depending on species of main charge carrier (electron or hole) for either *n*-type or *p*-type semiconductors are summarized in Figure 2.5.[7]

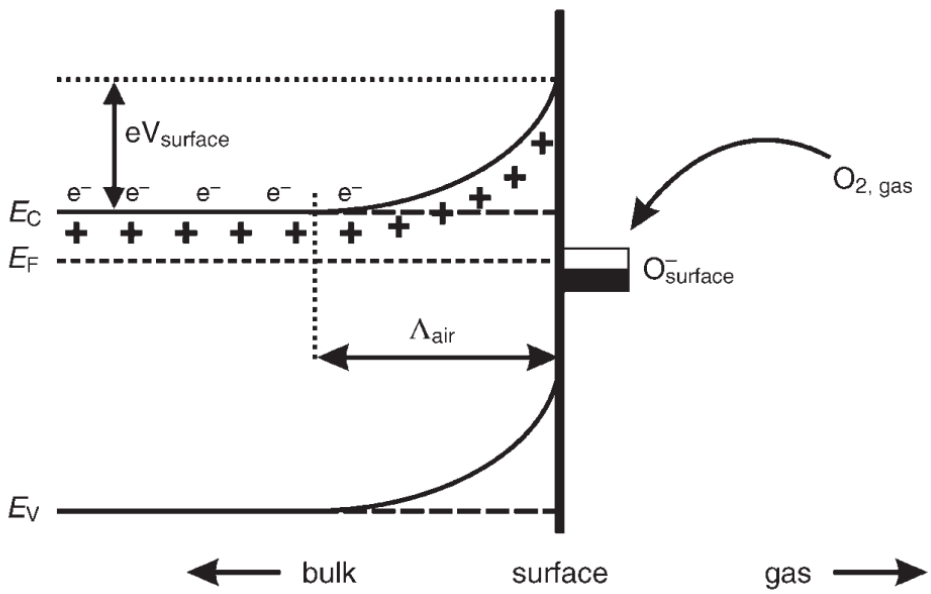

Figure 2.1. Band bending of chemoresistive gas sensing materials upon oxygen adsorption.[2]

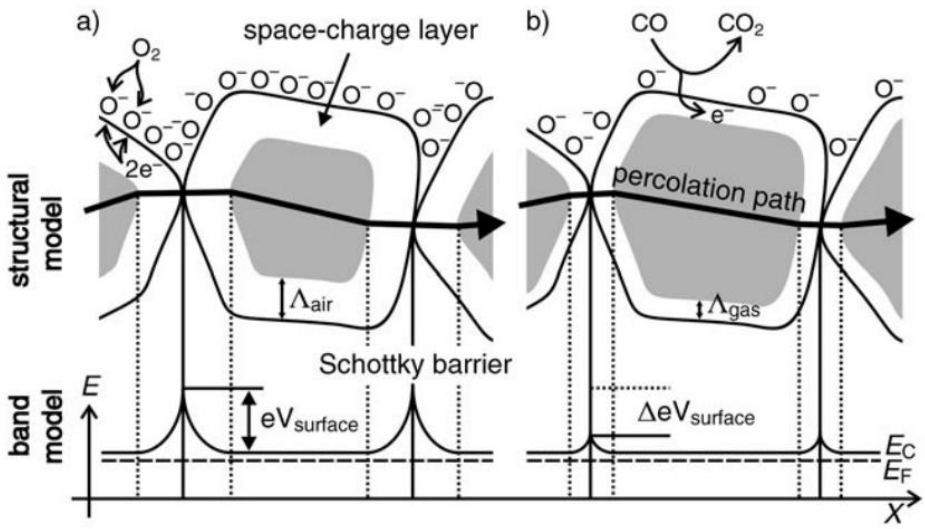

Figure 2.2. Structural and band model of chemoresistive gas sensing materials upon oxygen adsorption. (a) Initial state and (b) after exposure to target gas (CO).[2]

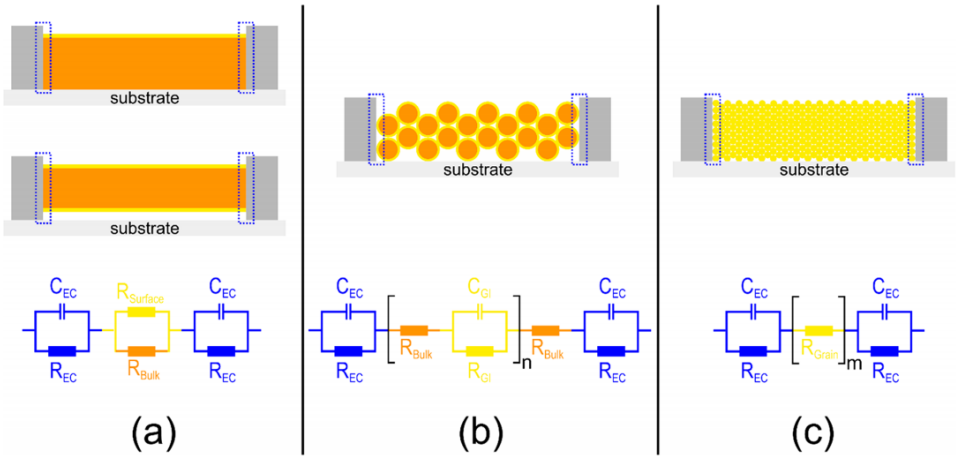

Figure 2.3. Schematics of chemoresistive gas sensors with different material configurations. (a) compact layer (top) and single crystal nanowire (bottom), (b) porous layer with grain radius larger than the Debye length, and (c) porous layer with grain radius smaller than the Debye length with corresponding circuits below.[4]

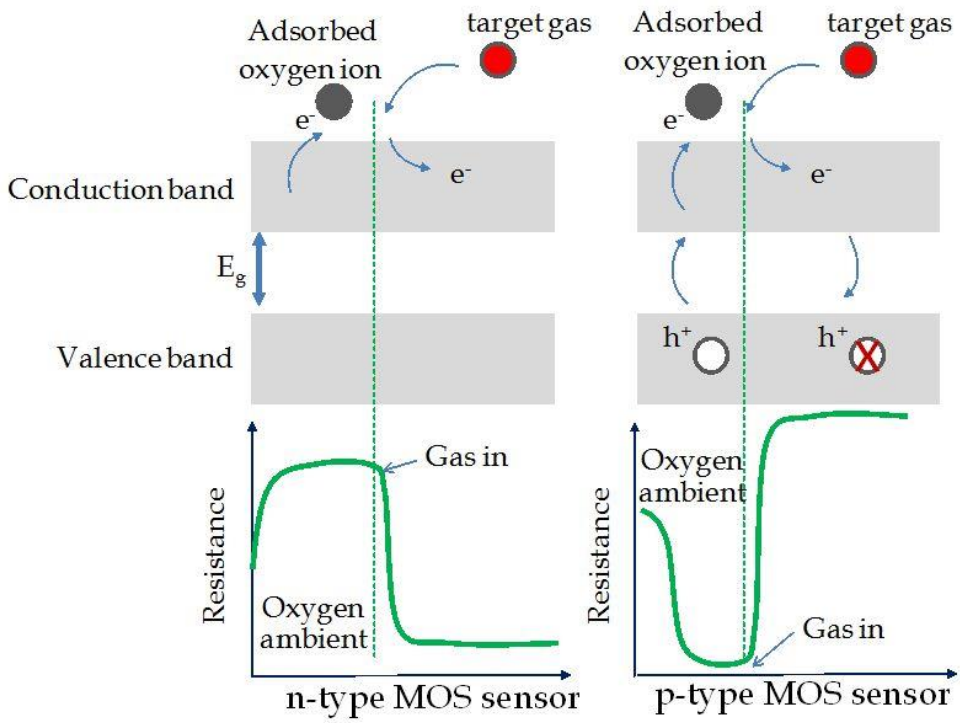

Figure 2.4. Schematic diagram for change of the sensor resistance upon exposure to the target gas (reducing gas) in the cases of *n*-type and *p*-type chemoresistive gas sensors.[7]

2.1.2. Terminologies

Response. Response represents how much sensors respond to the input stimuli. For chemoresistive gas sensors, a gas response can be calculated through a ratio of the measured electrical signal before and after exposure to target gases. The larger response indicated better gas sensing performance.

Sensitivity. Sensitivity represents a degree of response change in respect to change in target gas concentration. In response to gas concentration relationships, a larger slope in the relationship indicates higher sensitivity.

Selectivity. Selectivity represents the ability of chemoresistive gas sensors to distinguish each different gas species through a difference in response value, or data processing.

Stability. Stability represents the ability of chemoresistive gas sensors to reliably operate and produce reproducible electrical sensor signals during multiple exposures to target gases or for a long-term duration.

Detection limit. Detection limit represents the lowest concentration that the chemoresistive gas sensors can detect with meaningful sensor response. There is a concept of theoretical detection limit, where the relationship between response to gas concentration at low concentration range is extrapolated to the lowest possible concentration where signal-to-noise ratio becomes three.[8]

Linearity. Linearity represents the relative deviation of an experimentally measured calibration graph from an ideal linear plot. It also refers to the ability of chemoresistive gas sensors to have only one output value for each input value, which

is the most important parameter for gas sensors to operate properly and practically used.

Response time. Response time represents the time required to reach 90% of resistance change upon exposure to target gas molecules.

Recovery time. Recovery time represents the time required to reach 90% of resistance change upon exposure to ambient air.

2.1.3. Basic factors

The gas sensing properties of semiconducting materials used in chemoresistive gas sensors are affected by three basic factors: i) receptor function, ii) transducer function, and iii) utility factor.[9] Figure 2.5 shows schematic illustrations for receptor function and transducer function.[2] The receptor function represents the ability of semiconducting materials to interact with the target gas molecules. As explained in previous section, interaction with surface of semiconductors with target gas molecules are mediated by ionized oxygen absorbates. In other words, receptor function is strongly related to the amount of ionized oxygen absorbates. Therefore, the receptor function can be improved by surface modification such as metal doping[10, 11], forming heterojunctions[12, 13], noble metal catalyst (Pt, Pd, Au, or Ag) decoration[14], or utilizing surface plasmonic effects[15].

The transducer function refers to the ability of semiconducting materials to electrically modulate during conduction through the interface of each grain, where double-Schottky barrier exist. The height of double-Schottky barrier significantly affect electric conduction of the semiconducting materials and their behaviors upon adsorption and desorption of target gas molecules can dramatically change accordingly. In this aspect, forming additional electron depletion layer or hole accumulation layer can change the height of double-Schottky barrier. When noble metal catalysts are decorated on the surface of semiconductors, electron transfer from semiconductors to catalysts happens and additional electron depletion layers are formed. These properties are called electronic sensitization and chemical sensitization (Figure 2.6).[2] The electronic sensitization refers to the additives on the

surface of semiconductors playing a role of electron acceptors and the change of redox state and chemical state of additives when having reaction with target gas molecules affecting the interface between additives and semiconductors. The chemical sensitization refers to the activation of target gas molecules (e.g. $H_2 \rightarrow 2H$) by additives followed by spillover effects and change of ionized oxygen absorbates concentration.[16, 17]

The utility factor represents the ability of semiconducting materials to provide full access for the target gas molecules to the inner grains of semiconducting materials, which is directly related to the nanostructures of sensing materials. For bulk materials without any nanostructures can utilize only the upper exposed surface of the materials for the participation in chemical reaction with target gas molecules. On the other hand, semiconducting materials with highly porous nanostructures can utilize inner surface of material for the participation in the chemical reaction with target gas molecules. The pore size, thickness of junctions between each gain (inter-neck), and overall film thickness all significantly affect the utility factor. In summary, precise design and control of these three basic factors of semiconducting materials under consideration of target gas species and surrounding target environments can result in high-performance chemoresistive gas sensors with promising sensitivity and selectivity.

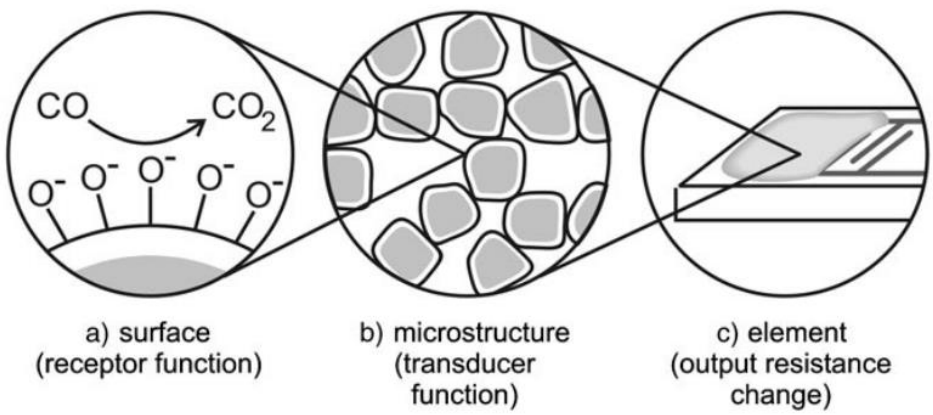

Figure 2.5. Schematic illustration for (a) surface (receptor function), (b) microstructure (transducer function), and (c) element (output resistance change).[2]

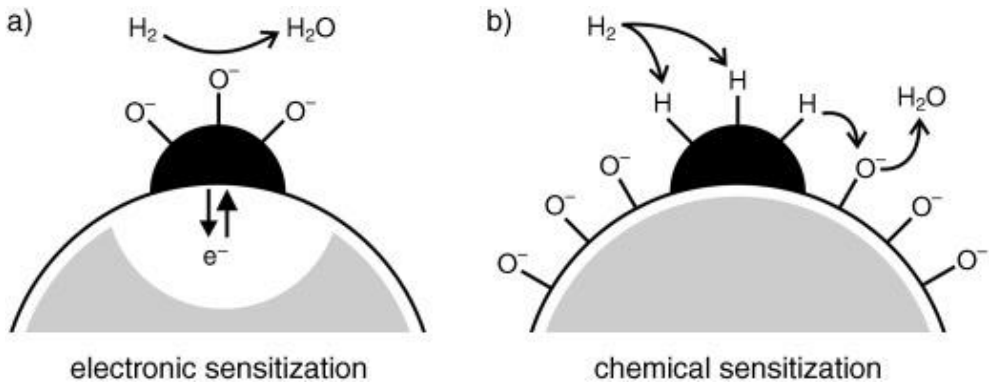

Figure 2.6. Schematic illustrations for (a) electronic sensitization and (b) chemical sensitization.[2]

2.2. Principles of glancing angle deposition

Figure 2.7 shows the schematic diagrams of glancing angle deposition (GLAD) method using e-beam evaporation.[18] Inside the vacuum chamber, the material sources to be evaporated are located at the bottom of the chamber and they are evaporated using thermionically generated electron beam from tungsten filament (Figure 2.7a). Compared to other vacuum deposition techniques like DC sputter, RF sputter, or atomic layer deposition being suitable for conformal coating of the materials, the evaporated vapor of materials during e-beam evaporation has strong directionality and is straightly deposited on the substrate without any conformability.[19] Therefore, when substrate is tilted during deposition, initially deposited nuclei of materials generated shadowed area depending on degree of glancing angles as shown in Figure 2.7b. The evaporated materials are no longer able to be deposited on this shadowed area, resulting in highly porous nanostructures. In respect to the tilted substrate, the materials vapor flux from the bottom of the chamber can be divided into lateral and vertical components. The vertical components will contribute to the vertical growth of the nanostructures or the overall film thickness and lateral components will contribute to the lateral growth of the nanostructures or the obliqueness of the nanostructures as shown in Figure 2.8a. When the tilted substrate experiences a rotation, the lateral components of vapor flux in respect to the substrate are all cancelled out and only vertical components are effective in the deposition of the material vapor, resulting in vertically aligned 1-dimensional nanostructures as shown in Figure 2.8b.[20, 21] Therefore, various 1-dimensional nanostructures with different obliqueness, porosity, diameters, overall

film thicknesses, can be synthesized with the control of glancing angles. Furthermore, precise manipulating in rotation speed can also result in various nanostructures such as zig-zag or helix nanostructures as shown in Figure 2.9.[22]

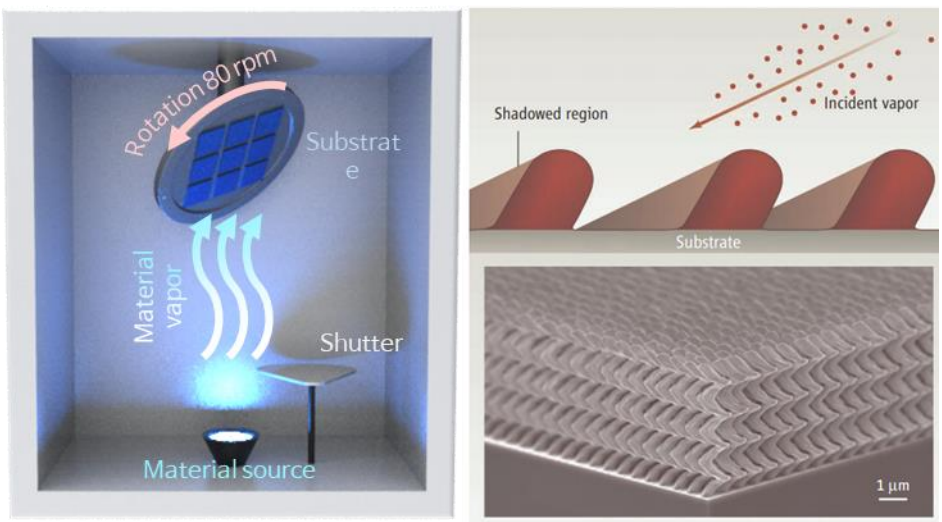

Figure 2.7. Schematic illustration of glancing angle deposition using e-beam evaporator and shadowing effects induced by initially deposited nuclei on the substrate.[18]

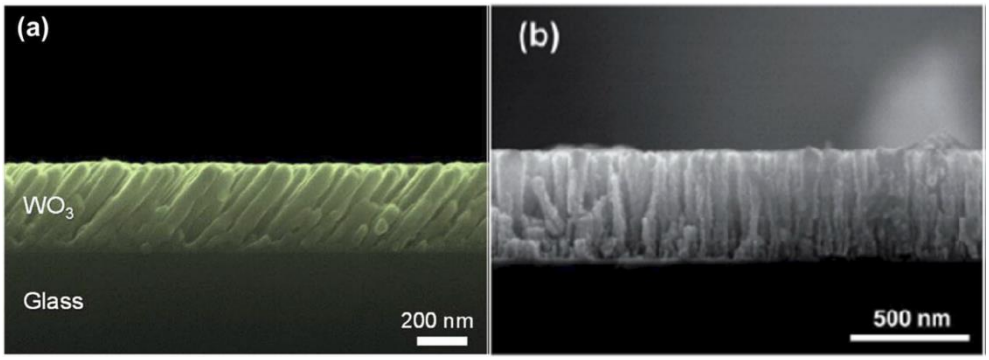

Figure 2.8. Cross-sectional SEM images of deposited metal oxide nanostructures using glancing angle deposition method using e-beam evaporation (a) without rotation and (b) with rotation.[21, 22]

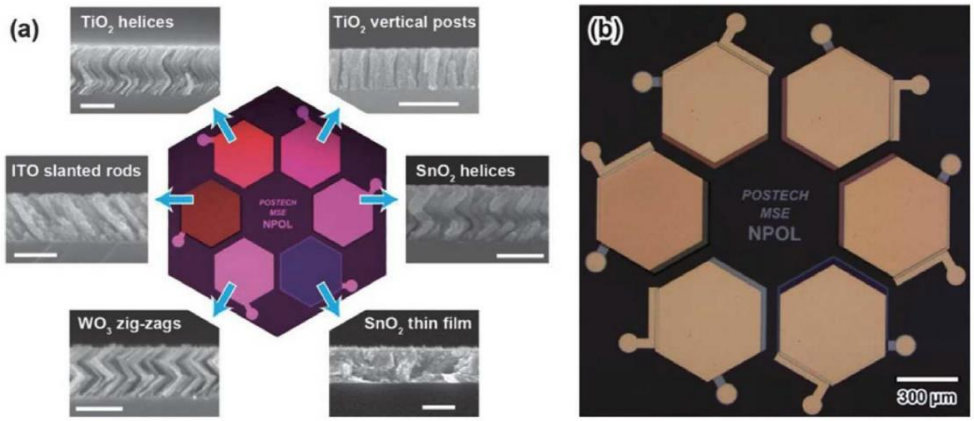

Figure 2.9. (a) Optical microscopy (OM) image of the fabricated prototype e-nose chip after the deposition of six different sensing layers, and corresponding cross-sectional SEM images. (Scale bars represent 300 nm) (b) OM image of the e-nose after the deposition of top and pad electrodes on the device shown in (a).[21]

2.3. References

[1] N. Barsan, U. Weimar, *J. Electroceram.* **2001**, 7, 143-167.

[2] M. E. Franke, T. J. Koplin, U. Simon, *Small* **2006**, 2(1), 36-50.

[3] H.-J. Kim, J.-H. Lee, *Sens. Actuat. B−Chem.* **2014**, 192, 607.

[4] D. Degler, U. Weimar, N. Barsan, *ACS Sens.* **2019**, 4, 2228-2249.

[5] N. Yamazoe, *Sens. Actuat. B−Chem.* **1991**, 5, 7-19.

[6] N. Barsan, D. Koziej, U. Weimar, *Sens. Actuat. B−Chem.* **2007**, 121, 18-35.

[7] S. Choopun, N. Hongsith, E. Wongrat, *Nanowires - Recent Advances*, IntechOpen, London, UK, 2012, DOI: 10.5772/54385.

[8] J. Li, Y. Lu, Q. Ye, M. Cinke, J. Han, M. Meyyappan, *Nano Lett.* **2003**, 3, 929-933.

[9] N. Yamazoe, G. Sakai, K. Shimanoe, *Catal. Surv. Asia* **2003**, 7, 63.

[10] H.-J. Kim, K.-I. Choi, K.-M. Kim, C. W. Na, J.-H. Lee, *Sens. Actuat. B−Chem.* **2012**, 171, 1029.

[11] J.-W. Yoon, H.-J. Kim, I.-D. Kim, J.-H. Lee, *Nanotechnology* **2013**, 24, 444005.

[12] C. W. Na, H.-S. Woo, J.-H. Lee, *RSC Adv.* **2012**, 2, 414.

[13] H.-R. Kim, K.-I. Choi, K.-M. Kim, I.-D. Kim, G. Cao, J.-H. Lee, *Chem. Commun.* **2010**, 46, 5061.

[14] Q. A. Drmosh, A. H. Hendi, M. K. Hossain, Z. H. Yamani, R. A. Moqbel, A. Hezam, M. A. Gondal, *Sens. Actuat. B−Chem.* **2019**, 290, 666-675.

[15] Y. Zhou, C. Zou, X. Lin, Y. Guo, *Appl. Phys. Lett.* **2018**, 113, 082103.

[16] J. M. Suh, Y.-S. Shim, K. C. Kwon, J.-M. Jeon, T. H. Lee, M. Shokouhimehr, H. W. Jang, *Electron. Mater. Lett.* **2019**, 15, 368-376.

[17] G. Velmathi, S. Mohan, R. Henry, IETE Tech. Rev. **2016**, 33(2), 122-129.

[18] M. J. Brett, M. M. Hawkeye, *Science* **2008**, 319(5867), 1192-1193.

[19] J. M. Suh, H. W. Jang, *J. Sens. Sci. Technol.* **2017**, 26, 228-234.

[20] H. G. Moon, Y.-S. Shim, D. H. Kim, M. Jeong, J. Y. Jung, S. M. Han, J. K. Kim, J.-S. Kim, H.-H. Park, J.-H. Lee, H. L. Tuller, S.-J. Yoon, H. W. Jang, *Sci. Rep.* **2012**, 2, 588.

[21] J.-M. Jeon, Y.-S. Shim, S. D. Han, D. H. Kim, Y. H. Kim, C.-Y. Kang, J.-S. Kim, M. Kim, H. W. Jang, *J. Mater. Chem. A* **2015**, 3, 17939.

[22] S. Hwang, H. Kwon, S. Chhajed, J. W. Byon, J. M. Baik, J. Im, S. H. Oh, H. W. Jang, S.-J. Yoon, and J. K. Kim, *Analyst* **2013**, 138(2), 443-450.

Chapter 3

1D Metal Oxide Nanostructures with Heterojunctions

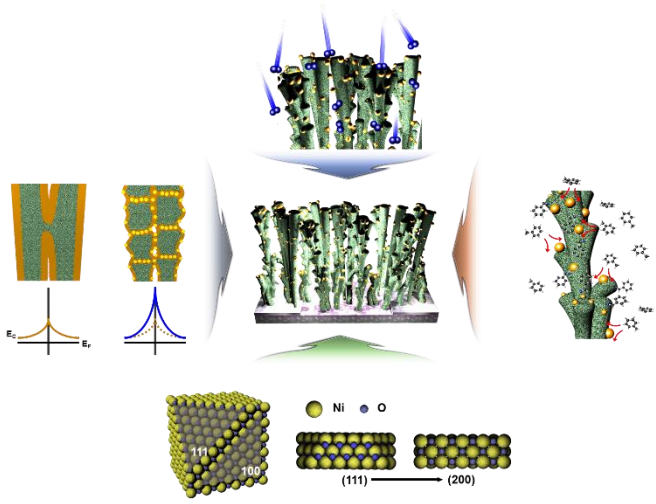

Adv. Mater. Technol. **2017**, 2(3), 1600259

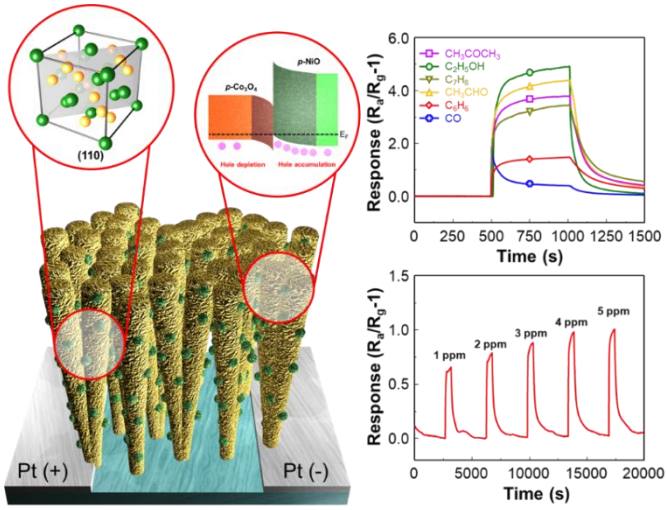

ACS Appl. Mater. Interface **2017**, 10(1), 1050-1058

3.1. *p*−*n* heterojunctions of nickel oxide and hematite

3.1.1. Introduction

In modern residences, human activities inside the buildings themselves, including exercising, manufacturing, working, and learning, have become increasingly important. Their consideration is therefore of paramount importance in the development of buildings and household products.[1] A recent survey on time budgeting among US residents found that individuals spent approximately 88% of their days inside buildings.[2] It is therefore easy to understand that the most important environment in relation to people's health is indoors. Volatile organic compounds (VOCs), which arise from building products including paints, varnishes, solvents, and preservatives, are the most relevant gases in this respect, and VOC emission from those substances is usually continuous and may last for several years in buildings, resulting in adverse health effects such as the sick building syndrome.[3] Toluene (C_7H_8), which arises mainly from paints and household solvents, can cause various conditions when people experience prolonged exposure; examples include tiredness, confusion, weakness, drunken-type actions, nausea, or loss of memory, appetite, hearing, or color vision. Thus, highly sensitive and selective detection of C_7H_8 is very important.[4]

Chemoresistive gas sensors based on metal oxides have been predominantly studied due to their superior advantages, including their simple operation, low cost, flexibility in production, and possible integration with other circuits. The *p*-type metal oxide semiconductors, including NiO, CuO, Cr_2O_3, Co_3O_4, or Mn_3O_4, have

attracted great attention because of their catalytic effect to promote selective oxidation of VOCs.[5] However, *p*-type semiconductors themselves exhibit a relatively weak response to analyte gases. According to Hübner *et al*.,[6] the response of *p*-type semiconductors is as low as the square root of that of *n*-type semiconductors when structural factors are equal, and such a low response may yield poor selectivity for various gases. Over the past decade, various approaches have been attempted to improve the gas sensing properties of *p*-type semiconductors, including (i) morphological control of the nanostructure,[7-9] (ii) metal doping or decoration,[10, 11] and (iii) formation of heterojunctions.[12, 13] Among the various efforts, heterostructures between two different materials have been reported to be very effective in enhancing the gas response.[14] Heterostructures with metal or metal oxide decorations can enhance gas sensing properties by promoting the adsorption of target gases (chemical sensitization) or by resistance modulation upon gas adsorption (electronic sensitization).[15] Recently, a wide variety of heterostructures based on *p*-type NiO with *n*-type α-Fe_2O_3 was studied, such as hollow spheres,[16] nanofibers[17] and tubular structures[18], for use in highly sensitive and selective VOC gas sensors, because α-Fe_2O_3 promotes selective oxidation of methyl groups (-CH_3) at elevated temperatures under oxidizing atmospheric conditions.[19] Despite reasonable results, achieving well-established and reproducible processes has remained as a problems to overcome.

Among the various heterostructures, especially 1-dimensional (1D) vertically ordered nanostructures with extremely large surface-to-volume ratios are very promising materials for high gas sensing performance due to their excellent target

gas accessibility and aggregation-free geometry.[20, 21] In our previous study,[22] we were successful in fully sensitizing SnO_2 nanorods through depositing SnO_2 and Au in multiple steps using a glancing angle deposition (GLAD) method. In that study, we only concentrated on full sensitization of the 1D nanostructures and did not consider additional effects of multiple-step heterostructuring in the 1D nanostructures on selective gas sensing. Compared to metal oxide nanorods composed of a single material, in which growth is only affected by the substrate, the growth of nanorods through multiple steps can be affected by the material deposited in the previous step. This unique effect of multiple-step heterostructuring can effectively be realized only when using the GLAD method. As a result, the orientation of the metal oxides can be altered by the stacking sequences, leading to different surface characteristics that directly influence the conductivity change of the metal oxides upon gas molecule adsorption. However, there has only been very little research on the modification of crystallographic orientation[23, 24] and approaches have been complex, expensive, and difficult in terms of making the nanostructures. Moreover, to the best of our knowledge, those studies' interpretations of gas sensing performances have been limited to aspects of electronic and chemical sensitization, and no systematic study has been conducted on *p*-type semiconducting materials with modification of the crystallographic orientation for high-performance gas sensors. In this study, we clearly identify that the crystallographic orientation of a metal oxide strongly depends on prior deposition steps in multiple-step heterostructuring.

Herein, we report extremely sensitive and selective C_7H_8 gas sensors using

vertically ordered nanostructures of α-Fe_2O_3-decorated NiO fabricated by a facile and effective method based on GLAD. NiO and Fe were deposited in multiple steps followed by oxidation into α-Fe_2O_3, resulting in multiple heterojunctions. The morphology of NiO nanorods and their crystallographic orientation were clarified by transmission electron microscopy (TEM) and X-ray diffraction (XRD), respectively. The gas sensing properties were measured and the selectivity of the decorated nanocorals investigated using principal component analysis (PCA) based on the collection of sensor responses to various gases. Our results here suggest that the decoration of *p*-type NiO 1D nanostructures with an *n*-type metal oxide like α-Fe_2O_3 through GLAD is an effective method to fabricate highly sensitive and selective gas sensors for C_7H_8 detection.

3.1.2. Experimental procedures

Sensor Fabrication. Interdigitated electrodes (IDEs) were fabricated by depositing Pt/Ti (150 nm/30 nm thick) on SiO_2/Si substrates (1 μm/500 μm thick) using photolithography. The distance between each electrode was 5 μm and there were 20 electrodes in 1 mm x 1 mm area. The Pt/Ti IDEs were sonicated in acetone and isopropanol followed by drying in nitrogen gas. Subsequently, only the area with electrodes was exposed by concealing the rest of the substrate with scotch tape. NiO grains and Fe pellets with 99.9% purity (Kojundo Chemistry) were used for film deposition. In order to fabricate the NiO nanorods, evaporation was conducted at glancing angle of 75, 80, 83, and 85° using a rotation speed of 80 rpm. The substrate was located 50 cm above the crucible, while the base pressure was 1×10^{-6} Torr and the growth rate 1.0 Å/s. After depositing 100 nm NiO nanorods, the substrate was positioned back to 0° and 1, 3, 5, and 7 nm Fe was deposited without rotation. Then, the substrate was positioned to the previously-used angle and NiO nanorods deposition was repeated. This process was repeated 6 times, with the whole process taking 5-6h. After deposition, all fabricated samples were annealed at 550 °C for 2h in ambient air. During annealing, NiO crystallized and Fe metal film agglomerated while simultaneously oxidizing into α-Fe_2O_3.

Characterization. The morphologies of the fabricated bare NiO nanorods and α-Fe_2O_3-decorated NiO nanocorals were characterized by a field-emission scanning electron microscope (FESEM, MERLIN-Compact) using an acceleration voltage of 1 kV and working distance of 3 mm. For cross-sectional transmission electron microscope (TEM) analysis, conventional mechanical polishing was followed by Ar

ion milling. Bright field and high-resolution images were obtained with a field-emission TEM (JEM-2100F) in order to investigate the morphology and structure of the bare NiO nanorods and the α-Fe_2O_3-decorated NiO nanocorals. In addition, orientations were measured by X-ray diffraction (XRD, D8 Advance), and chemical mapping of the α-Fe_2O_3-decorated NiO nanocorals was performed by energy dispersive X-ray spectroscopy (EDS).

Gas sensing measurement. Gas sensing measurements were performed in a quartz tube with an external heat source. Through an automated system, a repeating sequence of dry air and target gas (balanced with dry air, Sinjin Gases) injection occurred. A constant flow of 1000 sccm was used for both dry air and target gas. The concentration of all gases used in this study was fixed at 50 ppm, except for NO_2 which had a concentration of 5 ppm. The response to each target gas was precisely measured at a DC bias voltage of 1 V using a sourcemeter (Keithley 2400). The gas flow was controlled by a mass flow controller and all measurements were recorded by LabVIEW using a general purpose interface bus (GPIB) interface. Additional experimental details of the gas sensing measurements can be found in our previous work.[39-41]

3.1.3. Results and discussion

GLAD based on electron beam evaporation was selected as the synthesis method for vertically ordered NiO nanorods with α-Fe_2O_3 decoration (Figure 3.1a). By controlling the incident angle of vapor flux and orientation of the substrate, morphological properties such as the density, porosity, and diameter of the columnar nanostructures could be tailored, as shown in Figure 3.1b. To fabricate the vertically ordered NiO nanorods and apply them as a gas sensor, a substrate rotation speed of 80 rpm and tilt angle of 83° were used to deposit NiO on a SiO_2/Si substrate with Pt-interdigitated electrodes (IDEs) (Figure 3.1c). In order to fully decorate the NiO nanorods with a distribution of α-Fe_2O_3, we employed multiple deposition steps. Since the agglomeration of Fe metal followed by annealing into α-Fe_2O_3 nanoparticles is an effective way to decorate the whole surface of NiO nanorods with α-Fe_2O_3, we adopted Fe instead of α-Fe_2O_3, as the latter does not show agglomeration behavior during annealing. Firstly, an approximately 100-nm-thick layer of NiO nanorods was deposited (step 1), followed by a 3-nm-thick layer of Fe at a tilt angle of 0° on the NiO nanorods, uniformly coating them by minimizing the self-shadowing effect (step 2). We conducted step 1 and step 2 repeatedly until the total length reached around 600 nm (Figure 3.2). The fabricated samples were annealed at 550 °C for 2 h to oxidize Fe into α-Fe_2O_3. Scanning electron microscope (SEM) images show the cross-section of the bare NiO nanorods and the α-Fe_2O_3-decorated NiO nanorods on the substrate, respectively (Figure 3.1d and e). The bare NiO nanorods exhibited a typical nanorod morphology with a smooth surface and average diameter of 20 nm. Interestingly, the α-Fe_2O_3-decorated NiO nanorods exhibited a

very rough surface and their average diameter was much larger than that of the bare NiO nanorods. In the initial step of GLAD, evaporated unit cells adsorbed onto the substrate and two different forces influencing the unit cells existed: an adhesion force between the substrate and the adsorbed unit cells, and a binding force between the adsorbed unit cells.[25] The balance between these two forces determines the morphology of the fabricated nanostructures. The bare NiO nanorods grown on the SiO_2/Si substrate exhibited a relatively smooth surface. In sharp contrast, α-Fe_2O_3-decorated NiO nanorods grown on the SiO_2/Si substrate had a coral-like rough surface. Multiple deposition steps caused successive growth of NiO nanorods on Fe layers and thus the adhesion force between the substrate (Fe) and the adsorbed unit cells (NiO) changed, yielding a rough surface.[26]

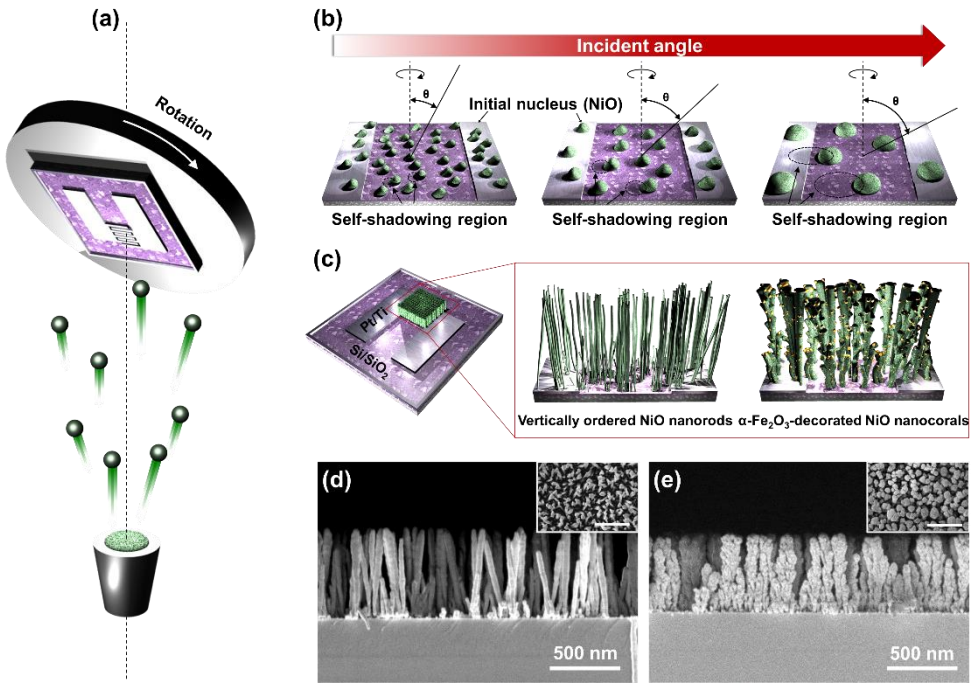

Figure 3.1. Schematics of (a) glancing angle deposition (GLAD) system based on electron-beam evaporation, (b) self-shadowing effects by increasing incident angle, and (c) vertically ordered NiO nanorods on Pt-interdigitated electrodes without and with α-Fe_2O_3 decoration. Cross-sectional SEM images of the NiO nanorods (d) without and (e) with α-Fe_2O_3 decoration. Insets are plane-view scanning electron microscope (SEM) images for each corresponding SEM figure. The scale bars indicate 500 nm.

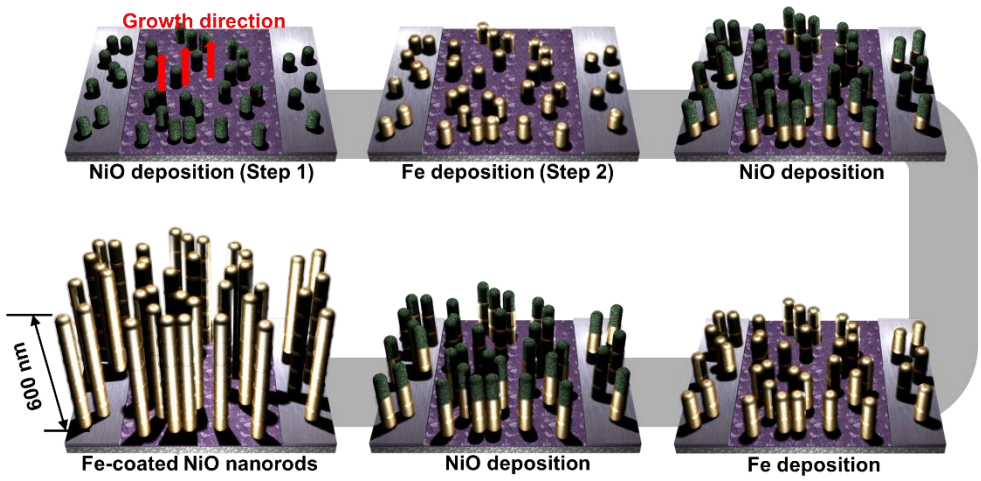

Figure 3.2. Schematic illustrations of detailed fabrication process for α-Fe_2O_3-decorated NiO nanocorals by multiple step glancing angle deposition method.

Cross-sectional TEM imaging of the α-Fe_2O_3-decorated NiO nanocorals showed that α-Fe_2O_3 nanoparticles entirely decorated not only the surface but also the joints of NiO nanocorals formed by multiple depositions (Figure 3.3a). Energy dispersive X-ray spectroscopy (EDS) mapping was conducted on the α-Fe_2O_3-decorated NiO nanocorals. Figure 3.3b-d show the chemical mapping of Fe, O, and Ni elements, respectively. The uniform distribution of Ni and O elements across the NiO nanocorals can easily be observed. In contrast to the Ni and O elements, Fe exhibited a sparse distribution, which indicates that the Fe film was changed to nanoparticles. High-resolution TEM images show the bare NiO nanorods and α-Fe_2O_3-decorated NiO nanocorals (Figure 3.3e-h). The selected area diffraction (SAED) patterns show that both the bare NiO nanorods and the α-Fe_2O_3-decorated NiO nanocorals were polycrystalline (Figure 3.4). However, bare NiO nanorods had a preferential orientation of (111). The NiO nanocorals with α-Fe_2O_3 decoration, on the other hand, initially preferred the (111) orientation, but were found to prefer the (200) orientation from the second step onward, which is consistent with the XRD results in Figure 3.3i (JCPDS #47-1049). Interestingly, we find that the morphological change occurred concurrently with the orientation change at the interface between the first and second NiO deposition steps. From these results, it follows that multiple NiO/Fe sequential depositions have a definite influence on the morphology of NiO nanocorals as well as their orientation, and this interesting phenomenon will be discussed later in detail.

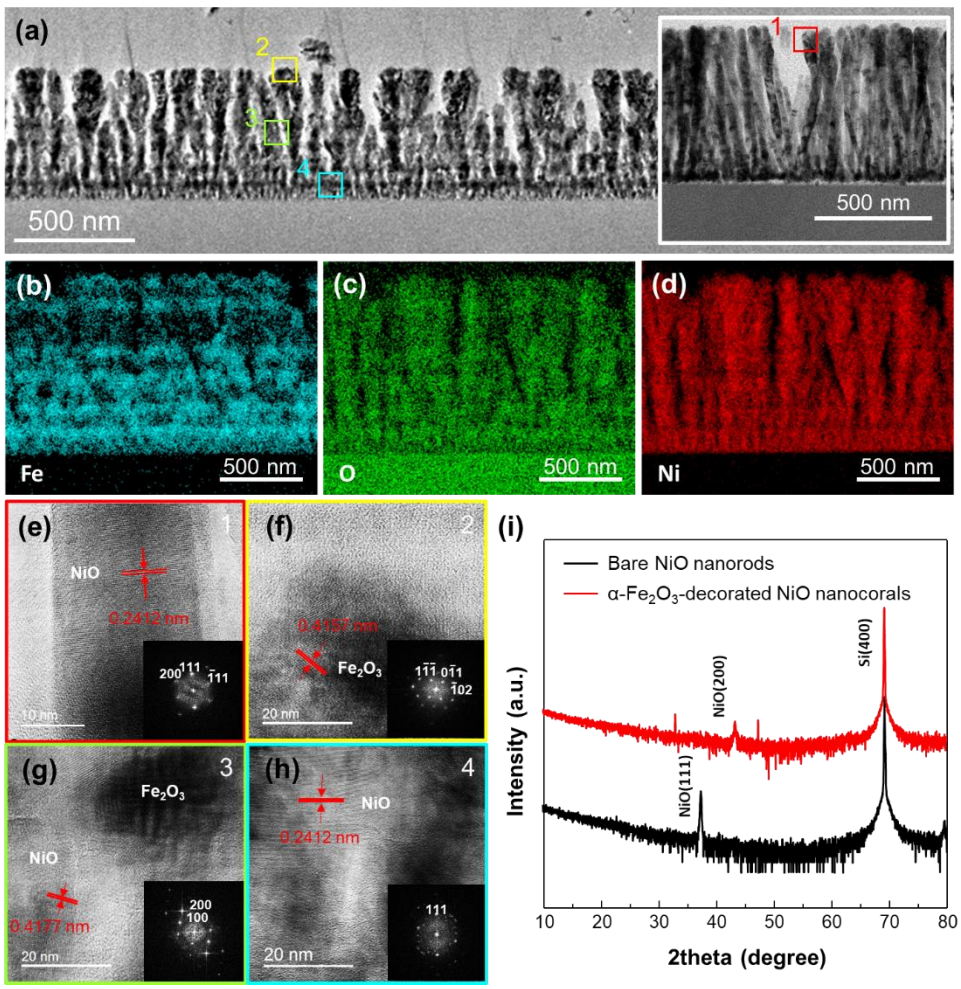

Figure 3.3. (a) Cross-sectional transmission electron microscope (TEM) image of α-Fe_2O_3-decorated NiO nanocorals. Inset shows TEM images of bare NiO nanorods. Energy-dispersive X-ray spectroscopy (EDS) mapping of (b) Fe, (c) O, and (d) Ni for α-Fe_2O_3-decorated NiO nanocorals. High-resolution TEM images for (e) bare NiO nanorods and (f–h) α-Fe_2O_3-decorated NiO nanocorals at different regions: (f) α-Fe_2O_3, (g) top NiO, and (h) bottom NiO, as indicated in (a) as numbers and dotted squares. (i) X-ray diffraction (XRD) data for bare NiO nanorods and α-Fe_2O_3-decorated NiO nanocorals.

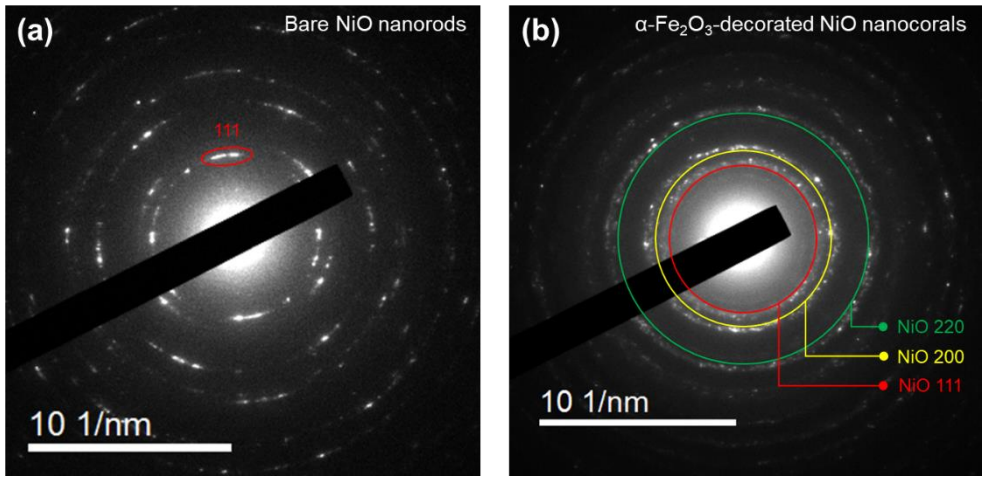

Figure 3.4. Selected area diffraction (SAED) patterns of (a) bare NiO nanorods and (b) α-Fe_2O_3-decorated NiO nanocorals.

Gas sensing properties of metal oxides are strongly dependent on three basic factors: the utility factor, receptor function, and transducer function.[15] In order to optimize those three factors and achieve maximum sensing performance, above all the optimal structure, temperature, and distribution of catalysts have to be investigated before measuring gas sensing properties. The porosity and density, i.e., the distances between vertically ordered metal oxide nanorods, strongly affect the gas sensing properties because they are related to both the target gas accessibility (utility factor) and the potential barrier height (transducer function). Hence, in order to find the optimal density of NiO nanorods, we prepared four different sample types with varying incident angles of vapor flux (75, 80, 83, and 85°), as shown in Figure 3.5. Upon exposure to 50 ppm C_2H_5OH at 300 °C, all samples exhibited different behaviors (Figure 3.6a). The maximum response (defined here as $(R_g - R_a)/R_a$, where R_g and R_a denote the sensors' resistance in the presence and absence of gas, respectively) was observed for the sample deposited on the substrate with a tilt angle of 83°. NiO nanorods deposited on the substrate with a tilt angle of 85° were too sparse to form necks between the nanorods, resulting in a high resistance with zero gas response. On the other hand, NiO nanorods deposited on the substrate with tilt angles of 75° and 80°, could not maximize the utility factor and transducer function to show the highest response, but still had better responses than the plain NiO film.

The operating temperature is also a critical factor to determine the performance of gas sensors based on metal oxides. In ambient air, oxygen molecules absorb onto the surface of semiconductors in three different forms (O_2^-, O^-, and O^{2-}) depending on the operating temperature.[27] The absorbed oxygen acts as a receptor for target gases

and forms a hole accumulation layer (HAL) on the semiconductor surface where the ionized oxygen components directly affect the resistance change upon exposure to target gases. For this reason, the gas sensing response of bare NiO nanorods deposited at 83° to 50 ppm C_2H_5OH was investigated at temperatures ranging from room temperature to 450 °C, as shown in Figure 3.6b. The base resistance of the NiO nanorods decreased as the operating temperature increased, reaching the highest response at 350 °C. At temperatures above 350 °C, increased desorption and oxidation of target gas molecules caused a decrease in gas response.

To effectively utilize the catalysts and maximize catalytic effects such as band bending (electronic sensitization) and gas dissociation (chemical sensitization), the distribution and size of metal or metal oxide nanoparticles have to be optimized, which can be achieved by controlling the initial thickness of the metal film. For example, when the initial thickness of the films is low, the inter-distances between metal or metal oxide nanoparticles are relatively long, which can then not entirely decorate the NiO surface. Conversely, when the initial thickness of the films is too high, the coverage of metal or metal oxide nanoparticles increases, leading to a reduced surface area for adsorption of gas molecules on the sensing material. Hence, we deposited Fe films with varying thicknesses (1, 3, 5, and 7 nm) to find the optimal distribution and size of α-Fe_2O_3 nanoparticles and measured their gas responses to 50 ppm C_2H_5OH at 350 °C, with results shown in Figure 3.6c. Both the base resistances and responses of all samples were increased due to the formation of a depletion layer from $p-n$ junctions, compared with the bare NiO nanorods. However, only 1-nm-thick samples showed a significantly higher resistance than that of the

bare NiO nanorods. As the thickness of Fe layer increased, the size of decorated α-Fe_2O_3 nanoparticles increased. For the 1-nm-thick samples, decorated α-Fe_2O_3 nanoparticles were too tiny to result in a significant change in the radial thickness of the nanorods (Figure 3.7). Therefore, only the *p*−*n* junction effect existed, resulting in relatively higher resistance. On the other hand, the samples with an Fe layer thicker than 3 nm had increased surface roughness with thicker radial diameters, leading to increased contact between the nanorods and a lower resistance. Finally, we determined the optimal conditions of α-Fe_2O_3-decorated NiO nanocorals for high sensing performance (Figure 3.6d-f) for the 3-nm-thick Fe film.

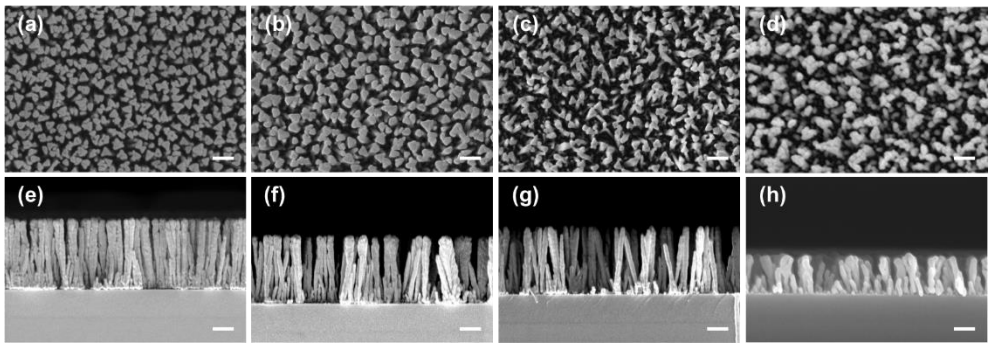

Figure 3.5. Plane-view SEM images of bare NiO nanorods deposited at (a) 75°, (b) 80°, (c) 83°, and (d) 85°. Cross-sectional SEM micrographs of bare NiO nanorods deposited at (e) 75°, (f) 80°, (g) 83°, and (h) 85°. Bar indicates 200 nm.

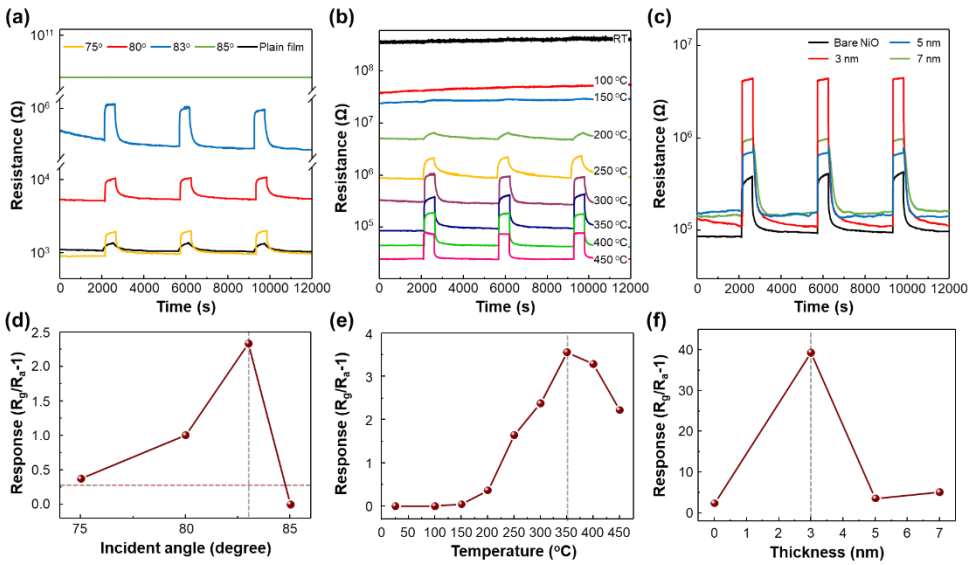

Figure 3.6. Response transients and responses of the bare NiO nanorods (a,d) deposited at different angles (75°, 80°, 83°, and 85°) at 300 °C to three consecutive exposures of 50 ppm C_2H_5OH and (b,e) measured at different temperatures from room temperature to 450 °C to 50 ppm C_2H_5OH. (c,f) Response transients and responses of α-Fe_2O_3-decorated NiO nanocorals with different thicknesses (1, 3, 5, and 7 nm) of Fe film at 350 °C to 50 ppm C_2H_5OH. Horizontal dotted line in (d) indicates the response of plain NiO film and vertical dotted lines in (d)–(f) indicate the maximum response value.

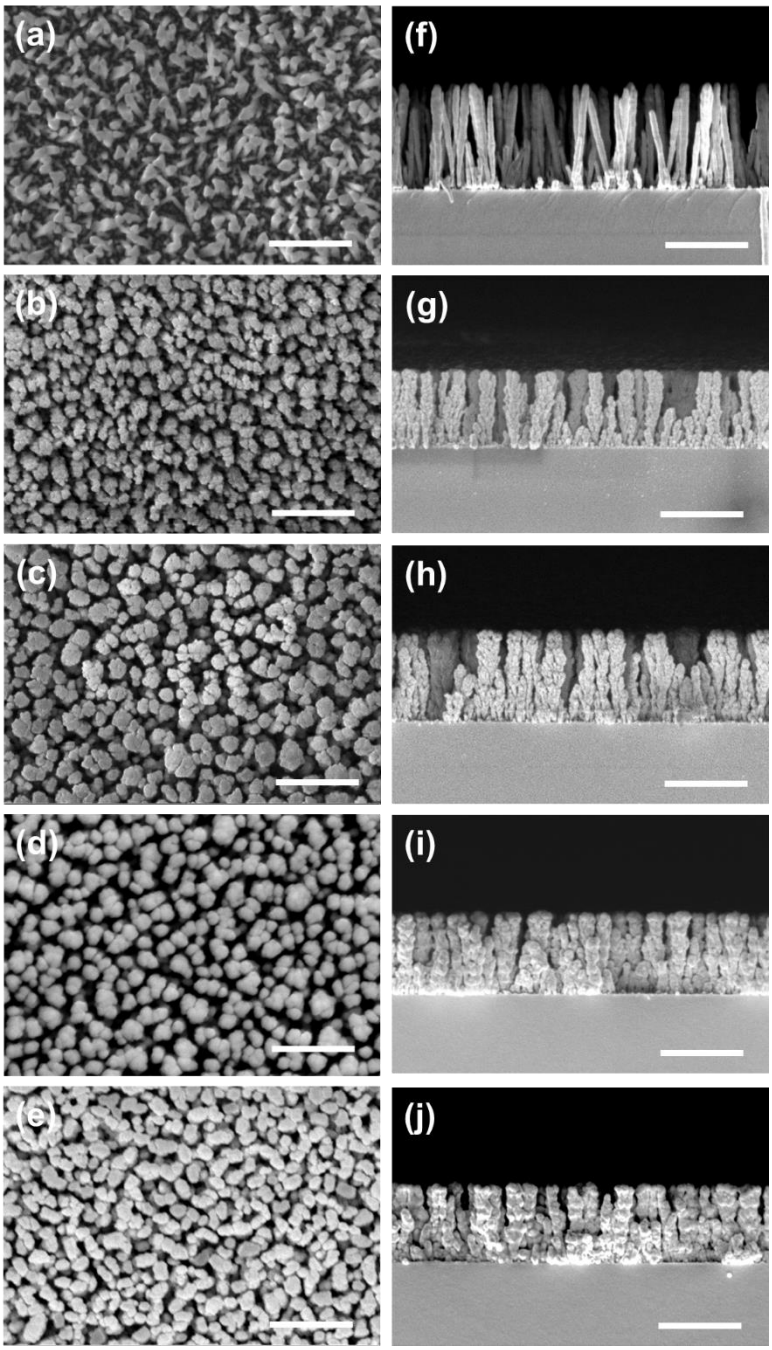

Figure 3.7. (a-e) Plane-view and (f-j) cross-sectional SEM images of (a, f) bare NiO nanorods and α-Fe_2O_3-decorated NiO nanocorals fabricated with (b, g) 1 nm, (c, h) 3 nm, (d, i) 5 nm, and (e, j) 7 nm-thick Fe layer. Bar indicates 500 nm.

The VOC selectivity of the α-Fe_2O_3-decorated NiO nanocorals at the optimum conditions was measured from their responses to various gases including C_2H_5OH, C_7H_8, CH_3CHO, CH_3COCH_3, C_6H_6, CO, NO_2, and H_2, measured at 350 °C. Figure 3.8a and b show the response transients of the bare NiO nanorods and α-Fe_2O_3-decorated NiO nanocorals. Compared with the bare NiO nanorods, the responses were enhanced, and response times decreased, to all gases for the α-Fe_2O_3-decorated NiO nanocorals (Figure 3.8c and d). To clearly differentiate the responses of both sample types to various target gases, responses were plotted as shown in Figure 3.9a and b. Interestingly, the bare NiO nanorods showed the highest response to C_2H_5OH and the second highest response to CH_3CHO, while the α-Fe_2O_3-decorated NiO nanocorals showed the highest response to C_2H_5OH and the second highest response to C_7H_8. The response to C_2H_5OH increased 10.8 times from 3.67 to 39.5, while that to C_7H_8 increased 45.4 times from 0.35 to 15.9. The response ratio S_a/S_b, where S_b and S_a are responses of the bare NiO nanorods and the α-Fe_2O_3-decorated NiO nanocorals, respectively, varied with the target gas, although C_7H_8 showed an extremely high response ratio, allowing selective detection of C_7H_8. Compared to previous studies of gas sensors based on NiO and α-Fe_2O_3, such a strong selective detection of a single target gas among various gases, as shown in Figure 3.9c, has not been shown before.[16-18, 28, 29] To investigate the selectivity in more detail, we examined the sensing results to three consecutive pulses of various gases (Figure 3.10) based on principal component analysis (PCA). Figure 3.11a and b show the principal component (PC1, PC2, and PC3) plots derived from normalized responses with an increase in the number of considered sensor elements on a 3D plane. The

data variance for each principal component is mentioned on its axis label. For bare NiO nanorods exposed to various gases, we did not find selectivity since the areas of most gases overlapped. However, for α-Fe_2O_3-decorated NiO nanocorals, except for CO and C_6H_6, most gases were easily separated, such as C_2H_5OH, C_7H_8, CH_3CHO, CH_3COCH_3, H_2, and NO. These results indicate that the fabricated α-Fe_2O_3-decorated NiO nanocorals exhibited excellent selectivity and could effectively distinguish various gases, especially C_7H_8.

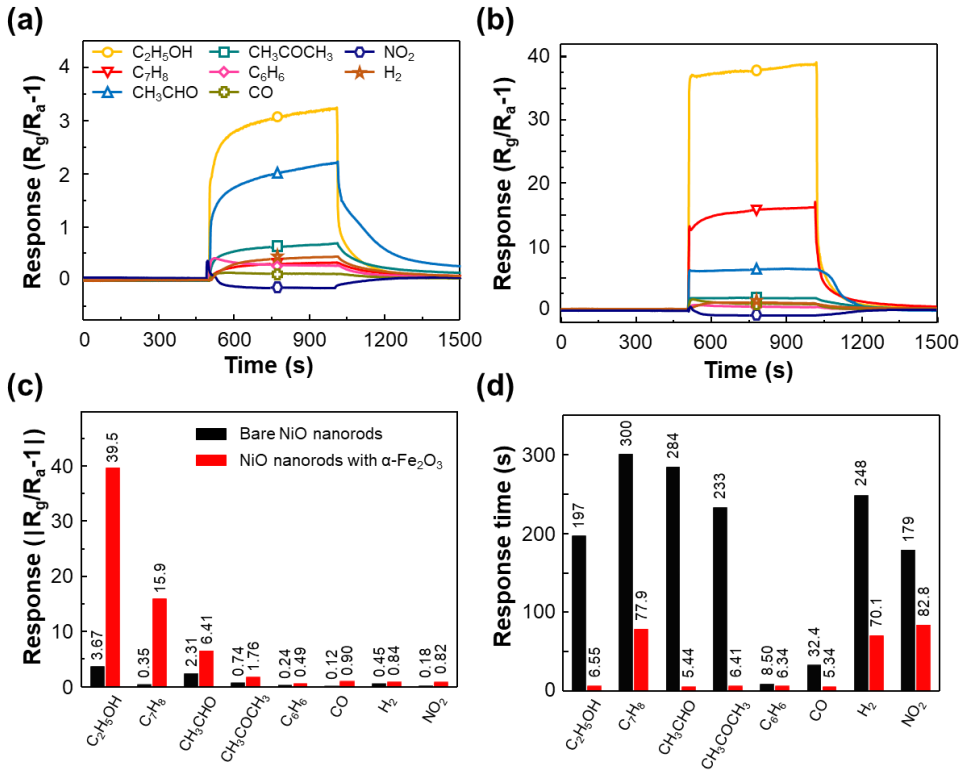

Figure 3.8. Response transients of (a) the bare NiO nanorods and (b) α-Fe_2O_3-decorated NiO nanocorals toward various gases at 350 °C. (c) Responses and (d) response times of bare NiO nanorods and α-Fe_2O_3-decorated NiO nanocorals to various gases (5 ppm for NO_2 and 50 ppm for other gases) at 350 °C.

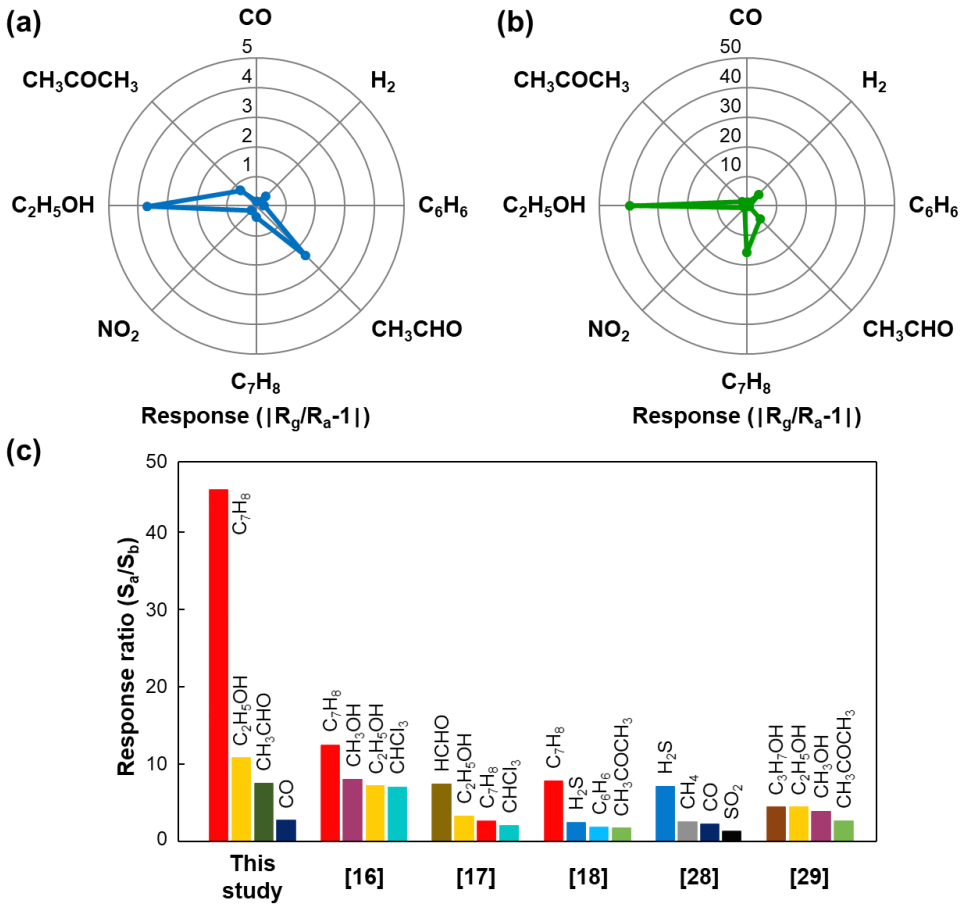

Figure 3.9. Polar plot for responses of (a) bare NiO nanorods and (b) α-Fe_2O_3-decorated NiO nanocorals to various gases (5 ppm for NO_2 and 50 ppm for other gases) at 350 °C. (c) Response ratio of various nanostructures based on NiO and α-Fe_2O_3 to several gases, as reported in the literature[16–18, 28, 29] and the present study.

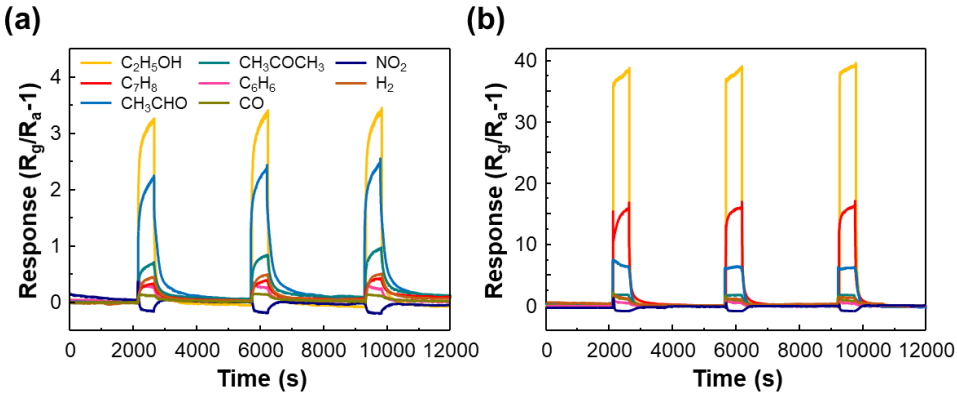

Figure 3.10. Response transients of (a) bare NiO nanorods and (b) α-Fe_2O_3-decorated NiO nanocorals to three consecutive exposures of various gases at 350 °C.

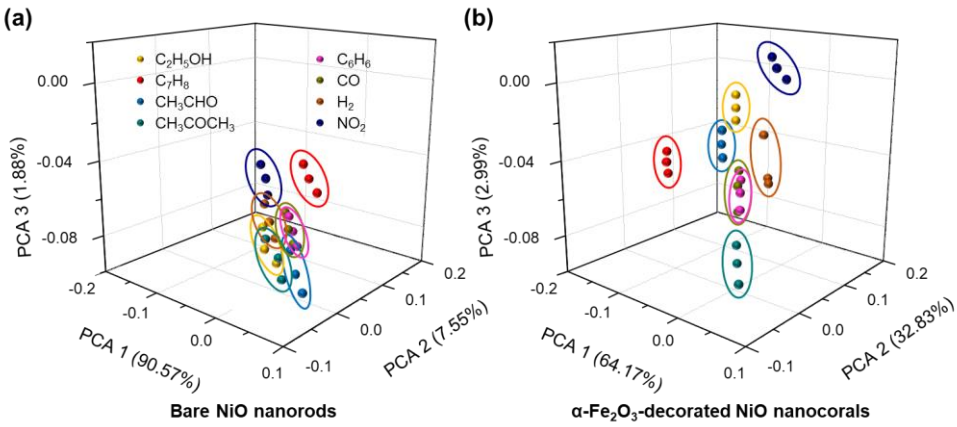

Figure 3.11. Principal component analysis (PCA) plot for (a) bare NiO nanorods and (b) α-Fe_2O_3-decorated NiO nanocorals in response to various gases (5 ppm for NO_2 and 50 ppm for other gases) at 350 °C.

For the evaluation of the practical applicability of α-Fe_2O_3-decorated NiO nanocorals, their stability during long-term operation (Figure 3.12) and humidity dependence (Figure 3.13) were investigated. The α-Fe_2O_3-decorated NiO nanocorals maintained their gas response upon eight consecutive gas pulses, showing their stability. Humidity induced an abrupt increase in the base resistance, but the α-Fe_2O_3-decorated NiO nanocorals still exhibited a good gas response to C_7H_8 in those conditions. To check the gas response linearity and calculate the detection limit, the response of α-Fe_2O_3-decorated NiO nanocorals to 1-5 ppm C_7H_8 was measured at 350 °C, as shown in Figure 3.14a. The sharp increase in gas response with the injection of C_7H_8 can be attributed to the sudden temperature drop by C_7H_8 and a small time gap between switching the air and C_7H_8 on and off, which resulted from our experimental settings. At high concentrations, this sharp increase is covered by the higher increase in current level, but at low concentrations it is not covered due to the smaller change in current level. The response of the α-Fe_2O_3-decorated NiO nanocorals increased with an increase in gas concentration from 1 to 5 ppm. The responses were 0.38, 0.48, 0.53, 0.55, and 0.59 to 1, 2, 3, 4, and 5 ppm C_7H_8, respectively. These responses are plotted as a function of the gas concentration in Figure 3.14b. The observed linear relationship between response and C_7H_8 concentration demonstrates the reliable operational capability over the tested concentration range. The slope of the concentration-response curve was calculated to be 0.101 ppm^{-1} by applying a linear least-squares fit. Although the C_7H_8 concentration of 1 ppm was the lowest measured experimentally in this study, the theoretical detection limit (signal-to-noise ratio > 3) was calculated to be as low as

~22 ppb.

The present study clearly shows that α-Fe_2O_3-decorated NiO nanocorals can exhibit enhanced gas sensing properties, with mechanisms shown in Figure 3.15. Multiple-step GLAD was already found in our previous study to be a very effective method to decorate the surface of nanorods.[22] Vertically ordered NiO nanorods are a very efficient structure for accessibility to target gas molecules (utility factor) and interaction between NiO and α-Fe_2O_3, which both have catalytic effects on the selective oxidation of methyl groups[13, 30], especially for C_7H_8[18, 31-34], contributing to the enhanced gas sensing properties (receptor function). However, we attribute the observed dramatic enhancement mainly to the increased potential barrier induced by the above-mentioned morphological changes (transducer function). Interestingly, α-Fe_2O_3 decoration changed the orientation of NiO nanocorals from (111) to (200). According to Ryu *et al.*,[35] NiO films with a (111) orientation have a smooth surface while those with a (200) orientation possess a relatively rough surface, which corresponds to the surface of the NiO nanocorals in this study. The rough surface of the decorated NiO nanocorals induces a difference in current path compared to the smooth surface of the bare NiO nanorods. It is known that narrower spaces between nanostructures can increase the resistance change upon exposure to target gases, mainly due to a diminished HAL.[36] Figure 3.16 shows the typical conduction mechanism of *p*-type semiconductor gas sensors. When oxygen atoms are absorbed (O_2^-, O^-, or O^{2-}) at ambient air, they extract electrons from the *p*-type semiconductor to form HAL at the surface. Then, molecules of reducing gases like VOCs donate electrons back to the HAL, leading to recombination. Therefore, the resistance of *p*-

type semiconductors increases when facing reducing gases. If the same amount of electrons or holes is available during the gas sensing reaction in *p*-type oxide semiconductors, the lower hole concentration in the HAL will show a larger variation in sensor resistance.[10] Compared to necks between the bare NiO nanorods with a smooth surface, the rougher surface of the α-Fe_2O_3-decorated NiO nanocorals resulted in narrower necks with a lower hole concentration. As a result, the unique morphological change in the NiO nanocorals induced by α-Fe_2O_3 decoration resulted in an enhanced the gas response to VOCs by decreasing the hole concentration in the HAL.

In terms of other contributing factors, the electronic interactions between NiO and α-Fe_2O_3 may also have enhanced the gas sensing performance. Since decoration of α-Fe_2O_3 nanoparticles was achieved by depositing Fe layers with successive annealing instead of by directly depositing α-Fe_2O_3, the surface decoration with α-Fe_2O_3 was successful due to the agglomeration of Fe. The effective surface decoration maximized $p-n$ junctions between NiO and α-Fe_2O_3. Well-distributed nanoscale $p-n$ junctions decreased the hole concentration in the HAL of NiO, leading to the increase in gas response.[37] The change in exposed atomic lattice due to the orientation change from (111) to (200) may have been another contributing factor. As shown in Figure 3.16, the (111) and (200) lattice structures of NiO have different ratios of exposed Ni and O atoms. A higher number of exposed Ni atoms can absorb more oxygen molecules, leading to a higher hole concentration in the HAL. Therefore, a (200) lattice of NiO, which was the orientation of the α-Fe_2O_3-decorated NiO nanocorals, is more beneficial in reducing the hole concentration in

the HAL. Wen *et al.*[38] also reported that the (200) lattice of NiO absorbs less oxygen components than the (111) lattice. This may be attributed to the more acidic nature of Fe^{3+} compared to Ni^{2+}, according to their electro-negativity. The more acidic Fe^{3+} tends to attract more O_2 molecule in air than Ni^{2+} and induce reduction of $O_2 + 2e^- \rightarrow O^{2-}$. In other words, compared with the Ni atoms in bare NiO nanorods, those in the α-Fe_2O_3-decorated NiO nanocorals interacted less with O_2 due to the adjacent Fe atoms during annealing. In addition, Ryu *et al.*[35] reported that differences in the partial pressure of O_2 when sputtering the NiO target can yield different orientations of the deposited NiO film. The NiO thin films showed a (111) orientation at 100% O_2 gas, since the (111) plane is the most densely packed plane for O^{2-}. Those formed at 0% O_2 gas showed both (111) and (200) orientations, since (100) is the most densely packed plane among the planes composed of both Ni^{2+} and O^{2-}. This study also supports the hypothesis that interactions between Fe^{3+} and O_2 may have caused the change in NiO orientation. Therefore, bare NiO nanorods will mainly be oriented in the (111) direction, while the α-Fe_2O_3-decorated NiO nanocorals are expected to be oriented in both (111) and (200) directions, which agrees with the XRD data.

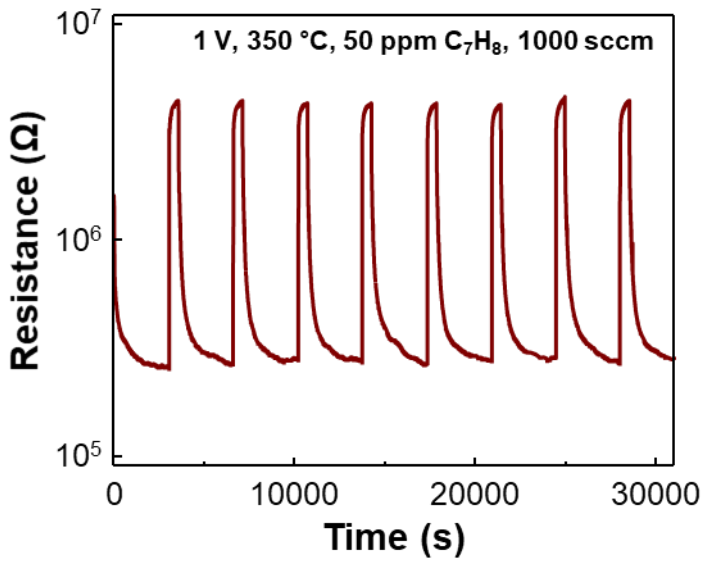

Figure 3.12. Responses curves of α-Fe_2O_3-decorated NiO nanocorals to 8 pulses of 50 ppm C_7H_8 at 350 °C.

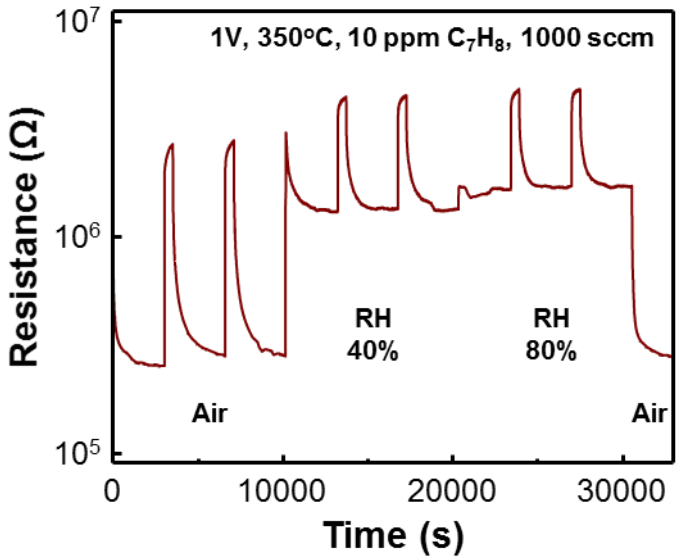

Figure 3.13. Gas sensing properties of α-Fe_2O_3-decorated NiO nanocorals to 10 ppm C_7H_8 at 350 °C under dry air and humidity (relative humidity (RH) 40 and 80%) conditions.

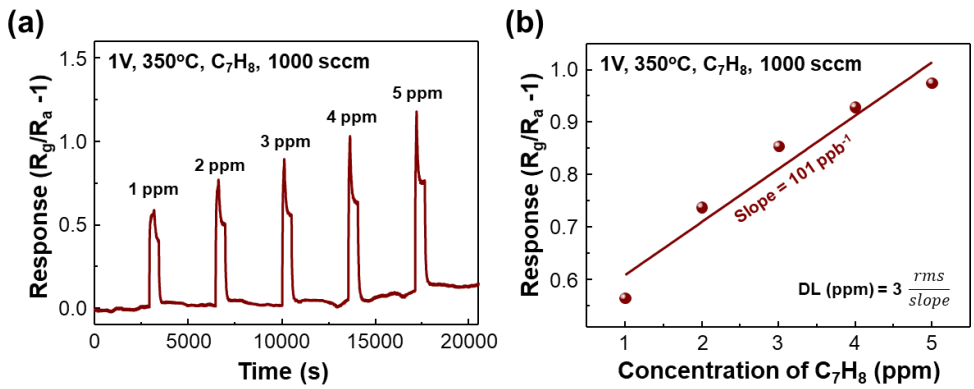

Figure 3.14. (a) Responses and (b) calibration of responses for α-Fe_2O_3-decorated NiO nanocorals toward 1–5 ppm C_7H_8 at 350 °C.

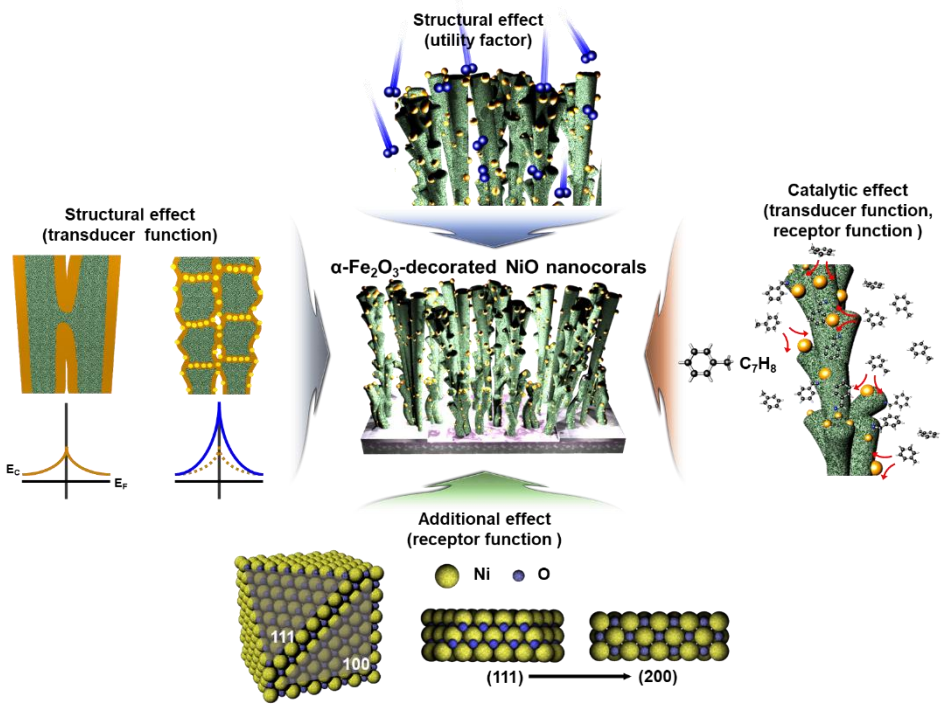

Figure 3.15. Schematic illustration of the utility factor, receptor function, and transducer function of the α-Fe_2O_3-decorated NiO nanocorals.

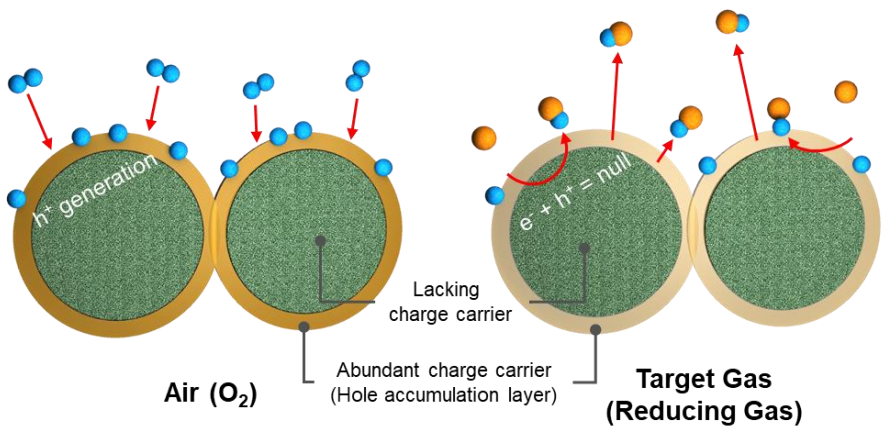

Figure 3.16. Typical conduction mechanism of *p*-type semiconductors.

3.1.4. Conclusion

We here demonstrated an effective way to decorate α-Fe_2O_3 on the whole surface of NiO nanorods through sequential deposition of NiO and Fe using a multiple-step glancing angle deposition method, followed by annealing to form α-Fe_2O_3. The distribution of Fe_2O_3 was optimized by controlling the thickness of the Fe films. Our results show that the responses of the α-Fe_2O_3-decorated NiO nanocorals to various gases such as C_2H_5OH, C_7H_8, CH_3CHO, CH_3COCH_3, C_6H_6, CO, NO_2, and H_2 dramatically increased compared to those of the bare NiO nanorods. This enhancement in response caused by α-Fe_2O_3 decoration could be explained by the efficiency of the vertically ordered nanostructures (utility factor), catalytic effects of NiO and α-Fe_2O_3 (receptor and transducer function), increased potential barrier between necks (transducer function), decreased hole concentration due to $p-n$ junctions and orientation change of the NiO. The observed excellent sensitivity toward C_7H_8 demonstrated the feasibility of applying the α-Fe_2O_3-decorated NiO nanocorals in gas sensors for indoor air quality monitoring. Finally, we strongly believe in broader applications of these fully-decorated nanostructures including in other chemical sensors, water splitting cells, photodetectors, and cathodes and anodes for batteries.

3.1.5. References

[1] G. Ingrosso, *Microchem. J.* **2002**, 73, 221.

[2] A. Anderson, A. Cheung, M. Lei, *Bachelor of Science Project Report*, Polytechnic Institute, Worchester, MA **2014**.

[3] J. J. Zhang, K. R. Smith, *Br. Med. Bull.* **2003**, 68, 209.

[4] S. J. Hwang, K. I. Choi, J. W. Yoon, Y. C. Kang, J. H. Lee, *Chem.–Euro. J.* **2015**, 21, 5872.

[5] H.-J. Kim, J.-H. Lee, *Sens. Actuat. B−Chem.* **2014**, 192, 607.

[6] M. Hübner, C. Simion, A. Tomescu-Sta˘noiu, S. Pokhrel, N. Bârsan, U. Weimar, *Sens. Actuat. B−Chem.* **2011**, 153, 347.

[7] N. G. Cho, I.-S. Hwang, H.-G. Kim, J.-H. Lee, I.-D. Kim, *Sens. Actuat. B−Chem.* **2011**, 155, 366.

[8] X. Song, L. Gao, S. Mathur, *J. Phys. Chem. C* **2011**, 115, 21730.

[9] G. Zhu, C. Xi, H. Xu, D. Zheng, Y. Liu, X. Xu, X. Shen, *RSC Adv.* **2012**, 2, 4236.

[10] H.-J. Kim, K.-I. Choi, K.-M. Kim, C. W. Na, J.-H. Lee, *Sens. Actuat. B−Chem.* **2012**, 171, 1029.

[11] J.-W. Yoon, H.-J. Kim, I.-D. Kim, J.-H. Lee, *Nanotechnology* **2013**, 24, 444005.

[12] C. W. Na, H.-S. Woo, J.-H. Lee, *RSC Adv.* **2012**, 2, 414.

[13] H.-R. Kim, K.-I. Choi, K.-M. Kim, I.-D. Kim, G. Cao, J.-H. Lee, *Chem. Commun.* **2010**, 46, 5061.

[14] R. Rajendran, Z. Yaakob, M. A. M. Teridi, M. S. A. Rahaman, K. Sopian,

Mater. Lett. **2014**, 133, 123.

[15] N. Yamazoe, G. Sakai, K. Shimanoe, *Catal. Surv. Asia* **2003**, 7, 63.

[16] C. Wang, X. Cheng, X. Zhou, P. Sun, X. Hu, K. Shimanoe, G. Lu, N. Yamazoe, *ACS Appl. Mater. Interfaces* **2014**, 6, 12031.

[17] J. Cao, Z. Wang, R. Wang, S. Liu, T. Fei, L. Wang, T. Zhang, *J. Mater. Chem. A* **2015**, 3, 5635.

[18] C. Wang, T. Wang, B. Wang, X. Zhou, X. Cheng, P. Sun, J. Zheng, G. Lu, *Sci. Rep.* **2016**, 6, 26432.

[19] D. H. Kim, Y.-S. Shim, J.-M. Jeon, H. Y. Jeong, S. S. Park, Y.-W. Kim, J.-S. Kim, J.-H. Lee, H. W. Jang, *ACS Appl. Mater. Interfaces* **2014**, 6, 14779.

[20] D. H. Kim, Y.-S. Shim, H. G. Moon, H. J. Chang, D. Su, S. Y. Kim, J.-S. Kim, B. K. Ju, S.-J. Yoon, H. W. Jang, *J. Phys. Chem. C* **2013**, 117, 17824.

[21] H. G. Moon, Y. R. Choi, Y.-S. Shim, K.-I. Choi, J.-H. Lee, J.-S. Kim, S.-J. Yoon, H.-H. Park, C.-Y. Kang, H. W. Jang, *ACS Appl. Mater. Interfaces* **2013**, 5, 10591.

[22] J.-M. Jeon, Y.-S. Shim, S. D. Han, D. H. Kim, Y. H. Kim, C.-Y. Kang, J.-S. Kim, M. Kim, H. W. Jang, *J. Mater. Chem. A* **2015**, 3, 17939.

[23] D. Cappus, C. Xu, D. Ehrlich, B. Dillmann, C. Ventrice, K. Al Shamery, H. Kuhlenbeck, H.-J. Freund, *Chem. Phys.* **1993**, 177, 533.

[24] H. Kuhlenbeck, S. Shaikhutdinov, H.-J. Freund, *Chem. Rev.* **2013**, 113, 3986.

[25] W. Huan-Hua, S. Yi-Jian, W. Chu, Y. Blum, *Chin. Phys. Lett.* **2008**, 25, 234.

[26] K. Marre, H. Neddermeyer, *Surf. Sci.* **1993**, 287, 995.

[27] K. Wetchakun, T. Samerjai, N. Tamaekong, C. Liewhiran, C. Siriwong, V.

Kruefu, A. Wisitsoraat, A. Tuantranont, S. Phanichphant, *Sens. Actuat. B−Chem.* **2011**, 160, 580.

[28] F. Li, Y. Chen, J. Ma, *RSC Adv.* **2014**, 4, 14201.

[29] X. Shen, Q. Liu, Z. Ji, G. Zhu, H. Zhou, K. Chen, *CrystEngComm* **2015**, 17, 5522.

[30] M. Bettahar, G. Costentin, L. Savary, J. Lavalley, *Appl. Catal. A* **1996**, 145, 1.

[31] G. Bai, H. Dai, J. Deng, Y. Liu, K. Ji, *Catal. Commun.* **2012**, 27, 148.

[32] G. Bai, H. Dai, J. Deng, Y. Liu, W. Qiu, Z. Zhao, X. Li, H. Yang, *Chem. Eng. J.* **2013**, 219, 200.

[33] W. Han, J. Deng, S. Xie, H. Yang, H. Dai, C. T. Au, *Ind. Eng. Chem. Res.* **2014**, 53, 3486.

[34] J. Ouyang, J. Pei, Q. Kuang, Z. Xie, L. Zheng, *ACS Appl. Mater. Interfaces* **2014**, 6, 12505.

[35] H. Ryu, G. Choi, W. Lee, J. Park, *J. Mater. Sci.* **2004**, 39, 4375.

[36] N. Barsan, C. Simion, T. Heine, S. Pokhrel, U. Weimar, *J. Electroceram.* **2010**, 25, 11.

[37] H.-J. Kim, H.-M. Jeong, T.-H. Kim, J.-H. Chung, Y. C. Kang, J.-H. Lee, *ACS Appl. Mater. Interfaces* **2014**, 6, 18197.

[38] R. T. Wen, C. G. Granqvist, G. A. Niklasson, *Adv. Funct. Mater.* **2015**, 25, 3359.

[39] Y.-S. Shim, L. Zhang, D. H. Kim, Y. H. Kim, Y. R. Choi, S. H. Nahm, C.-Y. Kang, W. Lee, H. W. Jang, *Sens. Actuat. B−Chem.* **2014**, 198, 294.

[40] Y.-S. Shim, H. G. Moon, D. H. Kim, L. Zhang, S.-J. Yoon, Y. S. Yoon, C.-Y.

Kang, H. W. Jang, *RSC Adv.* **2013**, 3, 10452.

[41] Y.-S. Shim, D. H. Kim, H. Y. Jeong, Y. H. Kim, S. H. Nahm, C.-Y. Kang, J.-S. Kim, W. Lee, H. W. Jang, *Sens. Actuat. B−Chem.* **2015**, 213, 314.

3.2. *p*–*p* heterojunctions of cobalt oxide and nickel oxide

3.2.1. Introduction

Human activities nowadays, such as office works, lectures, exercises, performing arts, or manufacturing, are mainly conducted indoors. Many kinds of harmful gases are emitted from various objects present inside buildings and they damage the human body. For example, formaldehyde from building materials causes sick building syndrome and ozone from sterilizers and printers destroys lung cells with its strong oxidizing property.[1-2] Especially, organic compounds with a high vapor pressure—thus, existing in vapor phase at room temperature, called volatile organic compounds (VOCs)—are the most significant harmful substances influencing indoor air quality. Although VOCs, such as ethanol (C_2H_5OH), acetone (CH_3COCH_3), acetealdehyde (CH_3CHO), toluene (C_7H_8), carbon monoxide (CO), and benzene (C_6H_6), are usually emitted in a low concentration, their emission is continuous, and prolonged exposure to them leads to severe damage to the human body, such as tiredness, nausea, or loss of memory, appetite, hearing, or color vision, or even cancer in the case of C_6H_6.[3] Thus, highly sensitive and selective detection of VOCs is essential.

In order to detect various VOCs with high sensitivity and selectivity, various studies on metal–oxide semiconductors have been conducted using chemoresistive-type gas sensors. The chemoresistive-type gas sensors have strong advantages in terms of their simple operation, low cost, and flexibility for application to the existing circuits.[4] Among various metal–oxide semiconductors, owing to the catalytic effect to promote the selective oxidation of VOCs, *p*-type metal–oxide

semiconductors, such as copper oxide (CuO), chrome oxide (Cr_2O_3), cobalt oxide (Co_3O_4), nickel oxide (NiO), or manganese oxide (Mn_3O_4), are strong candidates for the detection of VOCs.[5-9] Especially, Co_3O_4 is well-known for its catalytic effect in the oxidization of CO, alkanes, and C_7H_8 to effectively detect VOCs and its large oxygen adsorption is promising for gas sensing applications.[10-11] NiO is another widely used *p*-type metal–oxide semiconductor owing to its catalytic effects toward aromatic-substances-related reactions.[12-14] However, *p*-type metal oxides including Co_3O_4 and NiO have comparatively lower gas response than *n*-type metal–oxide semiconductors.[15] As low gas response can yield poor selectivity of various VOCs, there have been intensive studies on enhancing the response of gas sensors based on Co_3O_4 and NiO including increasing the active surface area by designing nanostructures (utility factor), improving the electronic properties via metal doping, catalyst decoration, or forming heterojunctions (receptor and transducer function).[16-19] Especially, heterojunctions between different materials are very effective in enhancing the gas response by promoting the adsorption of target gases (chemical sensitization) or resistance modulation upon gas adsorption (electronic sensitization).[20] Over the past few decades, various gas sensors using *p–n* heterojunctions have been reported but very few studies have been reported on gas sensors based on *p–p* isotype heterojunctions.[21-22] Compared to *p–n* heterojunctions, where recombination between majority charge carriers occurs and the total number of charge carriers is decreased, isotype heterojunctions can inject majority charge carriers from wide band gap materials to narrow band gap materials, resulting in spatially separated charge carriers without a decrease in the total number of charge

carriers.[23-24] Therefore, more electronic interactions between semiconductors and gas molecules, and enhanced catalytic effects toward VOCs by the combination of isotype *p*-type semiconductors as *p–p* heterojunctions can be expected.

Herein, we report highly sensitive and selective VOC gas sensors based on *p–p* isotype heterojunctions using vertically aligned Co_3O_4 nanostructures decorated with NiO fabricated using the multiple-step glancing angle deposition (GLAD) method. Based on our previous studies, the multiple-step GLAD method has been found to be an effective strategy to decorate catalysts or nanoparticles on the existing nanostructures.[25-26] The oxidization and agglomeration of Ni into NiO during annealing result in numerous *p–p* heterojunctions with increased active site density and increased conductivity of Co_3O_4 leading to better performance.[27] The investigation on the morphologies and crystallographic orientations of Co_3O_4 nanorods (NRs) was conducted using scanning electron microscopy (SEM), transmission electron microscopy (TEM), and X-ray diffraction (XRD). The gas sensing properties were measured and the selectivity of NiO-decorated Co_3O_4 NRs was investigated using principal component analysis (PCA) based on gas responses and response times. Our results herein suggest that the *p–p* isotype heterojunctions can be effective structures for fabricating highly sensitive and selective VOCs gas sensors.

3.2.2. Experimental procedures

Gas sensor fabrication. Interdigitated electrodes (IDEs) were fabricated by depositing Pt/Ti (100-nm-/30-nm-thick) on SiO_2/Si substrates (300-μm-/400-μm-thick) using an e-beam evaporator after patterning via photolithography. Twenty electrodes were placed in an area of 1 mm × 1 mm with the inter-distance of 5 μm between them. The IDE-patterned substrates were cleaned by sonication in acetone and isopropanol followed by drying in N_2 gas. In order to deposit sensing materials only on the active area of IDEs, the rest of the substrate was concealed with scotch tape. Co_3O_4 grains and Ni pellets with 99% purity (Kojundo Chemistry) were used for the deposition. Electron-beam evaporation was performed at the glancing angles of 73°, 75°, 78°, 80°, and 83° with a rotation speed of 80 rpm. The base pressure of the chamber was maintained at 1×10^{-6} Torr and the growth rate was 1.0 Å/s. After depositing 100 nm of Co_3O_4 NRs, the substrate was returned to 0° for the uniform deposition of Ni film (thicknesses 1, 3, and 5 nm) without rotation. Subsequently, the substrate was returned to the initial glancing angle for the deposition of further 100 nm Co_3O_4 NRs. These procedures were repeated six times to obtain the thickness of 600 nm. After deposition, all the fabricated samples were annealed at 550 °C for 2 h in air condition.

Characterization. The morphologies of the fabricated bare Co_3O_4 NRs and NiO-decorated Co_3O_4 NRs were characterized using a field-emission SEM (SU-70, Hitachi), with an acceleration voltage of 5 kV and working distance of 8 mm, and field-emission TEM (JEM-2100F, JEOL). Focused ion beam milling (Helios 650, FEI) was conducted for the preparation of TEM specimens. Through TEM, bright-

field and high-resolution images were obtained, and energy-dispersive X-ray spectroscopy (EDS) analysis was conducted. XRD (D8 Advance, Bruker Miller) was used for the crystallographic investigation of the bare Co_3O_4 NRs and the NiO-decorated Co_3O_4 NRs.

Gas sensing measurement. Gas sensing measurements were conducted in a quartz tube placed in a furnace for external heating. Dry air and target gas (balanced with dry air, Sinjin Gases) were injected in a repeated sequence using an automated system. A constant flow of 1000 sccm was maintained for every gas injection. The concentration of all the gases used in this study was fixed at 50 ppm. The electric current was precisely measured under constant DC bias of 1 V using a SourceMeter (Keithley 2400). The additional experimental details of the gas sensing measurements are available in our previous works.[28-31]

3.2.3. Results and discussion

The vertically aligned Co_3O_4 NRs with NiO decoration were fabricated using the multiple step GLAD method with an e-beam evaporator (Figure 3.17). First, the morphological features of the bare Co_3O_4 NRs were optimized. By changing the glancing angle of the substrate, the incident angle of vapor flux could be controlled and therefore, the initial nucleation could be controlled to design the porosity, density and diameter of Co_3O_4 NRs. At a low incident angle, the initial nuclei were relatively small and dense owing to a small self-shadowing region whereas they were relatively large and sparse at a high incident angle, leading to lower porosity and smaller diameter of NRs (Figure 3.18a). Figures 3.18b–f show the cross-sectional SEM images of the bare Co_3O_4 NRs deposited at the tilting angles of 73°, 75°, 78°, 80°, and 83°. An increase in the diameter of Co_3O_4 NRs as the incident angle increased can be clearly observed with the increase in porosity in the insets of Figure 3.18b–f. At the incident angle of 73°, Co_3O_4 NRs were too densely deposited to combine with each other and become thick NRs. At the incident angle of 83°, Co_3O_4 NRs were too sparsely deposited and had a very large diameter owing to heavy nucleation. Figure 3.18g shows the morphology of the plain Co_3O_4 thin film. In order to fabricate NiO-decorated Co_3O_4 NRs, Co_3O_4 and Ni were deposited in sequence via the multiple-step GLAD and subsequently annealed to induce the agglomeration of Ni metal into NiO nanoparticles via oxidization. Instead of directly depositing NiO which does not agglomerate during annealing, the utilization of Ni is very effective for decorating NiO nanoparticles on the entire surface of Co_3O_4. The photograph and optical microscopy images of the fabricated device show uniformly deposited NiO-

decorated Co_3O_4 NRs over the active area (Figure 3.19). As shown in the cross-sectional TEM images (Figure 3.20a) and EDS mapping (Figure 3.20b–d), Ni substances were effectively decorated on the entire surface of Co_3O_4 NRs. This indicates that NiO nanoparticles were decorated on the both inside and outside of Co_3O_4 NRs with the formation of *p–p* heterojunctions. Notably, the crystallographic orientation of Co_3O_4 changed from (111) to (220) with NiO decoration as shown in the high-resolution (HR)-TEM images (Figure 3.20e and f), and this can be confirmed using XRD results (Figure 3.20g). The NiO-decorated Co_3O_4 NRs exhibited polycrystalline nature with the preferred orientation of (220) and (311). The selected-area electron diffraction (SAED) patterns (Figure 3.21) clearly exhibited the polycrystalline nature of the NiO-decorated Co_3O_4 NRs. In our previous study, changes in the crystallographic orientation were observed to influence the gas sensing properties and this will be discussed in detail later.[25]

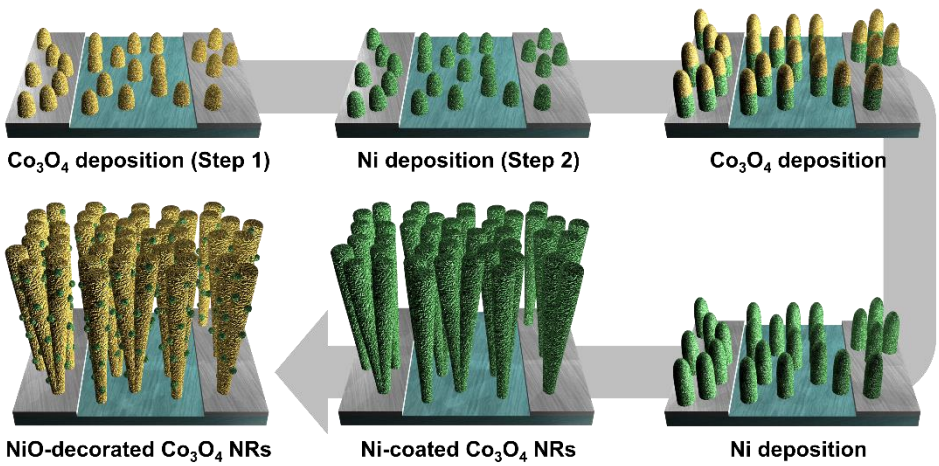

Figure 3.17. Fabrication procedure of NiO-decorated Co_3O_4 NRs.

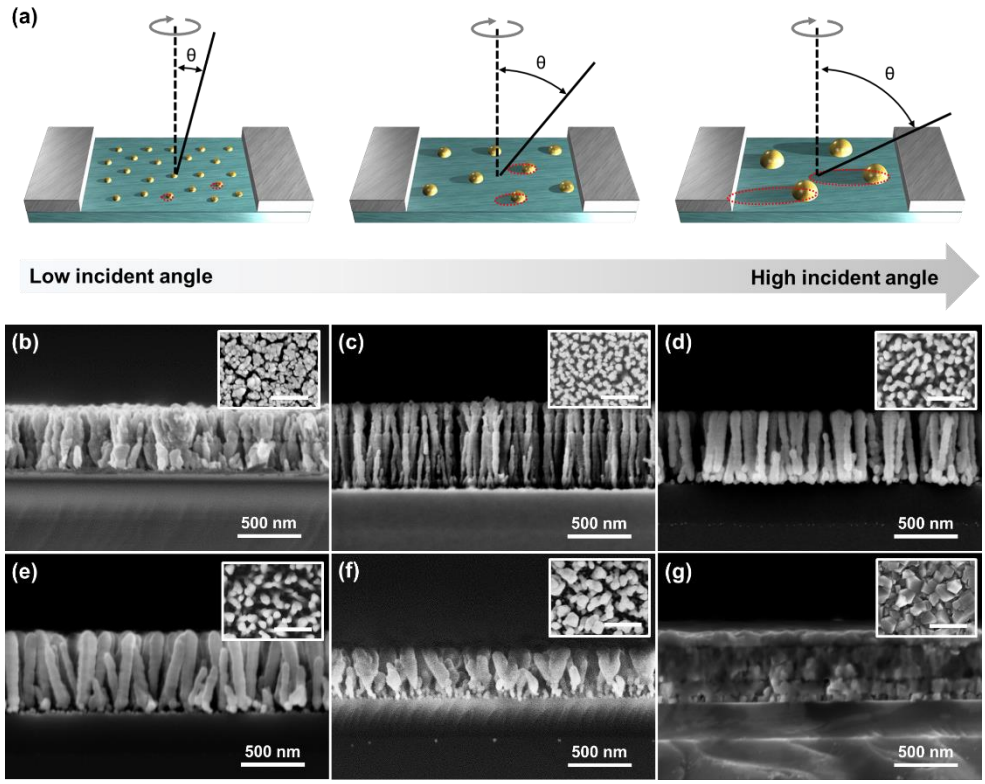

Figure 3.18. (a) Schematic illustrations of initial nucleus formation at different incident angles. Cross-sectional SEM images of the bare Co_3O_4 NRs deposited at (b) 73°, (c) 75°, (d) 78°, (e) 80°, and (f) 83° and (g) the plain Co_3O_4 thin film. The insets show plane-view SEM images of each sample.

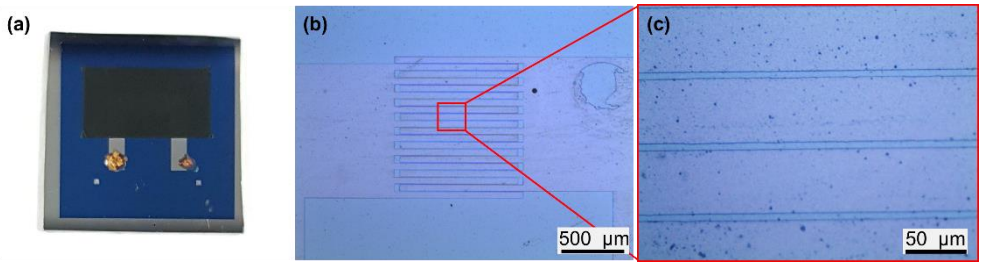

Figure 3.19. (a) Photograph of fabricated NiO-decorated Co_3O_4 NRs on Pt-interdigitated electrodes (IDEs) and (b, c) optical microscopy images in magnification of (b) x50 and (c) x500.

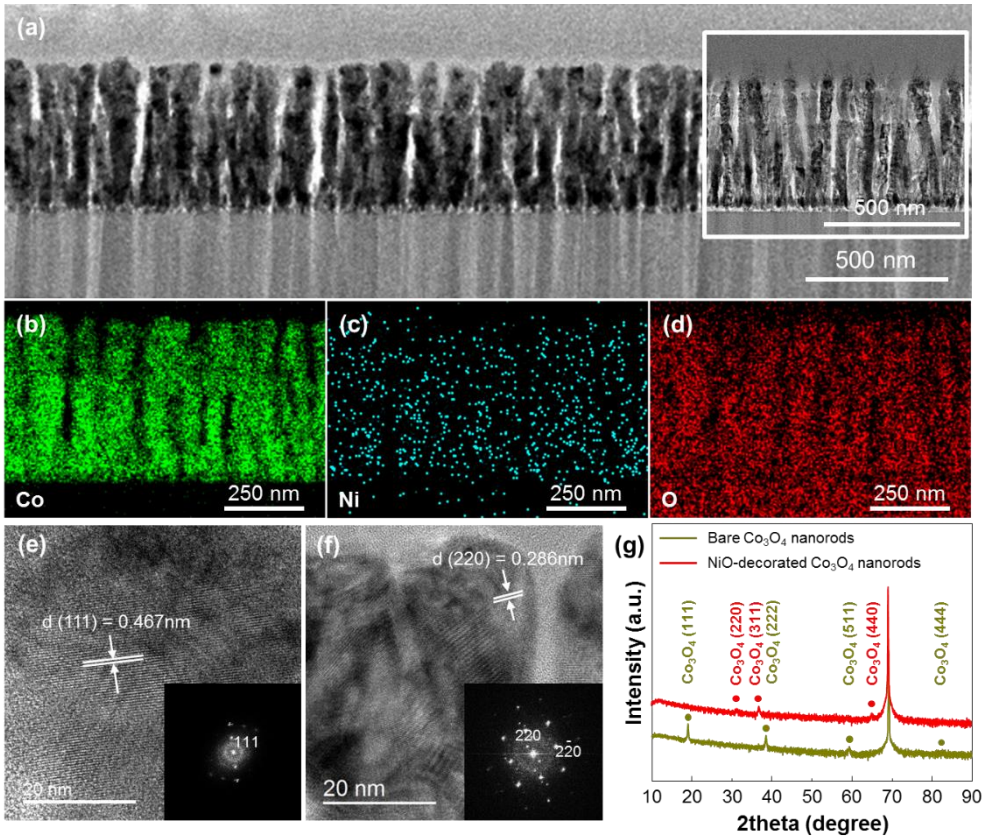

Figure 3.20. (a) Cross-sectional TEM image of NiO-decorated Co_3O_4 NRs. The inset shows a TEM image of bare Co_3O_4 NRs. EDS mapping of (b) Co, (c) Ni, and (d) O for NiO-decorated Co_3O_4 NRs. High-resolution TEM images of (e) bare Co_3O_4 NRs and (f) NiO-decorated Co_3O_4 NRs. (g) XRD data for bare Co_3O_4 NRs and NiO-decorated Co_3O_4 NRs.

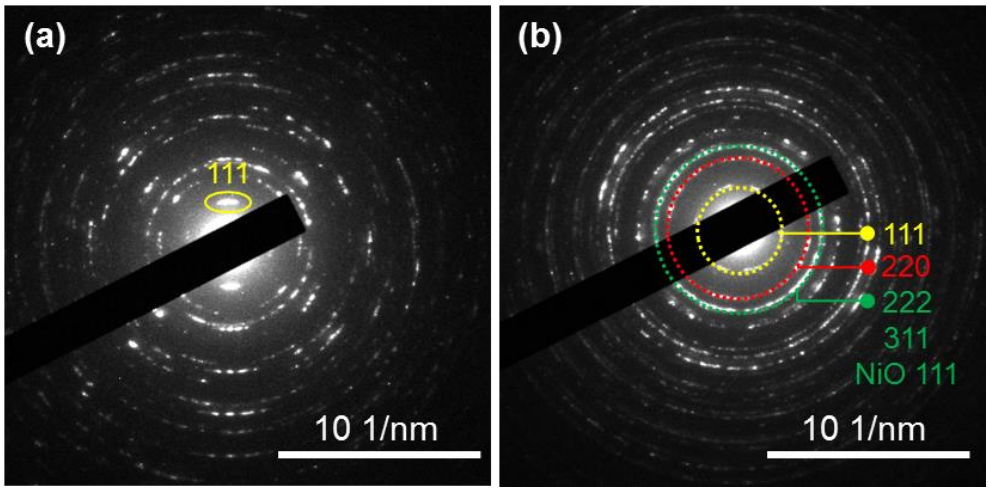

Figure 3.21. Selected area diffraction (SAED) patterns of (a) bare Co_3O_4 NRs and (b) NiO-decorated Co_3O_4 NRs.

Gas sensing properties are closely related to and affected by morphologies (utility factor), operating temperature, and distribution of catalysts (receptor function). The bare Co_3O_4 NRs deposited at different deposition angles (73°, 75°, 78°, 80°, and 83°) were exposed to three consecutive pulses of 50 ppm of C_2H_5OH at 300 °C to determine the optimal deposition angle (Figure 3.22a and d). The bare Co_3O_4 NRs deposited at 75° exhibited the highest gas response (defined here as $(R_g – R_a)/R_a$, where R_g and R_a correspond to the resistance of the sensor in the presence and absence of target gas, respectively), whereas all the fabricated Co_3O_4 NRs exhibited higher gas response than the plain Co_3O_4 thin film (0.00412) except those deposited at 83° as the inter-distance between NRs was too far to form an electric conduction path at this angle. As both the increase in the diameter and decrease in the porosity of the Co_3O_4 NRs with the increase in deposition angle contribute to effective surface area for the adsorption of gas molecules, the balance was obtained at 75° to achieve the highest gas response. The increase in base resistance can be attributed to the increase in the inter-distance between NRs with the increase in deposition angles. With the bare Co_3O_4 NRs deposited at 75°, the gas responses to 50 ppm of C_2H_5OH were measured at different operating temperatures (150, 200, 250, 300, 350, and 400 °C) (Figure 3.22b and e). The optimal operating temperature was determined to be 350 °C and all the measurements thereafter were conducted at 350 °C. As the operating temperature increased, the base resistance decreased owing to the enhanced electrical conduction at higher temperature. Subsequently, the NiO-decorated Co_3O_4 NRs were fabricated with precisely controlled thicknesses (1, 3, and 5 nm) of Ni interlayers (Figure 3.23) and exposed to 50 ppm of C_2H_5OH at

350 °C to determine the optimal conditions (Figure 3.22c and f). The NRs deposited with 1-nm-thick Ni interlayers exhibited the highest gas response. Notably, compared to the bare Co_3O_4 NRs, the base resistance of the NiO-decorated Co_3O_4 NRs decreased initially (1 nm) and increased for NRs with thicker Ni interlayers (3 and 5 nm). This will be discussed in detail later.

The sensitivity and selectivity of the NiO-decorated Co_3O_4 NRs toward various VOCs were investigated with 50 ppm of CH_3COCH_3, C_2H_5OH, C_7H_8, CH_3CHO, C_6H_6, and CO at 350 °C. Figures 3.24a and b show the response transients of the bare Co_3O_4 NRs and the NiO-decorated Co_3O_4 NRs toward various VOCs, respectively. The bare Co_3O_4 NRs exhibited the highest gas response to C_2H_5OH, the second highest response to CH_3COCH_3, and the third highest response to CH_3CHO. The NiO-decorated Co_3O_4 NRs exhibited the highest gas response to C_2H_5OH, the second highest response to CH_3CHO, and third highest response to CH_3COCH_3. For a better comparison, the responses of the bare Co_3O_4 NRs and NiO-decorated Co_3O_4 NRs were plotted in a polar plot as shown in Figure 3.24c, and the overall responses to VOCs were observed to be enhanced for the NiO-decorated Co_3O_4 NRs The response ratio S_a/S_b, where S_a and S_b represent the responses of the bare Co_3O_4 NRs and the NiO-decorated Co_3O_4 NRs, respectively, was calculated and plotted as shown in Figure 3.24d in order to investigate the selectivity toward various VOCs. Owing to the NiO decoration, the gas response toward C_6H_6 significantly increased (S_a/S_b = 16.78) compared to the responses toward other gases (S_a/S_b for CH_3COCH_3, C_2H_5OH, C_7H_8, CH_3CHO, and CO = 3.23, 3.59, 7.90, 5.30, and 5.49, respectively). Compared to other previously reported studies which measured the gas sensing

properties of Co_3O_4-based composite materials toward C_6H_6, the NiO-decorated Co_3O_4 NRs exhibited higher gas response and selectivity than other combinations (Table 3.1).[32-38] For further investigation of selectivity, PCA was conducted for the bare Co_3O_4 NRs and NiO-decorated Co_3O_4 NRs (Figure 3.24e and d). In order to perform PCA, the gas responses and response times were collected from exposure to three pulses of each VOC gas tested in this work (Figure 3.25). It can be clearly observed that C_6H_6 and CO were completely separated for the NiO-decorated Co_3O_4 NRs compared to that for the bare Co_3O_4 NRs. Although the overall distribution of the components was reduced, the collection of data (gas responses, response ratio, and PCA) from the NiO-decorated Co_3O_4 NRs and their processing can provide enhanced selective detection of various VOCs.

For the investigation of the potential practical applications of NiO-decorated Co_3O_4 NRs, their stability and detection limits were studied. As shown in Figure 3.26a, the NiO-decorated Co_3O_4 NRs exhibited stable gas responses to eight consecutive pulses of 50 ppm of C_6H_6 to demonstrate their stability. For the detection limit, the NiO-decorated Co_3O_4 NRs were exposed to 1–5 ppm of C_6H_6 at 350 °C and their response curves are shown in Figure 3.26b. The gas responses exhibit evident linearity with the increase in gas concentration, demonstrating their reliable operation over the examined concentration range (Figure 3.26c). The slope of the concentration-to-response curve was calculated to be 0.088 ppm^{-1} using a linear least-squares fit. Although the lowest concentration of C_6H_6 tested in this work was 1 ppm, the theoretical detection limit (signal-to-noise ratio >3) was calculated to be as low as approximately 13.91 ppb.

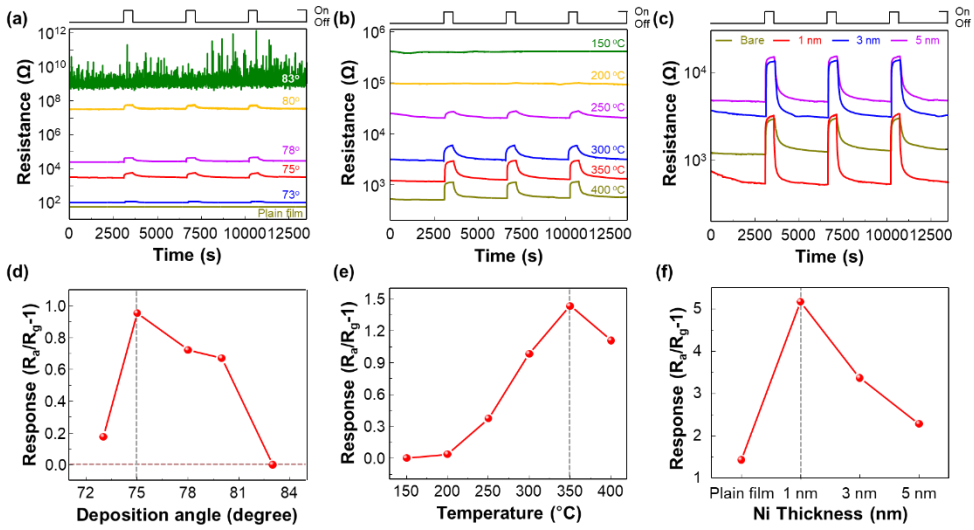

Figure 3.22. Response transients and responses of the bare Co_3O_4 NRs (a, d) deposited at different angles (73, 75, 78, 80, and 83°) at 300 °C to three consecutive exposures of 50 ppm of C_2H_5OH and (b, e) measured at different temperatures from 100 to 400 °C to 50 ppm of C_2H_5OH. (c, f) Response transients and responses of NiO-decorated Co_3O_4 NRs with different thicknesses (1, 3, and 5 nm) of the Ni film at 350 °C to 50 ppm of C_2H_5OH. The horizontal dotted line in (d) indicates the response of the plain Co_3O_4 film (0.00412), and the vertical dotted lines in (d)−(f) indicate the variables with the maximum response value.

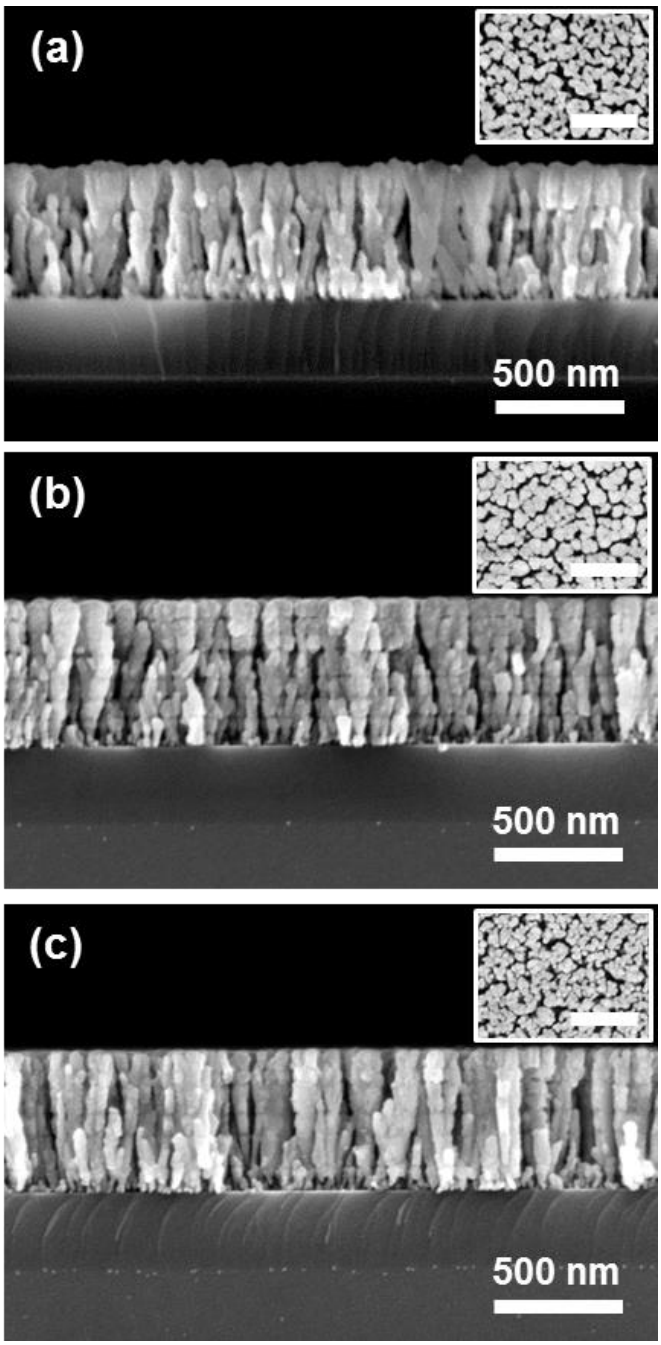

Figure 3.23. Cross-sectional SEM images of the NiO-decorated Co_3O_4 NRs with (a) 1 nm, (b) 3 nm, and (c) 5 nm-thick Ni layer. Insets show plane-view SEM images of each sample. Scale bars in insets indicate 500 nm.

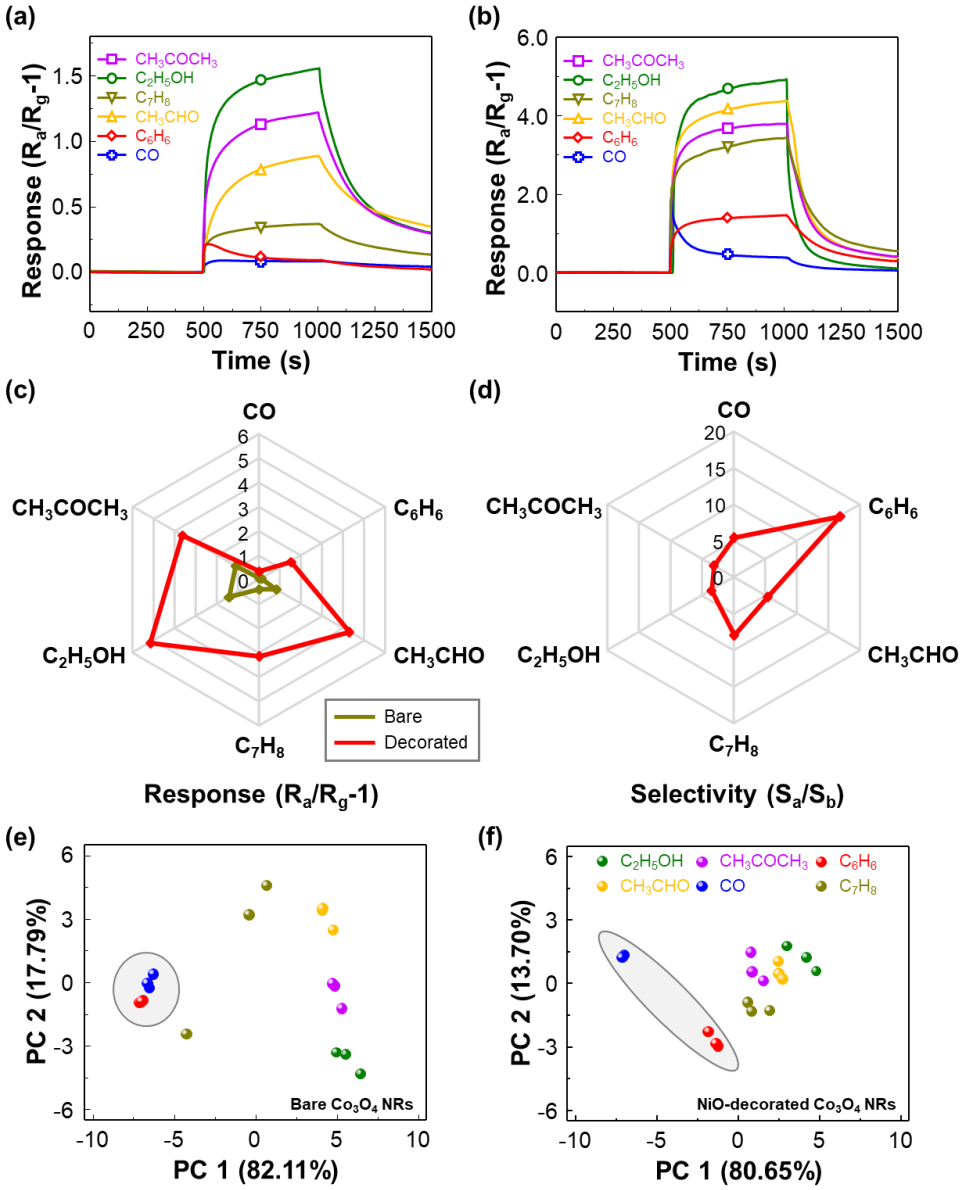

Figure 3.24. (a, b) Response transients and (e, f) PCA plots of (a, e) bare Co_3O_4 NRs and (b, f) NiO-decorated Co_3O_4 NRs to various gases (50 ppm) at 350 °C. Polar plots for (c) responses and (d) selectivity to various gases (50 ppm) at 350 °C.

Table 3.1. Gas Sensing Properties of Co_3O_4-Based Materials toward C_6H_6, as Reported in the Literature and the Present Study

Materials	Concen. (ppm)	Operating Temp. (℃)	Gas response		Selectivity	Ref.
			Composite	Bare		
$Co_3O_4/NiCo_2O_4$	100	238.9	0.16	0.10	1.62	[32]
Co_3O_4/Fe_2O_3	100	200	0.68	N/A	N/A	[33]
Co_3O_4/WO_3	100	280	0.50	N/A	N/A	[34]
Co_3O_4/SnO_2	5	275	0.93	1.73	0.54	[35]
Co_3O_4/MoS_2	5	RT	0.16	N/A	N/A	[36]
Co_3O_4/Cu_2O	100	350	0.90	N/A	N/A	[37]
Co_3O_4/ZnO	100	350	0.08	0.43	0.19	[38]
Co_3O_4/NiO	50	350	**1.49**	0.09	**16.8**	**Our work**
	5	350	**1.00**	N/A	N/A	

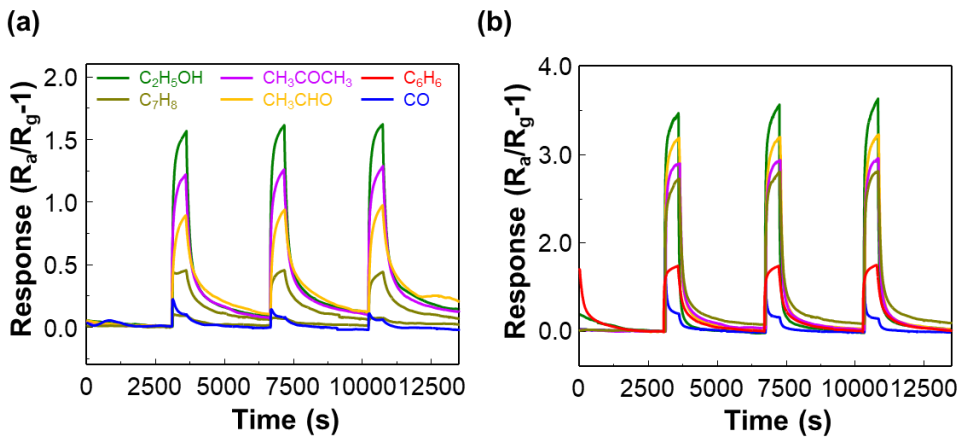

Figure 3.25. Response transients of (a) the bare Co_3O_4 NRs and (b) NiO-decorated Co_3O_4 NRs to three consecutive exposures of various gases (50 ppm) at 350 °C.

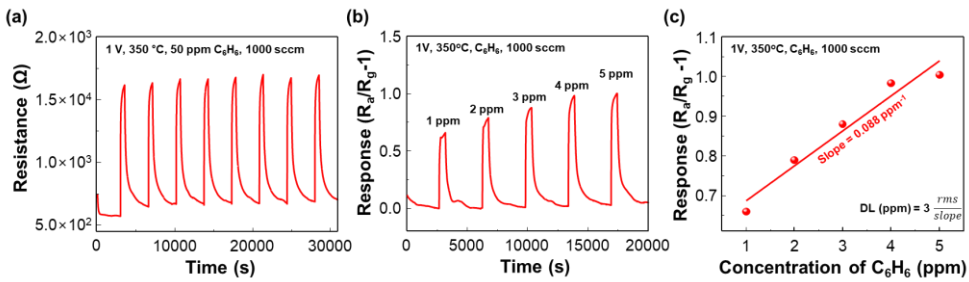

Figure 3.26. (a) Response curves of NiO-decorated Co_3O_4 NRs to 8 pulses of 50 ppm of C_6H_6 at 350 °C. (b) Responses and (c) calibration of responses for NiO-decorated Co_3O_4 NRs toward 1−5 ppm of C_6H_6 at 350 °C.

The NiO-decorated Co_3O_4 NRs can enhance the gas sensing properties of the bare Co_3O_4 NRs owing to following mechanisms. In air ambient, oxygen atoms interact with metal oxides and become adsorbed onto the surface in the form of O^{2-}, O^-, or O_2^- depending on the operating temperature.[39] In this reaction, *p*-type metal–oxide semiconductors provide electrons to oxygen atoms, and holes are generated. Therefore, a hole accumulation layer is formed on the surface of *p*-type metal–oxide semiconductors. After stabilization in air ambient, the target gas (reducing gas) molecules approach and provide electrons to *p*-type metal–oxide semiconductors to recombine with holes on the surface. Therefore, the electrical resistance increases upon the adsorption of target gas molecules, and these changes in the electrical signal are utilized for gas sensing. Therefore, the amount of oxygen atom adsorption and the resulting hole depletion layer can contribute to different gas sensing performances. From XRD data and SAED patterns, the NiO-decorated Co_3O_4 NRs exhibited a polycrystalline nature with the preferred orientation of (220) and (311) whereas the bare Co_3O_4 NRs exhibited the (111) orientation. As illustrated in Figure 3.27a–c, Co_3O_4 had a face-centered cubic structure with Co^{2+} and Co^{3+} coexisting in the unit cell.[40] Depending on the crystallographic orientation, the exposed atomic configurations differed from each other and those in the (111), (110), and (311) directions are illustrated. While the (111) direction exposed only Co^{2+} atoms, the (110) and (311) directions exposed both Co^{2+} and Co^{3+} atoms. The number of Co^{2+} exposed was also greater in the (110) planes than in the (111) planes. Therefore, more electric charge carriers can be generated by the exposed lattice of NiO-decorated Co_3O_4 NRs and they lower the base resistance as previously mentioned in Figure

3.22c. Moreover, as Co^{3+} atoms with higher charges are exposed, more oxygen components from air ambient can be adsorbed and more active sites are provided to gas molecules for access, leading to higher gas response. As the thickness of Ni interlayers increases to more than 1 nm, the base resistance starts to increase to a value more than that of the bare Co_3O_4 NRs, and this can be attributed to the formation of more *p–p* isotype heterojunctions. The energy band diagram shown in Figures 3.27d and e demonstrates the band bending before and after contact. As Co_3O_4 and NiO are both *p*-type semiconductors, their major charge carriers are holes. As Co_3O_4 has lower valence band energy (–6.30 eV) than NiO (–5.50 eV), the charge carriers are transferred from Co_3O_4 to NiO to form the hole depletion region at Co_3O_4 and the hole accumulation region at NiO.[16, 41] If the amount of charge carriers is the same, their lower concentration yields a larger variation of resistance level upon the adsorption of gas molecule. Owing to the *p–p* heterojunctions between Co_3O_4 and NiO, Co_3O_4 exhibits a lower hole concentration and this contributes to higher resistance level and more sensitive gas sensing behavior as compared to the bare Co_3O_4 NRs. In order to further investigate this mechanism, a gas sensor with opposite sequences, or Co_3O_4-decorated NiO NRs were prepared and their gas sensing properties to 50 ppm of C_2H_5OH were measured (Figure 3.28). Owing to the hole accumulation region at NiO, Co_3O_4-decorated NiO NRs exhibited inferior gas responses as compared to NiO-decorated Co_3O_4. The effects of NiO decoration on Co_3O_4 were as follows: i) the crystallographic orientation changed (increase in active sites) and ii) *p–p* isotype heterojunctions (increased modulation) achieved their balance at the thickness of 1 nm to demonstrate the highest gas sensing performance,

especially toward C_6H_6. Furthermore, vertically aligned nanostructures provided enlarged surface area to gas molecules for access (utility factor) and the catalytic effect of NiO contributed to the selective detection of C_6H_6 (electronic and chemical sensitization). It is widely reported that *p*-type semiconductors including NiO and Co_3O_4 exhibit catalytic effects to various VOCs, resulting in enhanced gas sensing performance.[39] Especially, NiO is reported to be an effective catalyst for the hydrogenation of benzene and is used as a base material for the selective detection of methyl benzene.[12-14] Although the catalytic effects of NiO on aromatic substances are unclear, their close application to aromatic substances indicates their potential interaction—and thus that of NiO-decorated Co_3O_4 NRs—with aromatic substances to sensitive and selective detection of C_6H_6.

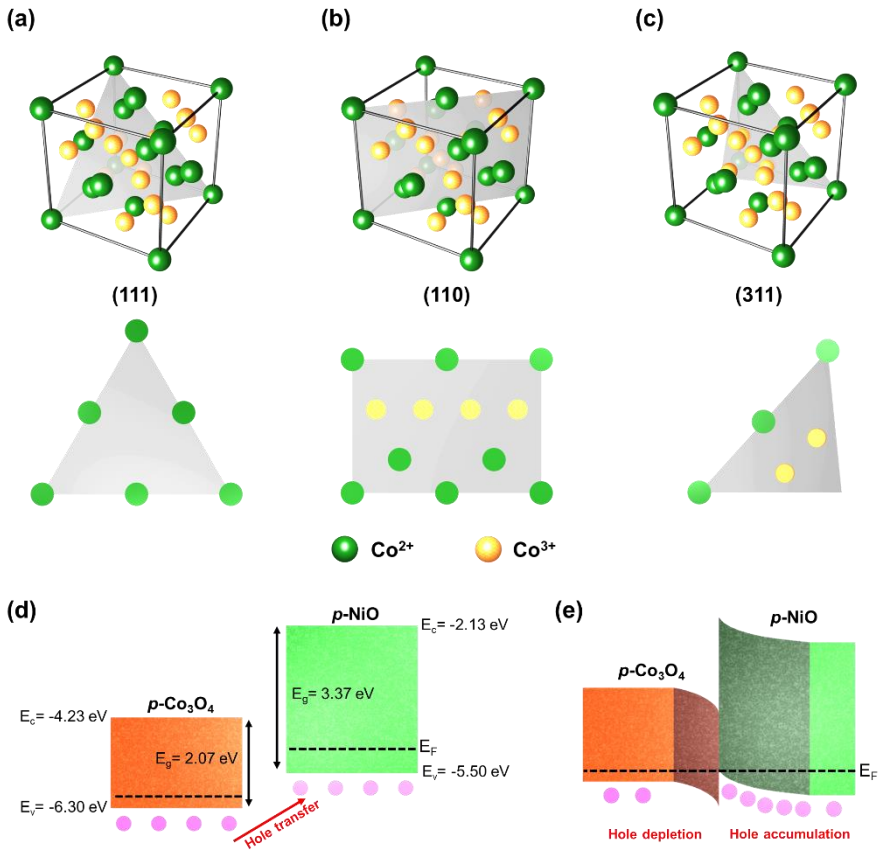

Figure 3.27. Schematic illustrations of the three-dimensional and two-dimensional surface atomic configurations in the (a) (111) plane, (b) (110) plane, and (c) (311) plane of Co_3O_4. The energy band structure of Co_3O_4/NiO heterojunctions (d) before and (e) after contact.

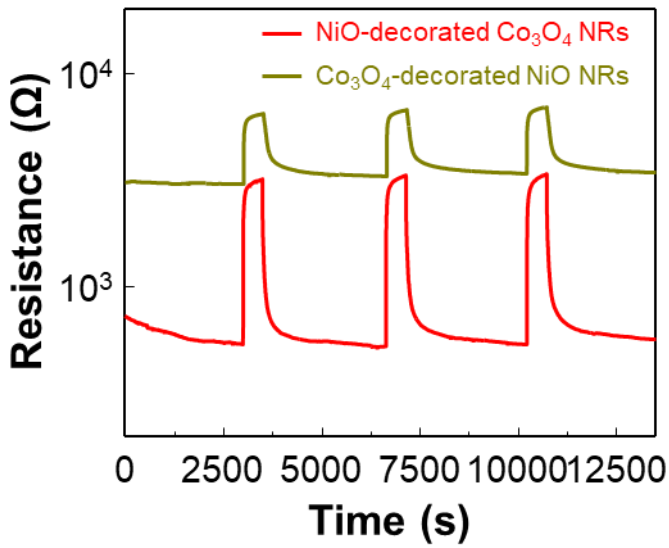

Figure 3.28. Response curves of the NiO-decorated Co_3O_4 NRs and Co_3O_4-decorated NiO NRs to three consecutive exposures of 50 ppm C_2H_5OH at 350 °C.

3.2.4. Conclusion

We demonstrated a novel type of gas sensor based on metal oxides using *p–p* isotype heterojunctions between NiO and Co_3O_4. For the effective formation of *p–p* heterojunctions on Co_3O_4 NRs, Co_3O_4 and Ni were deposited in sequence using the multiple-step GLAD method followed by the oxidization and agglomeration of Ni into NiO nanoparticles. NiO-decorated Co_3O_4 NRs exhibited enhanced gas sensing properties to various VOCs, and the response to C_6H_6 especially increased to demonstrate the selective detection of C_6H_6. The enhanced gas sensing performance can be attributed to i) increased active sites from changes in the orientation of the exposed lattice plane, ii) increased modulation upon adsorption of gas molecules owing to *p–p* heterojunctions, iii) vertically aligned nanostructures, and iv) the catalytic effects of NiO. We strongly believe that this study can provide a new perspective for improving the performance of gas sensors based on hetero-structured metal–oxide nanostructures.

3.2.5. References

[1] G. Ingrosso, *Microchem. J.* **2002**, 73, 221.

[2] T. Tang, R. Gminski, M. Könczöl, C. Modest, B. Armbruster, V. Mersch-Sundermann, *Environ. Mol. Mutagen.* **2012**, 53, 125−135.

[3] R. F. Machado, D. Laskowski, O. Deffenderfer, T. Burch, S. Zheng, P. J. Mazzone, T. Mekhail, C. Jennings, J. K. Stoller, J. Pyle, J. Duncan, R. A. Dweik, S. C. Erzurum, *Am. J. Respir. Crit. Care Med.* **2005**, 171, 1286−1291.

[4] H. G. Moon, Y.-S. Shim, D. H. Kim, M. Jeong, J. Y. Jung, S. M. Han, J. K. Kim, J.-S. Kim, H.-H. Park, J.-H. Lee, H. L. Tuller, S.-J. Yoon, H. W. Jang, *Sci. Rep.* **2012**, 2, 588.

[5] N. Barsan, C. Simion, T. Heine, S. Pokhrel, U. Weimar, *J. Electroceram.* **2010**, 25, 11−19.

[6] D. Barreca, E. Comini, A. Gasparotto, C. Maccato, C. Sada, G. Sberveglieri, E. Tondello, *Sens. Actuat. B−Chem.* **2009**, 141, 270−275.

[7] T.-H. Kim, J.-W. Yoon, Y. C. Kang, F. Abdel-Hady, A. Wazzan, J.-H. Lee, *Sens. Actuat. B−Chem.* **2017**, 240, 1049−1057.

[8] J.-W. Yoon, H.-J. Kim, I.-D. Kim, J.-H. Lee, *Nanotechnology* **2013**, 24, 444005.

[9] C. W. Na, S.-Y. Park, J.-H. Chung, J.-H. Lee, *ACS Appl. Mater. Interfaces* **2012**, 4, 6565−6572.

[10] H.-M. Jeong, H.-J. Kim, P. Rai, J.-W. Yoon, J.-H. Lee, *Sens. Actuat. B−Chem.* **2014**, 201, 482−489.

[11] W.-Y. Li, L.-N. Xu, J. Chen, *Adv. Funct. Mater.* **2005**, 15, 851−857.

[12] H.-J. Kim, J.-W. Yoon, K.-I. Choi, H. W. Jang, A. Umar, J.-H. Lee, *Nanoscale* **2013**, 5, 7066−7073.

[13] R. L. Motard, R. Burke, L. Canjar, R. Beckmann, *J. Appl. Chem.* **1957**, 7,1−14.

[14] M. M. Peng, U. J. Jeon, M. Ganesh, A. Aziz, R. Vinodh, M. Palanichamy, H. T. Jang, *Bull. Korean Chem. Soc.* **2014**, 35, 3213−3218.

[15] M. Hübner, C. Simion, *Sens. Actuat. B−Chem.* **2011**, 153, 347− 353.

[16] C. Wang, T. Wang, B. Wang, X. Zhou, X. Cheng, P. Sun, J. Zheng, G. Lu, *Sci. Rep.* **2016**, 6, 26432.

[17] N. Yamazoe, G. Sakai, K. Shimanoe, *Catal. Surv. Asia* **2003**, 7, 63−75.

[18] J.-W. Yoon, H.-J. Kim, H.-M. Jeong, J.-H. Lee, *Sens. Actuat. B−Chem.* **2014**, 202, 263−271.

[19] C. W. Na, H.-S. Woo, J.-H. Lee, *RSC Adv.* **2012**, 2, 414−417.

[20] N. Yamazoe, *Sens. Actuat. B−Chem.* **1991**, 5, 7−19.

[21] C. Wang, X. Cheng, X. Zhou, P. Sun, X. Hu, K. Shimanoe, G. Lu, N. Yamazoe, *ACS Appl. Mater. Interfaces* **2014**, 6, 12031−12037.

[22] C. Cantalini, M. Post, D. Buso, M. Guglielmi, A. Martucci, *Sens. Actuat. B−Chem.* **2005**, 108, 184−192.

[23] J.-H. Zhong, A.-L. Wang, G.-R. Li, J.-W. Wang, Y.-N. Ou, Y.-X. Tong, *J. Mater. Chem.* **2012**, 22, 5656−5665.

[24] J. Wang, Y. Chen, Y. Shen, S. Liu, Y. Zhang, *Chem. Commun.* **2017**, 53, 2978−2981.

[25] J. M. Suh, Y.-S. Shim, D. H. Kim, W.; Sohn, Y. Jung, S. Y. Lee, S. Choi, Y. H. Kim, J. M. Jeon, K. Hong, K. C. Kwon, S. Y. Park, C. Kim, J.-H. Lee, C.-Y.

Kang, H. W. Jang, *Adv. Mater. Technol.* **2017**, 2, 1600259.

[26] J.-M. Jeon, Y.-S. Shim, S. D. Han, D. H. Kim, Y. H. Kim, C.-Y. Kang, J.-S. Kim, M. Kim, H. W. Jang, *J. Mater. Chem. A* **2015**, 3, 17939−17945.

[27] T. Liu, Y. Li, G. Quan, P. Dai, X. Yu, M. Wu, Z. Sun, G. Li, *Mater. Lett.* **2015**, 139, 208−211.

[28] Y.-S. Shim, D. H. Kim, H. Y. Jeong, Y. H. Kim, S. H. Nahm, C.-Y. Kang, J.-S. Kim, W. Lee, H. W. Jang, *Sens. Actuat. B−Chem.* **2015**, 213, 314−321.

[29] Y.-S. Shim, L. Zhang, D. H. Kim, Y. H. Kim, Y. R. Choi, S. H. Nahm, C.-Y. Kang, W. Lee, H. W. Jang, *Sens. Actuat. B−Chem.* **2014**, 198, 294−301.

[30] D. H. Kim, Y.-S. Shim, J.-M. Jeon, H. Y. Jeong, S. S. Park, Y.-W. Kim, J.-S. Kim, J.-H. Lee, H. W. Jang, *ACS Appl. Mater. Interfaces* **2014**, 6, 14779−14784.

[31] Y.-S. Shim, H. G. Moon, D. H. Kim, L. Zhang, S.-J. Yoon, Y. S. Yoon, C.-Y. Kang, H. W. Jang, *RSC Adv.* **2013**, 3, 10452−10459.

[32] F. Qu, H. Jiang, M. Yang, *Mater. Lett.* **2017**, 190, 75−78.

[33] F. Qu, J. Liu, Y. Wang, S. Wen, Y. Chen, X. Li, S. Ruan, *Sens. Actuat. B−Chem.* **2014**, 199, 346− 353.

[34] X. Zhao, H. Ji, Q. Jia, M. Wang, *J. Mater. Sci.: Mater. Electron.* **2015**, 26, 8217−8223.

[35] H.-M. Jeong, J.-H. Kim, S.-Y. Jeong, C.-H. Kwak, J.-H. Lee, *ACS Appl. Mater. Interfaces* **2016**, 8, 7877− 7883.

[36] D. Zhang, C. Jiang, P. Li, Y. Sun, *ACS Appl. Mater. Interfaces* **2017**, 9, 6462−6471.

[37] F. Qu, Y. Wang, Y. Wang, J. Zhou, S. Ruan, *RSC Adv.* **2014**, 4, 24211−24216.

[38] K. Xu, L. Yang, Y. Yang, C. Yuan, *Phys. Chem. Chem. Phys.* **2017**, 19, 29601−29607.

[39] H.-J. Kim, J.-H. Lee, *Sens. Actuat. B−Chem.* **2014**, 192, 607−627.

[40] D. Liu, X. Wang, X. Wang, W. Tian, Y. Bando, D. Golberg, *Sci. Rep.* **2013**, 3, 2543.

[41] H. Zhang, S. Pokhrel, Z. Ji, H. Meng, X. Wang, S. Lin, C. H. Chang, L. Li, R. Li, B. Sun, M. Wang, Y.-P. Liao, R. Liu, T. Xia, L. Mädler, A. E. Nel, *J. Am. Chem. Soc.* **2014**, 136, 6406−6420.

Chapter 4

2D Materials with 1D Nanostructures

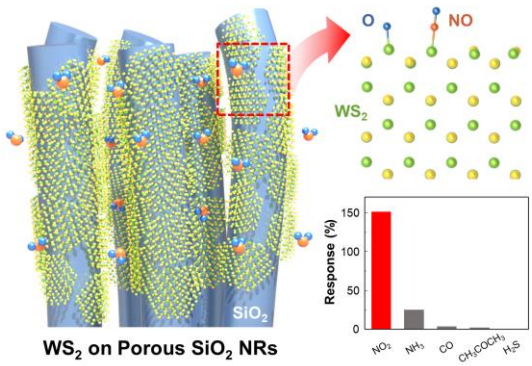

WS_2 on Porous SiO_2 NRs

Manuscript under preparation

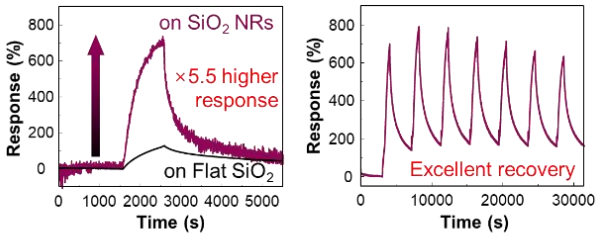

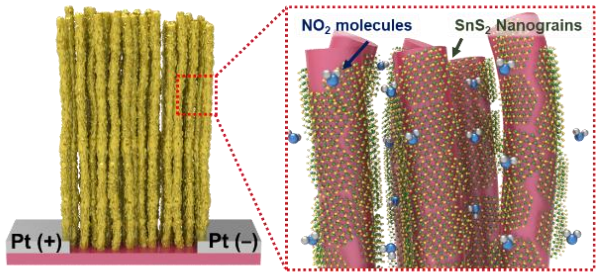

SnS_2 nanograins on SiO_2 NRs

ACS Sens. **2019**, 4(3), 678-686.

.

4.1. Tungsten disulfide on 1D silicon dioxide

4.1.1. Introduction

With the development of the Internet of Everything (IoE) market, demands for high-performance gas sensors have been sky-rocketing for the acquisition of high-quality data from surrounding environments.[1] At the same time, the gas sensors need to be scaled down as smaller as possible to be embedded into the circuits of mobile devices not to mention a low power consumption.[2] In this aspect, among various gas sensor types, chemoresistive gas sensors have been considered to be the most appropriate candidates for the IoE application since their simple device structures are advantageous to miniaturization and lowering power consumption.[3] Electrode design-dependency and complicated components in surface acoustic wave and optical gas sensors limit the miniaturization of their device structures. Furthermore, catalytic and electrochemical gas sensors consume high power due to their high operating temperature.[4] Though current chemoresistive metal oxide-based gas sensors require high operating temperature near 300 °C, there have been plenty of successful approaches to reduce power consumption: i) light-activation[5, 6], ii) noble metal decoration[7, 8], iii) heterojunction engineering[9-12], and iv) utilization of non-oxide materials[13, 14]. However, noble metal decoration and heterojunction engineering were more effective in diversifying selectivity of the gas sensors enabling reasonable detection at a little lower temperature but less effective in further lowering overall operating temperature to near room temperature. The light-activated gas sensors operate well at room temperature but still, light sources consume a significant amount of power. Therefore, the active gas sensing materials

themselves should be replaced by other sensitive materials capable of room-temperature operation.

The 2-dimensional (2D) materials have been considered as promising active materials to replace conventional metal oxides since their high surface-to-volume ratio and high surface energy enable adsorption and desorption of target gas molecules even at room temperature. The 2D materials for gas sensor application include graphene[15], graphene derivatives[16], transition metal dichalcogenides (TMDs)[17], or layered perovskites[18, 19]. Since graphene and its derivatives are intrinsically metallic with difficulties in utilizing their excellent electronic properties by opening a gap at the Dirac cone, TMDs including MoS_2, WS_2, SnS_2, or NbS_2 which are intrinsic semiconductors have been widely adopted as active materials for chemoresistive gas sensors.[20-23] The layered perovskites are recently adopted gas sensing materials but still suffer their widely known relatively unstable storage under ambient air and humidity.[18, 19] One of the most notable characteristics of TMDs is their edge sites having many dangling bonds and high reactivity due to high *d*-orbital electron density.[24] The TMDs have lattice structures of transition metal atoms at the middle layer sandwiched by chalcogen atoms (S, Se, and Te) on top and bottom. Therefore, edge sites of TMDs can expose highly reactive transition metal atoms to the ambient air while only a limited number can be exposed at the basal plane of TMDs through chalcogen defects. The highly reactive edge sites of TMDs have recently been reported for gas sensor application and considered as the most effective strategies to overcome relatively low gas responses and incomplete recovery characteristics exhibited by bulk planar TMDs at room temperature.[25] However, still,

further efforts on the improvement of gas sensing properties by edge sites of TMDs are required to satisfy high standards for the IoE application.

Herein, we fabricated edge-exposed WS_2 synthesized on SiO_2 nanorods (NRs), named as WS_2 NRs, to achieve highly sensitive and selective NO_2 detection at room temperature. Our previous studies already revealed TMDs synthesized on SiO_2 NRs exhibited a large number of edge sites.[20] In addition, highly porous SiO_2 NRs template realized numerous WS_2 edge sites in a limited active area to achieve promising gas sensing properties that have not been reported using WS_2 according to the best of the author's knowledge. We deposited 500 nm-thick SiO_2 NRs by glancing angle deposition (GLAD) method using an e-beam evaporator with precisely controlled SiO_2 NRs porosity. The WCl_6 precursor solution was spin-coated on the SiO_2 NRs and sulfurized using a chemical vapor deposition (CVD) system. The edge-exposed WS_2 NRs exhibited a gas response of 151.2% to 5 ppm NO_2 at room temperature and the theoretical detection limit was calculated to be 13.726 ppb. The WS_2 NRs also exhibited stable operation under both dry and humid conditions. The highly selective behavior toward NO_2 was interpreted by density functional theory (DFT) calculation. The promising gas sensor performance by WS_2 NRs can provide possible future pathways and perspective of gas sensors based on 2D materials toward IoE applications.

4.1.2. Experimental procedures

Fabrication of SiO_2 NRs. After preparation of Pt-interdigitated electrodes (Pt-IDEs) with 5 μm spacing through photolithography and deposition of Pt/Ti (100/30 nm) on SiO_2 (300 μm)/Si substrates, the GLAD method using e-beam evaporator was conducted to deposit SiO_2 NRs with 500 nm thickness. The glancing angles were 75˚, 77.5˚, 80˚, 82.5˚, and 85˚ with a rotation speed of 80 rpm. SiO_2 grains (Kojundo Chemistry) were used for the evaporation. The base pressure of the chamber was maintained at 2×10^{-6} Torr, and the growth rate was 2.0 Å/s.

Synthesis of WS_2 on porous SiO_2 NRs. After deposition of SiO_2 NRs, the fabricated samples were treated with UV-O_3 cleaner (Jelight Company Inc. Model 30) for 15 min. The treated samples were then spin-coated (3500 rpm for 60s) with filtered 500 mM WCl_6 (99.9% purity, Merck) precursor solution diluted in ethylene glycol solvent. After drying at 50 ℃ for 5 min, the samples were placed in a home-built CVD system with sliding rails for two separate furnaces each for sulfur and samples. Inside the quartz tube of the CVD system, 0.5g of sulfur powder and precursor-coated SiO_2 NRs were placed at each position. Under constant flow of N_2 and H_2 (500 and 100 sccm), each furnace was heated up to 330 ℃ (for sulfur) and 700 ℃ (for sample), respectively for 30 min at out of position. After 30 min, the furnace for sulfur was slid into the right position and maintained for 5 min. After 5 min, the furnace for samples was slid into the right position and maintained for 60 min. After 60 min, both furnaces were turned off and cooled for 40 min under a fan.

Characterization. The top-view and cross-sectional morphologies were characterized by a field-emission scanning electron microscopy (FESEM, SU-70)

using an acceleration voltage of 5 kV and a working distance of 8 mm. Bright-field and high-resolution TEM images were obtained with a field-emission transmission electron microscopy (FETEM, JEM-2100F). The chemical mapping of WS_2 NRs was obtained by EDS detector installed in FETEM. Raman spectroscopy (LabRAM HR, Horiba) and XPS (Sigma Probe, ThermoFisher Scientific) were conducted to characterize synthesized WS_2.

Gas sensing measurement. Gas sensing measurement was done in a quartz tube with a furnace (Lindberg/Blue™ Mini-Mite™). The furnace was used to maintain the quartz tube at room temperature (25 °C). The gas was injected in a repeating sequence of dry air and target gas (balanced with dry air, Sinjin Gases) through an automated mass flow control system. For the humidity, a controlled flow of dry air was injected into the bubbler to produce H_2O vapor. A constant flow of 1000 sccm was maintained throughout the measurements. The response to target gas was measured at a DC bias voltage of 0.5 V using a sourcemeter (Keithley 2400).

4.1.3. Results and discussion

The GLAD method using an e-beam evaporator is a widely adopted technique for the fabrication of vertically aligned 1-dimensional (1D) nanostructures. As shown in the schematic illustration in Figure 4.1a, SiO_2 sources located at the bottom of the vacuum chamber are evaporated by e-beam irradiation and SiO_2 vapors are deposited at the SiO_2/Si substrates located 50 cm above the sources. When the substrates are tilted with a rotation, vertically aligned 1D nanostructures can be constructed. Figure 4.2a represents schematic illustrations of initial nucleation with following shadow effects depending on glancing angles of the substrates during GLAD and resulting SiO_2 NRs with varying porosity. Since the substrates rotate, all the lateral vectors of SiO_2 vapor flux are canceled out and only vertical vectors of SiO_2 vapor flux are valid for the deposition, yielding vertically aligned SiO_2 NRs.[26] As the glancing angle increases ($\theta_1 < \theta_2 < \theta_3$), emerging shadows caused by initially deposited nucleus get larger and no further deposition can happen in the shadow area. As a result, inter-distance between SiO_2 NRs, or porosity can be controlled by manipulating the glancing angle of the substrates. Excessively low porosity can have almost no difference to planar film and excessively high porosity can lose electric conduction path through the nanostructures. To achieve the highest available porosity without electric open circuit, SiO_2 NRs with 500 nm thickness at five different glancing angles (75˚, 77.5˚, 80˚, 82.5˚, and 85˚) were prepared for the optimization. The deposited SiO_2 NRs were treated with UV-O_3 cleaner and 500 mM WCl_6 precursor solution was spin-coated on them. Under the constant flow of H_2 and N_2, the prepared samples were sulfurized using the CVD system to result in WS_2

synthesized on porous SiO_2 NRs (Figure 4.1b). Since SiO_2 NRs are insulator and used only as a porous template for WS_2 synthesis, we call the final resultant sample as WS_2 NRs. The top-view and cross-sectional view scanning electron microscopy (SEM) images of plain WS_2 thin film and fabricated WS_2 NRs are shown in Figure 4.2b-g. From top-view SEM images, while WS_2 NRs deposited at 75˚ show very low porosity, WS_2 NRs deposited at 85˚ show highly porous nanostructures. The cross-sectional view SEM images in insets show WS_2 uniformly covering SiO_2 NRs for all WS_2 NRs. For WS_2 NRs deposited at 85˚, extremely high porosity even exposed significant amount of bottom planar surface area where SiO_2 NRs were not deposited.

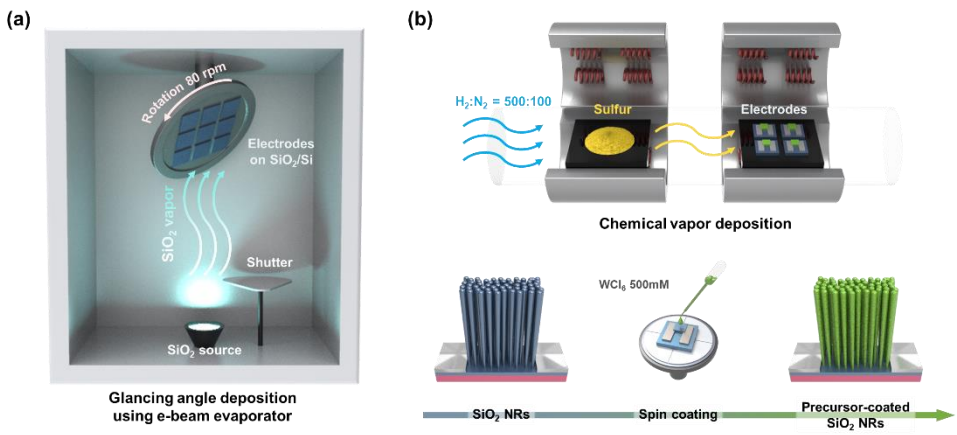

Figure 4.1. Schematic illustrations of (a) a glancing angle deposition method using e-beam evaporator and (b) preparation of precursor-coated SiO_2 NRs and sulfurization process using chemical vapor deposition system.

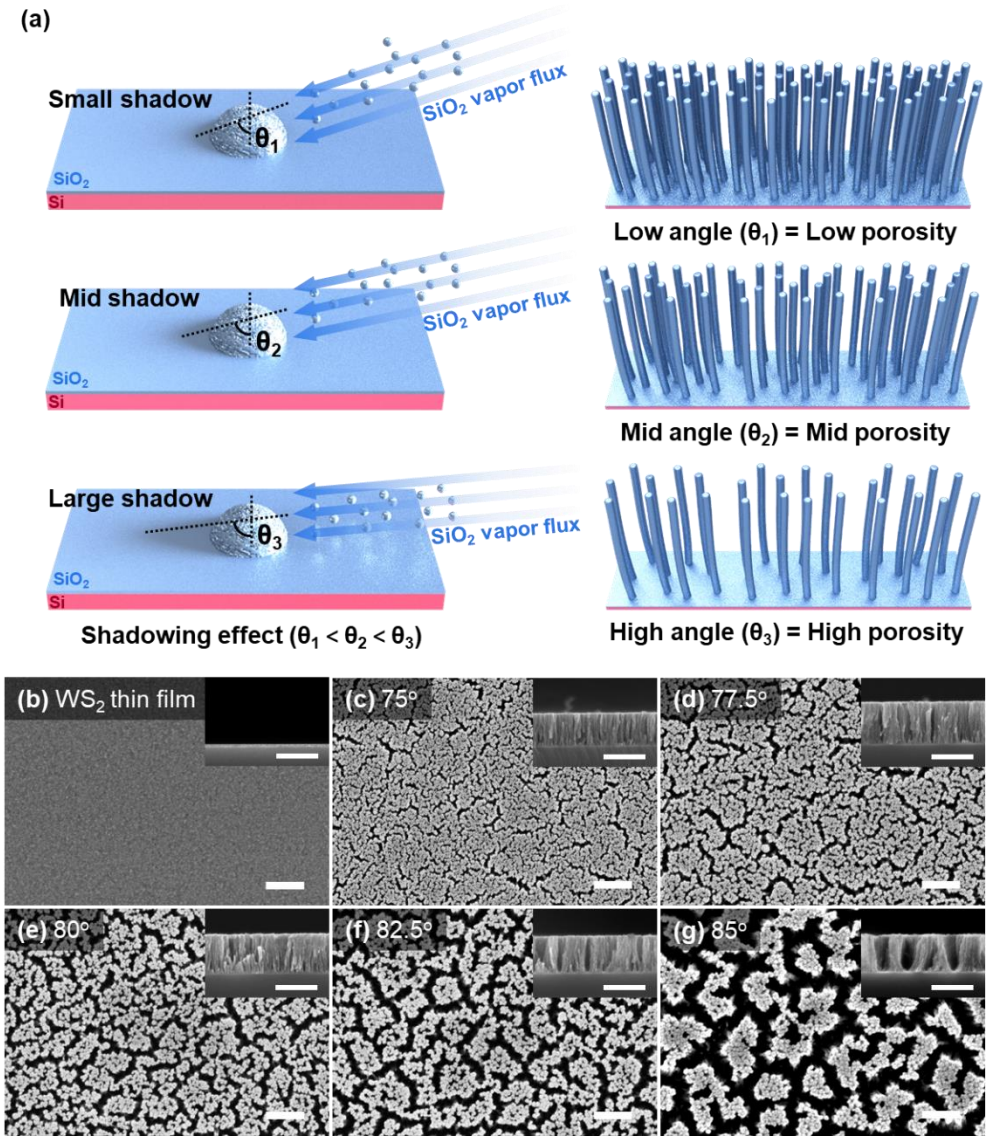

Figure 4.2. (a) Schematic illustrations of initial nucleation with following shadowing effects depending on glancing angles of the substrate during glancing angle deposition (GLAD) and resulting SiO_2 NRs with varying porosity. Top-view and cross-sectional view (insets) scanning electron microscopy (SEM) images of (b) plain WS_2 thin film and (c-g) WS_2 NRs at a glancing angle of (c) 75 (d) 77.5 (e) 80˚, (f) 82.5˚, and (g) 85˚. Scale bars indicate 500 nm.

Further structural characterization was conducted with transmission electron microscopy (TEM) and electron dispersive spectroscopy (EDS) analysis as shown in Figure 4.3a-i. Figure 4.3a shows a cross-sectional scanning transmission electron microscopy (STEM) image of WS_2 NRs. WS_2 uniformly covering SiO_2 NRs can clearly be identified. The magnified STEM image in a red square area in Figure 4.3a is shown in Figure 4.3b, and further magnified STEM image in a yellow square area in Figure 4.3b is presented in Figure 4.3c. As clearly seen in Figure 4.3c, edge sites of WS_2 are well-exposed and black regions in Figure 4.3b all indicate edge-exposed WS_2. Compared to WS_2 grain growth on a planar substrate, WS_2 grain growth on SiO_2 NRs has a limitation in the maximum available domain size and that can lead to a large number of grain boundaries and more exposed edge sites of WS_2.[22] High-resolution (HR) TEM images in Figure 4.3d shows hexagonal coordination of W atoms and S atoms with 0.27 nm *d*-spacing in (100) direction. The selected area diffraction (SAED) pattern in Figure 4.3e shows a diffraction pattern of WS_2 ($P6_3/mmc$) crystal. Figure 4.3f-i correspond to EDS analysis data of WS_2 NRs and uniformly coated WS_2 on SiO_2 NRs deposited on SiO_2/Si substrates can be clearly confirmed. The Raman spectroscopy data for plain WS_2 thin film and WS_2 NRs in Figure 4.3j shows E^1_{2g} peak which stands for lateral vibration modes located at 351.517 cm^{-1} and A_{1g} peak which stands for vertical vibration modes located at 415.595 cm^{-1}, indicating well-synthesized WS_2. The X-ray photoelectron spectroscopy (XPS) analysis also confirmed well-synthesized WS_2 with distinctive peaks as shown in Figure 4.3k and l. The peaks for W $5p_{2/3}$, W $4f_{5/2}$, W $4f_{7/2}$, S $2p_{1/2}$, and S $2p_{3/2}$ were found at 38 eV, 34.8 eV, 32.6 eV, 163.4 eV, and 162.2 eV,

respectively. Wide scan XPS spectra for WS_2 NRs are presented in Figure 4.4.

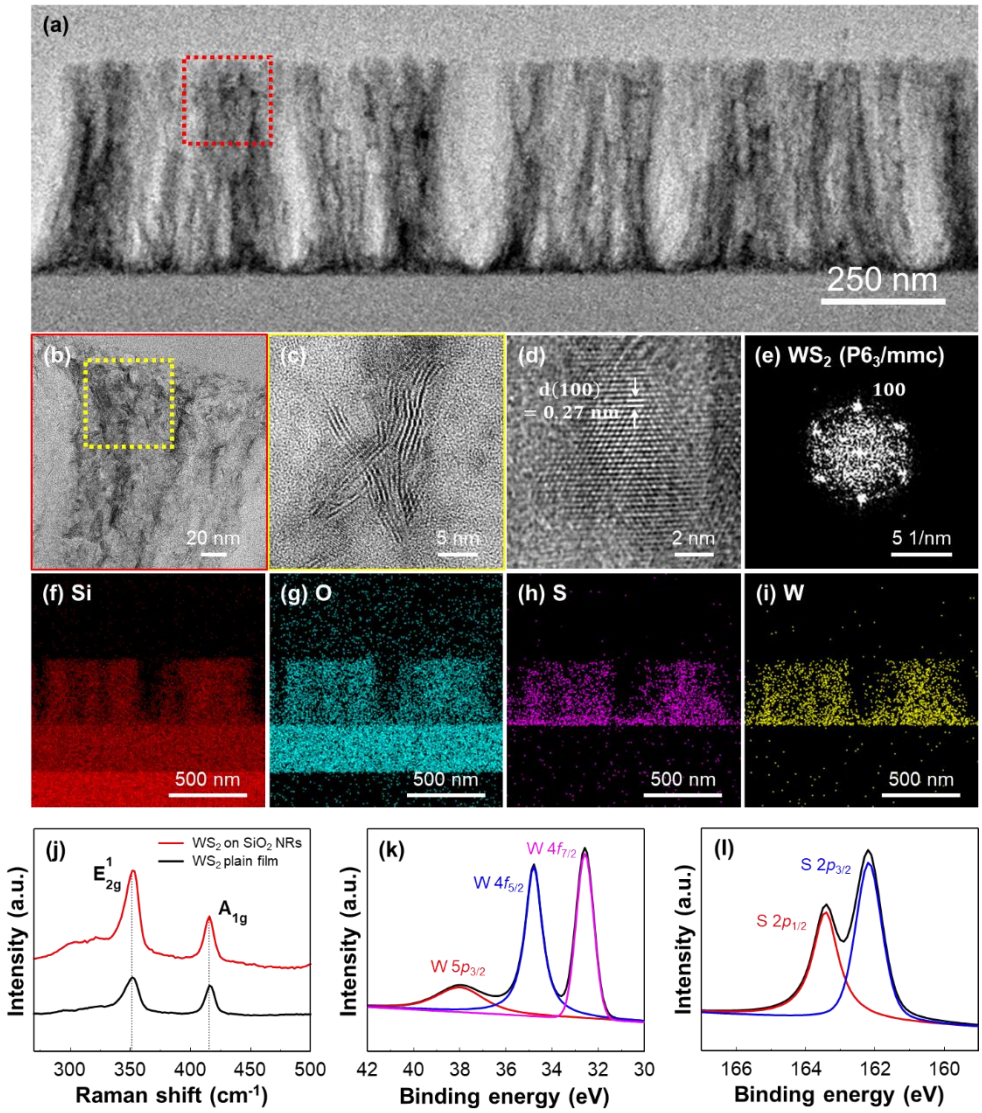

Figure 4.3. (a-c) Cross-sectional scanning transmission electron microscopy (STEM) images in a (a) low, (b) mid, and (c) high magnification; (d) High-resolution TEM, (e) selected area diffraction (SAED) pattern images, and (f-i) Energy-dispersive X-ray spectroscopy (EDS) mapping of (f) Si, (g) O, (h) S, and (i) W of WS_2 NRs. (j) Raman spectra of synthesized WS_2 NRs and plain SiO_2/Si substrate. The X-ray photoelectron spectroscopy (XPS) core level spectra of (k) W 4*f* and (l) S 2*p* for WS_2 NRs.

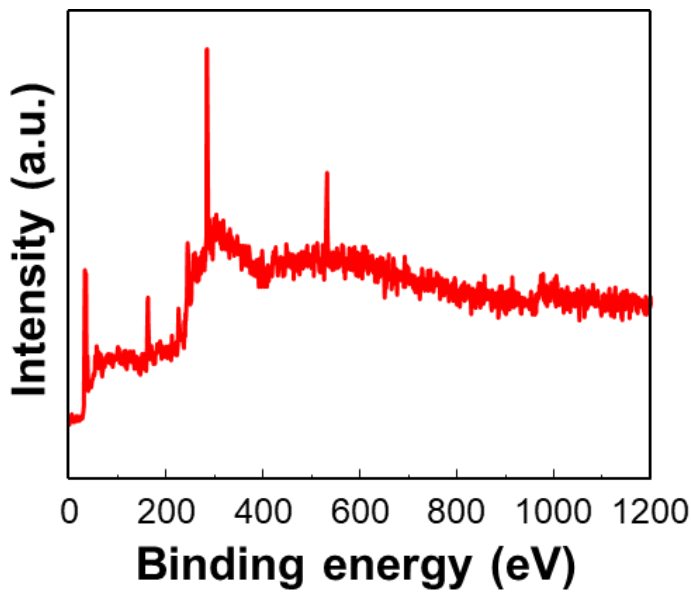

Figure 4.4. Wide scan XPS spectra for WS_2 NRs.

The WS_2 NRs synthesized at five different glancing angles were then exposed to 5 ppm NO_2 at room temperature to investigate optimal porosity conditions for the gas sensing applications. The gas response can be calculated as $(R_{air} - R_{gas})/R_{gas} \times 100$ (%), where R_{air} and R_{gas} denote resistance under exposure to synthetic air and target gas, respectively. As shown in Figure 4.5a, WS_2 NRs deposited at 75˚ exhibited a gas response of 12.72% as low as plain WS_2 thin film (22.96%), indicating porosity formed at 75˚ has almost no contribution to gas sensing properties of WS_2 NRs. The WS_2 NRs deposited at higher glancing angles than 75˚ exhibited enhanced gas responses due to higher porosity. The gas response for WS_2 NRs deposited at 77.5˚, 80˚, 82.5˚, and 85˚ were 90.88%, 115.85%, 151.24%, and 95.59%, respectively. As porosity increases with higher glancing angles, gas responses also increase up to a glancing angle of 82.5˚ and decrease after 82.5˚ (Figure 4.5b). Too high porosity introduces the bottom planar region under WS_2 NRs as already shown in Figure 4.2g to target gas molecules and eventually taking less advantages of increased surface area of the 1D nanostructures for the gas sensing application. The inset in Figure 4.5b shows base resistance values for each WS_2 NR and it keeps increasing for higher glancing angles due to larger inter-distance between each WS_2 NR resulting in less conduction path (plain WS_2 thin film = 1399.12 Ω). Collectively, WS_2 NRs deposited at 82.5˚ exhibited the most effective porosity for the gas molecule interactions.

Further gas sensing properties of WS_2 NRs deposited at 82.5˚ were investigated as shown in Figure 4.6a-d. The WS_2 NRs were exposed to four consecutive pulses of NO_2 with low concentrations of 400, 600, 800, and 1000 ppb to figure out their detection limit (Figure 4.6a). The gas responses were plotted as a function of NO_2

concentration as shown in Figure 4.6b, and they exhibited an excellent linear relationship with a slope of 5.965 ppm^{-1}. Although the lowest gas concentration tested in this study was 400 ppb, the theoretical detection limit can be calculated by extrapolating the linear relation curve to the lowest possible NO_2 concentration where the noise-to-signal ratio reaches three. The noise level can be calculated using variation in resistance change before exposure to NO_2 using the root-mean-square deviation.[27] As a result, the theoretical detection limit was calculated to be as low as 13.726 ppb. American Society of Heating, Refrigerating and Air-Conditioning Engineers (ASHRAE) standards for indoor air pollutant states indoor air concentration of NO_2 as 50 ppb.[28] The extremely low detection limit toward NO_2 exhibited by WS_2 NRs in this study can sufficiently satisfy the requirement for indoor air monitoring. Further gas sensing properties under humidity were investigated as shown in Figure 4.7a. WS_2 NRs were exposed to two pulses of 5 ppm NO_2 under both dry and humid conditions (relative humidity 50%). The presence of humidity improved recovery characteristics with a still moderate gas response (44.94%). For stability test, WS_2 NRs were exposed to ten consecutive pulses of 5 ppm NO_2 as shown in Figure 4.6c. Although recovery was not complete and there is a little shift in base resistance, stable operation upon multiple exposures to NO_2 was verified. The stability under three-day storage was also confirmed as shown in Figure 4.7b. The gas responses toward various gases including 5 ppm NO_2, 50 ppm NH_3, 500 ppm CO, 50 ppm CH_3COCH_3, and 5 ppm H_2S were also investigated for selectivity study. Although tested concentrations were different for each gas species due to our experimental setup, NO_2 with the lowest concentration among tested gases was the

most selectively detected gas species by WS_2 NRs. The highly sensitive and selective NO_2 detection achieved by WS_2 NRs in this study has not been reported in performance-wise to the best of the author's knowledge compared to previously reported WS_2-based NO_2 gas sensors as shown in Table 4.1.[29-37] The previous studies incorporated various noble metal catalysts or utilized nanostructures but no reports were as effective as WS_2-covered SiO_2 NRs, or WS_2 NRs for NO_2 detection at room temperature. Although there are some reports of forming heterojunctions with MoS_2[38] or ZnS[39] being more effective (798% and 3250% to 5 ppm NO_2, respectively), it is notable that WS_2 NRs in this study achieved the excellent gas sensing properties relying solely on WS_2 properties. In other words, incorporating heterojunctions with other materials to WS_2 NRs could yield further improved gas sensing properties.

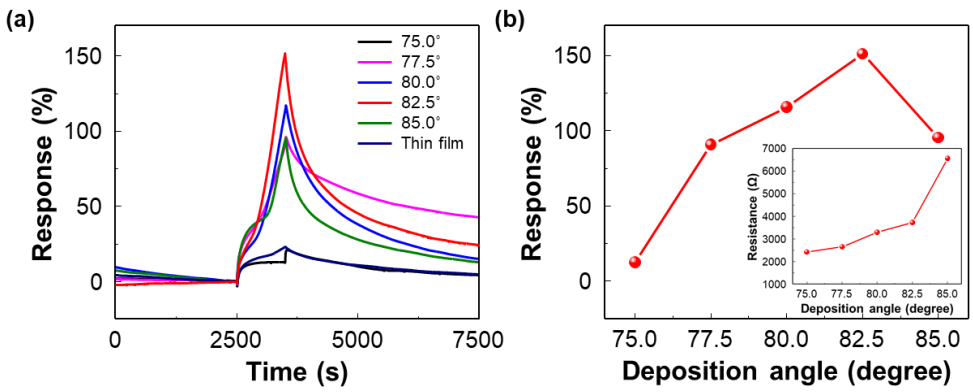

Figure 4.5. (a) Response curves and (b) responses and resistance change (inset) of WS_2 thin film and WS_2 NRs deposited at different glancing angles (75, 77.5, 80, 82.5, and 85˚) to 5 ppm NO_2 at room temperature.

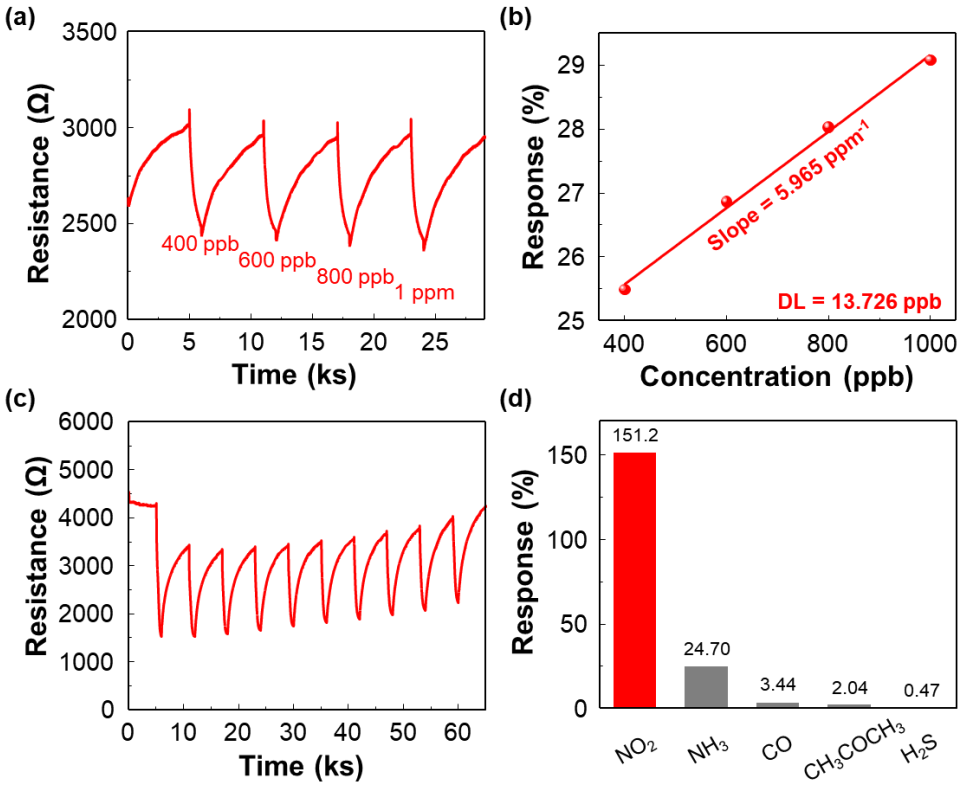

Figure 4.6. (a) Response curves and (b) calibration of responses for WS_2 NRs toward 0.4−1 ppm NO_2 at room temperature. Responses of WS_2 NRs to (c) 10 pulses of 5 ppm of NO_2 and (d) various gases at room temperature.

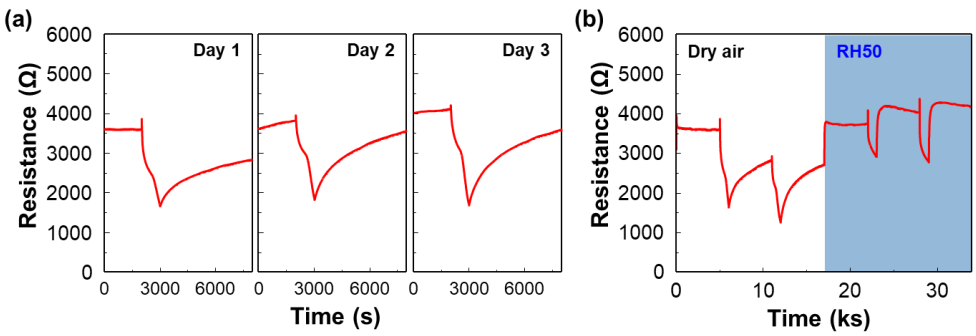

Figure 4.7. Response curves of WS_2 NRs toward 5 ppm NO_2 at room temperature (b) under relative humidity (RH) 50%, and (a) under dry condition for 3 days of storage.

Table 4.1. Comparison of gas sensor performances of the recently reported WS_2-based NO_2 gas sensors

Sensing Materials	Conc. (ppm)	Response (%)	Operating Temp. (°C)	Ref.	Year
WS_2 Nanosheets + Ag Nanowire	25	58.0	100	[29]	2016
WS_2 Nanoflakes Functionalized Carbon Nanofibers	5	20.5	RT	[30]	2017
WS_2 Nanosheets + Pt Quantum Dots	20	1.9	RT	[31]	2018
WS_2 Nanosheets	5	68.4	RT	[32]	2018
WS_2 Nanoplates in Hollow Carbon Nanocages	5	48.2	RT	[33]	2018
WS_2 Nanosheets + Au Nanoparticles	50	60.0	31.7	[34]	2019
WS_2 Nanoparticles	10	15.2	100	[35]	2019
WS_2 Nanocrystallites-embedded WS_2 Nanofibers	10	39.0	60	[36]	2020
WS_2 Nanosheets	5	121.0	160	[37]	2020
WS_2 Synthesized on SiO_2 NRs	5	**151.2**	**RT**	**This work**	

The promising gas sensing performances of WS_2 NRs can mainly be attributed to vertically aligned 1D nanostructure and the edge sites rich nature of WS_2 NRs. Highly porous 1D nanostructures with extremely high surface-to-volume ratio provided large enough surface area for WS_2 to be exposed to target gas molecules in a limited active area. In addition, WS_2 growth on porous SiO_2 NRs induced a large number of grain boundaries leading to more edge sites exposed WS_2, as explained previously. The interaction of WS_2 NRs with gas molecules can occur in two pathways at room temperature: i) oxygen ion-mediated interaction and ii) direct interaction with WS_2. The oxygen ion-mediated interaction occurs through adsorbed oxygen ions on the surface of WS_2. The active semiconducting materials for gas sensors adsorb oxygen molecules in ambient air in three different shapes (O_2^-, O^-, O^{2-}) depending on operating temperature.[40] At room temperature, not enough energy to overcome activation energy for ionization leads to adsorption in either neutral oxygen molecule ($O_{2(ads)}$) or ionized oxygen molecule ($O_2^-{}_{(ads)}$) at the sulfur vacancies at the basal plane or reactive edge sites of WS_2.[41] Although adsorption of ionized O_2^- molecular form is theoretically more likely to take place at the temperature over 100 °C,[42] Liu *et al.* experimentally revealed the existence of $O_2^-{}_{(ads)}$ molecular form even at room temperature by measuring conductance under pure N_2 and pure O_2.[43] The adsorbed $O_2^-{}_{(ads)}$ can interact with NO_2 gas molecules as the following equations.

$$O_{2(gas)} + e^- \rightarrow O_2^-{}_{(ads)} \quad (1)$$

$$O_2^-{}_{(ads)} + NO_{2(gas)} \rightarrow O_{2(gas)} + NO_2^-{}_{(ads)} \quad (2)$$

Although oxygen ion-mediated interaction is one of the possible gas sensing mechanisms at room temperature as explained, however, it is more reasonable to assume a larger portion of neutral $O_{2(ads)}$ adsorption than ionized $O_2^-{}_{(ads)}$ at reactive sites at room temperature. When exposed to NO_2 gas, a little $O_2^-{}_{(ads)}$ participate in the NO_2 sensing and many O_2(ads) get desorbed from the active sites, which are now open to direct interaction with NO_2 molecules. Since kinetics of $O_{2(ads)}$ desorption and NO_2 direct adsorption are slow at room temperature, response time is very slow as exhibited by experimental data. Although both reactive edge sites and sulfur vacancies at the basal plane can participate in gas sensing as reactive sites, any possible configurations of edge sites (metal termination or chalcogen termination) of TMDs possess higher adsorption energy than basal plane according to S.-Y. Cho *et al.*[25] Therefore, more edge sites of WS_2 can yield to a stronger interaction with target gas molecules. Since WS_2 NRs fabricated in this study have numerous edge-exposed WS_2 induced by limitation in grain growth and resultant smaller sized nanograins, WS_2 NRs exhibited unexpectedly high response toward 5 ppm NO_2.[22]

To interpret the impressive selectivity of WS_2 NRs toward NO_2, DFT calculation was conducted to compare binding energies to WS_2 edge sites for each different gas species (NO_2, NH_3, CO, CH_3COCH_3, and H_2S). Figure 4.8a-e show the most favorable configuration for each gas species and Figure 4.8f summarizes calculated binding energy for each gas species. The gas molecules interact with semiconducting materials through either chemisorption or physisorption. According to the calculation, chemisorption was preferred for NO_2 and NH_3, and physisorption was preferred for CO, CH_3COCH_3, and H_2S. Rather than NO_2 binding to WS_2 edge sites

in a molecular form, binding in a dissociated form of NO and O was more likely to happen with the calculated binding energy of 8.51 eV as shown in Figure 4.8a. NH_3 can have three possible configurations: i) physisorption (NH_3), ii) chemisorption ($NH_3 \rightarrow NH_2 + H$), and iii) another chemisorption ($NH_3 \rightarrow NH + 2H$). The binding energy for each case was 3.25 eV, 4.11 eV, and 4.51 eV, respectively, and the second chemisorption ($NH_3 \rightarrow NH + 2H$) was calculated to be the most favorable configuration as shown in Figure 4.8b. For other gases including CO, CH_3COCH_3, and H_2S, physisorption was preferred and binding energy was calculated as 3.64 eV, 2.29 eV, and 1.59 eV, respectively. All calculated binding energies of the most favorable configuration for all gas species are summarized in Figure 4.8f. The calculation results on selectivity well match with the experimental selectivity data presented in Figure 4.6d, indicating direct interaction with WS_2 is a primary gas sensing mechanism in our WS_2 NRs.

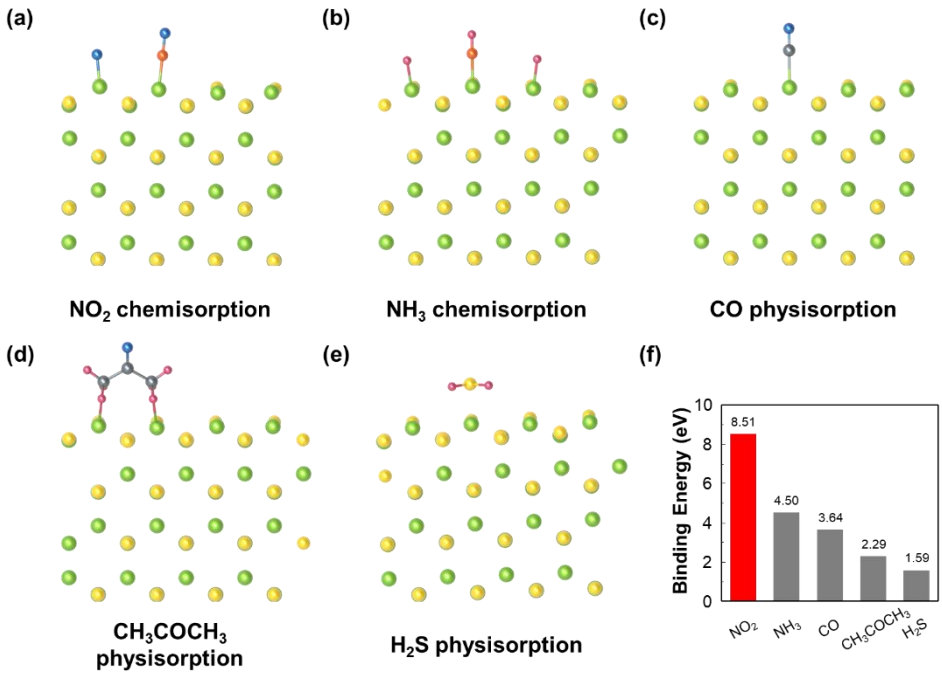

Figure 4.8. (a) Schematic illustrations of WS_2 lattice configurations experiencing (a) NO_2 chemisorption (b) NH_3 chemisorption (c) CO physisorption (d) CH_3COCH_3 physisorption and (e) H_2S physisorption, respectively. (f) Calculated binding energy values for each gas species.

4.1.4. Conclusion

In summary, the highly sensitive and selective NO_2 detection that has not been reported in performance-wise to the best of the author's knowledge achieved by WS_2 NRs in this study can be attributed to two major contributions: i) highly porous 1D nanostructures and ii) numerous edge-exposed WS_2 synthesized on highly porous SiO_2 NRs template. Chemically reactive edge sites of WS_2 served as highly favorable active sites for direct interaction with target gas molecules. Well-matching experimental data and DFT calculation results on promising NO_2 selectivity suggest a direct interaction of target gas molecules with edge sites of WS_2 is more favorable than oxygen ion-mediated gas sensing. The excellent gas sensor performance exhibited by WS_2 NRs can suggest possible future pathways and perspective of gas sensors based on 2D materials toward IoE applications.

4.1.5. References

[1] R. A. Potyrailo, *Chem. Rev.* **2016**, 116, 11877-11923.

[2] R. Prajesh, N. Jain, A. Agarwal, *Microsyst. Technol.* **2016**, 22, 2185-2192.

[3] Y. G. Song, Y.-S. Shim, J. M. Suh, M.-S. Noh, G. S. Kim, K. S. Choi, B. Jeong, S. Kim, H. W. Jang, B.-K. Ju, C.-Y. Kang, *Small* **2019**, 15, 1902065.

[4] H. Nazemi, A. Joseph, J. Park, A. Emadi, *Sensors* **2019**, 19, 1285.

[5] M. M. Hashemi, A. Nikfarjam, H. Hajghassem, N. Salehifar, *J. Phys. Chem. C* **2020**, 124, 322-335.

[6] C. B. Jacobs, A. B. Maksov, E. S. Muckley, L. Collins, M. Majouri-Samani, A. Ievlev, C. M. Rouleau, J.-W. Moon, D. E. Graham, B. G. Sumpter, I. N. Ivanov. *Sci. Rep.* **2017**, 7, 6053.

[7] Y.-S. Shim, B. Jang, J. M. Suh, M. S. Noh, S. Kim, S. D. Han, Y. G. Song, C.-Y. Kang, H. W. Jang, W. Lee, *Sens. Actuat. B−Chem.* **2018**, 255, 1841-1848.

[8] D. H. Kim, T. H. Kim, W. Sohn, J. M. Suh, Y.-S. Shim, K. C. Kwon, K. Hong, S. Choi, H.-G. Byun, J.-H. Lee, H. W. Jang, *Sens. Actuat. B−Chem.* **2018**, 274, 587-594.

[9] J. M. Suh, Y.-S. Shim, D. H. Kim, W. Sohn, Y. Jung, S. Y. Lee, S. Choi, Y. H. Kim, J.-M. Jeon, K. Hong, K. C. Kwon, S. Y. Park, C. Kim, J.-H. Lee, C.-Y. Kang, H. W. Jang, *Adv. Mater. Technol.* **2017**, 2, 1600259.

[10] J. M. Suh, W. Sohn, Y.-S. Shim, J.-S. Choi, Y. G. Song, T. L. Kim, J.-M. Jeon, K. C. Kwon, K. S. Choi, C.-Y. Kang, H.-G. Byun, H. W. Jang, *ACS Appl. Mater. Interfaces* **2017**, 10, 1050-1058.

[11] Y. G. Song, J. Y. Park, J. M. Suh, Y.-S. Shim, S. Y. Yi, H. W. Jang, S. Kim, J. M. Yuk, B.-K. Ju, C.-Y. Kang, *Chem. Mater.* **2018**, 31, 207-215.

[12] S. Y. Yi, Y. G. Song, J. Y. Park, J. M. Suh, G. S. Kim, Y.-S. Shim, J. M. Yuk, S. Kim, H. W. Jang, B.-K. Ju, C.-Y. Kang, *ACS Appl. Mater. Interfaces* **2019**, 11, 7529-7538.

[13] B. Liu, X. Liu, Z. Yuan, Y. Jiang, Y. Su, J. Ma, H. Tai, *Sens. Actuat. B−Chem.* **2019**, 295, 86-92.

[14] J. M. Suh, Y.-S. Shim, K. C. Kwon, J.-M. Jeon, T. H. Lee, M. Shokouhimehr, H. W. Jang, *Electron. Mater. Lett.* **2019**, 15, 368-376.

[15] Y. H. Kim, Y. S. Choi, S. Y. Park, T. Kim, S.-P. Hong, T. H. Lee, C. W. Moon, J.-H. Lee, D. Lee, B. H. Hong, H. W. Jang, *Nanoscale* **2019**, 11, 2966-2973.

[16] S. Y. Park, Y. H. Kim, S. Y. Lee, W. Sohn, J. E. Lee, Y.-S. Shim, K. C. Kwon, K. S. Choi, H. J. Yoo, J. M. Suh, M. Ko, J.-H. Lee, M. J. Lee, S. Y. Kim, M. H. Lee, H. W. Jang, *J. Mater. Chem. A* **2018**, 6, 5016-5024.

[17] S. Y. Park, J. E. Lee, Y. H. Kim, J. J. Kim, Y.-S. Shim, S. Y. Kim, M. H. Lee, H. W. Jang, *Sens. Actuat. B−Chem.* **2018**, 258, 775-782.

[18] H. Chen, M. Zhang, R. Bo, C. Barugkin, J. Zheng, Q. Ma, S. Huang, A. W. Y. Ho-Baillie, K. R. Catchpole, A. Tricoli, *Small* **2018**, 14, 1702571.

[19] H. Chen, M. Zhang, X. Fu, Z. Fusco, R. Bo, B. Xing, H. T. Nguyen, C. Barugkin, J. Zheng, C. F. J. Lau, S. Huang, A. W. Y. Ho-Baillie, K. R. Catchpole, A. Tricoli, *Phys. Chem. Chem. Phys.* **2019**, 21, 24187.

[20] Y.-S. Shim, K. C. Kwon, J. M. Suh, K. S. Choi, Y. G. Song, W. Sohn, S. Choi, K. Hong, J.-M. Jeon, S.-P. Hong, S. Kim, S. Y. Kim, C.-Y. Kang, H. W. Jang, *ACS Appl. Mater. Interfaces* **2018**, 10, 31594-31602.

[21] Y. H. Kim, K. C. Kwon, S. Kang, C. Kim, T. H. Kim, S.-P. Hong, S. Y. Park, J. M. Suh, M.-J. Choi, S. Han, H. W. Jang, *ACS Sens.* **2019**, 4, 2395-2402.

[22] K. C. Kwon, J. M. Suh, T. H. Lee, K. S. Choi, K. T. Hong, Y. G. Song, Y.-S. Shim, M. Shokouhimehr, C.-Y. Kang, S. Y. Kim, H. W. Jang, *ACS Sens.* **2019**, 4, 678-686.

[23] W. Zhang, Z. Huang, W. Zhang, Y. Li, *Nano Research* **2014**, 7, 1731-1737.

[24] R. Kumar, P. K. Kulriya, M. Mishra, F. Singh, G. Gupta, M. Kumar, *Nanotechnology* **2018**, 29, 464001.

[25] S.-Y. Cho, S. J. Kim, Y. Lee, J.-S. Kim, W.-B. Jung, H.-W. Yoo, J. Kim, H.-T. Jung, *ACS Nano* **2015**, 9, 9314-9321.

[26] J. M. Suh, H. W. Jang, *J. Sens. Sci. Technol.* **2017**, 26, 228-234.

[27] J. Li, Y. Lu, Q. Ye, M. Cinke, J. Han, M. Meyyappan, *Nano Lett.* **2003**, 3, 929-933.

[28] N. El-Hougeiri, M. El Fadel, *Indoor Built Environ.* **2004**, 13, 421-431.

[29] K. Y. Ko, J.-G. Song, Y. Kim, T. Choi, S. Shin, C. W. Lee, K. Lee, J. Koo, H. Lee, J. Kim, T. Lee, J. Park, H. Kim, *ACS Nano* **2016**, *10*, 9287-9296.

[30] J.-H. Cha, S.-J. Choi, S. Yu, I.-D. Kim, *J. Mater. Chem. A* **2017**, *5*, 8725-8732.

[31] C. Ouyang, Y. Chen, Z. Qin, D. Zeng, J. Zhang, H. Wang, C. Xie, *Appl. Surf. Sci.* **2018**, *455*, 45-52.

[32] T. Xu, Y. Liu, Y. Pei, Y. Chen, Z. Jiang, Z. Shi, J. Xu, D. Wu, Y. Tian, X. Li, *Sens. Actuat. B−Chem.* **2018**, *259*, 789-796.

[33] W.-T. Koo, J.-H. Cha, J.-W. Jung, S.-J. Choi, J.-S. Jang, D.-H. Kim, I.-D. Kim, *Adv. Func. Mater.* **2018**, *28*, 1802575.

[34] J.-H. Kim, A. Mirzaei, H. W. Kim, S. S. Kim, *Sens. Actuat. B−Chem.* **2019**, *296*, 126659.

[35] Y. Jeong, J. Shin, Y. Hong, M. Wu, S. Hong, K. C. Kwon, S. Choi, T. Lee, H. W. Jang, J.-H. Lee, *Solid State Electron.* **2019**, *153*, 27-32.

[36] D.-H. Youn, B.-J. Kim, S. J. Yun, *Nanotechnology.* **2020**, *31*, 105602.

[37] D. Liu, Z. Tang, Z. Zhang, *Sens. Actuat. B−Chem.* **2020**, *303*, 127114.

[38] M. Ikram, L. Liu, Y. Liu, L. Ma, H. Lv, M. Ullah, L. He, H. Wu, R. Wang, K. Shi, *J. Mater. Chem. A* **2019**, 7, 14602-14612.

[39] Y. Han, Y. Liu, C. Su, S. Wang, H. Li, M. Zeng, N. Hu, Y. Su, Z. Zhou, H. Wei, Z. Yang, *Sens. Actuat. B−Chem.* **2019**, 296, 126666.

[40] N. Yamazoe, G. Sakai, K. Shimanoe, *Catal. Surv. Asia* **2003**, 7, 63-75.

[41] R. Kumar, N. Goel, M. Kumar, *Appl. Phys. Lett.* **2018**, 112, 053502.

[42] N. Barsan, U. Weimar, *J. Electroceram.* **2001**, 7, 143-167.

[43] B. Liu, Y. Luo, K. Li, H. Wang, L. Gao, G. Duan, *Adv. Mater. Interf.* **2019**, 6, 1900376.

4.2. Tin disulfide on 1D silicon dioxide

4.2.1. Introduction

With technology development in data acquisition and processing, there have been increasing demands on high-performance sensors for data collection. Especially, sensors for detecting gaseous substances have been one of the most intensively studied fields since the data they can provide directly benefit human health and life. For example, indoor air quality data prevent people from exposure to toxic gases like volatile organic compounds, which are usually emitted in very low concentration but continuous exposure can lead to severe damage in the human body.[1] In addition, the examination of the exhaled breath from people can provide helpful information for the diagnosis of potential diseases.[2] In order to collect the gaseous data from various sources in real-time and process into useful information through a network under the Internet of Everything (IoE) platform, the gas sensors should be small-sized for portability and consume very low power due to limited battery capacity.[3] To date, various types of gas sensors have been reported including electrochemical sensors, optical sensors, surface acoustic wave sensors, mass sensitive sensors, and chemoresistive sensors.[4] Compared to other types of gas sensors, chemoresistive gas sensors are developed in a very simple structure and are relatively cheap from an economic point of view, having potential in future commercialization. The chemoresistive gas sensors detect sensor signals from changes in electric current that continuously flows along with the sensing materials, and the most widely adopted sensing materials have been the metal oxide semiconductors like SnO_2, or WO_3 due to their abundant surface defects.[5–7] However, they require a very high operating

temperature over 300 °C for activation of the surface defects and meaningful sensor signals followed by inevitable high power consumption. As an alternative, two dimensional (2D) materials including graphene, transition metal dichalcogenides (TMDs), or metal nanosheets, have been attracting a great amount of attention for their high surface-to-volume ratio with high surface energy, which is beneficial for room-temperature operation.[8–10] Among various 2D materials, tin disulfide (SnS_2) has been intensively studied for gas sensor application due to its earth-abundant, nontoxic, and heavy-metal-free characteristics with layered 2D structure just like TMDs such as MoS_2, WS_2, or VS_2, as well as superior mechanical properties and remarkable electronic properties.[11] Ou *et al.* reported NO_2 gas sensors based on SnS_2 with high selectivity and reversibility.[12] According to them, SnS_2 has larger electronegativity compared to MoS_2, leading to potentially increased active sites for gas adsorption. Their SnS_2 nanoflakes prepared by solution methods exhibited the response of 27.2 to 10 ppm of NO_2 but still required an external heater for the operating temperature of 80 °C. Xu *et al.* reported SnO_2−SnS_2 hybrids for NH_3 gas sensors operating at room temperature.[13] Partially oxidized SnS_2 with the utilization of heterojunctions between SnS_2 and SnO_2 was effective in room temperature operation but exhibited a relatively low response of 1.16 to 10 ppm of NH_3. In order to achieve gas sensors based on SnS_2 operating at room temperature with high-performance, further efforts are required.

Herein, we report highly sensitive NO_2 sensors operating at room temperature with excellent recovery using SnS_2 nanograins synthesized on porous SiO_2 nanorods (NRs). This strategy was adopted from our recent study applied to MoS_2.[14] We

deposited 500 nm of SiO_2 NRs by glancing angle deposition (GLAD) method using an e-beam evaporator. The precursor solution for SnS_2 was spin-coated on the SiO_2 NRs and a sulfurization process using a chemical vapor deposition (CVD) system was conducted to synthesize SnS_2. Uniformly distributed SnS_2 on SiO_2 NRs exhibited the gas response of 701% to 10 ppm of NO_2 at room temperature with a theoretical detection limit of 408.9 ppb. These promising gas sensing properties with excellent recovery at room temperature can provide a new perspective toward the real application of SnS_2 based gas sensors to IoE.

4.2.2. Experimental procedures

Fabrication of SiO_2 NRs. Interdigitated electrodes (IDEs) with 5 μm spacing were fabricated by depositing Pt/Ti (100 nm/ 30 nm thick) on SiO_2/Si substrate using photolithography and e-beam evaporation. The fabricated electrodes were sonicated in acetone, isopropanol and distilled water in sequence. Then the electrodes were concealed with scotch tape except the active area with IDEs for a selective deposition on the active area. SiO_2 grains (Kojundo Chemistry) were used for the deposition of SiO_2 NRs. In order to fabricate SiO_2 NRs, evaporation was conducted at a glancing angle of 80° with substrate rotation speed of 80 rpm. The substrate was located 50 cm above the crucible with SiO_2 grains. The base pressure was maintained at 1×10^6 Torr and growth rate was 2.0 Å/s.

Synthesis of SnS_2 nanograins on SiO_2 NRs. The precursor solution was prepared by dissolving tin (IV) chloride pentahydrate ($SnCl_4 \cdot 5H_2O$, Sigma-Aldrich, 98%) in ethylene glycol at a concentration of 1 M. The precursor solution was spin-coated on prepared IDEs and SiO_2/Si substrates at 3500 rpm for 60 s. Hydrogen (H_2) and nitrogen (N_2) gases with high purity were used for the thermolysis process in a thermal CVD system with dual furnaces. Firstly, the temperature of CVD furnace (Heater #2 in Figure 1) for precursor-coated sample was increased to 500 °C under the flow of H_2 and N_2 at 1 Torr during 20 min. The flow rate of H_2 and N_2 was set at 100 and 500 sccm, respectively, by using mass flow controllers. After 20 min, the CVD furnace (Heater #1 in Figure 1) with temperature of 300 °C for S powder was moved through sliding rail to the set position to evaporate the S powder for the sulfurization process. The sulfurization process was started slowly under constant

flow of H_2 and N_2 gas and maintained for 30 min. After 30 min, both furnaces were cooled down to room temperature with rate of 20 °C/min.

Characterization. The morphologies of the fabricated the bare SiO_2 NRs and the SnS_2 nanograins on SiO_2 NRs were characterized by a field-emission scanning electron microscopy (FESEM, SU-70) using an acceleration voltage of 5 kV and a working distance of 8 mm. Bright field and high-resolution images were obtained with a field-emission transmission electron microscopy (FETEM, JEM-2100F) in order to investigate the morphology and structure of the bare SiO_2 NRs and the SnS_2 nanograins on SiO_2 NRs. The chemical mapping of the SnS_2 nanograins on SiO_2 NRs was also obtained by energy dispersive X-ray spectroscopy (EDS). The X-ray photoemission spectroscopy (XPS) was carried out using AXIS Ultra DLD instrument (Kratos, U.K.) in an advanced in-situ surface analysis system (AISAS; KBSI, Korea) operating at a base pressure of 1.6×10^{-10} mbar at 300 K with a monochromatic Al Kα line at 1486.69 eV to discover the chemical composition of synthesized SnS_2 nanograins on SiO_2 NRs.

Gas sensing measurement. Gas sensing measurement was performed in a quartz tube with external heater for consistent room temperature of 25 °C. The dry air and target gases (balanced with dry air, Sinjin Gases) were injected in repeating sequences through automated program. A constant flow of 1000 sccm was used for both dry air and target gases. The concentration of all gases used in this study was fixed at 500 ppm except NO_2 which was 10 ppm and H_2 which was 10000 ppm. The change in electric current by gas sensors was precisely measured by a sourcemeter (Keithley 2400) under DC bias voltage of 1 V.

4.2.3. Results and discussion

The GLAD method using an e-beam evaporator was utilized to deposit SiO_2 NRs on Pt-interdigitated electrodes (IDEs) with different thicknesses (125, 250, and 500 nm) for gas sensor applications. By changing deposition angle and time, the diameters, lengths, and degree of porosity of SiO_2 NRs can be controlled. The deposition angle of 80° and thicknesses of 125, 250, and 500 nm were chosen based on our previous studies and the detailed procedures for GLAD method can also be found in our previous studies.[15,16] After deposition of SiO_2 NRs, 1 M tin (IV) chloride pentahydrate ($SnCl_4 \cdot 5H_2O$) precursor solution which is dissolved in ethylene glycol was spin-coated on the SiO_2 NRs and sulfurization process using CVD system was conducted to synthesize the SnS_2 nanograins on porous SiO_2 NRs (Figure 4.9). The sulfur (S) powder and precursor coated-SiO_2 NRs were placed inside the quartz tube with individual heater for each of them. The evaporated S powder reacted with spin-coated $SnCl_4 \cdot 5H_2O$ precursor solution on SiO_2 NRs with the following chemical equation:

$$SnCl_4 + S\ (excess) + 2H_2 \rightarrow SnS_2 + HCl + H_2S \qquad (1)$$

The H_2 gas was used as a dilute gas to get rid of chlorine radicals and the N_2 gas was used as a carrier gas.[17] Figure 4.10a-c show cross-sectional scanning transmission electron microscopy (STEM) images of SnS_2 nanograins on SiO_2 NRs in 125, 250, and 500 nm thicknesses, respectively. The synthesized SnS_2 nanograins can be clearly seen through the rough surface of the SiO_2 NRs for all thicknesses.

From SEM images in Figure 4.11, the SnS_2 nanograins were distributed not on the individual SiO_2 NR but on a group of SiO_2 NRs. The decrease in the concentration of $SnCl_4 \cdot 5H_2O$ precursor solution from 1 M can help SnS_2 distribution on individual SiO_2 NR but the electrical resistance increases at the same time. The resistance increases with decreasing concentration of precursor solution due to a limited amount of SnS_2 at the conduction path of inter-spacing between SiO_2 NRs. The balance between the grouping of SnS_2 nanograins on SiO_2 NRs and electrical conductivity were met at the concentration of 1 M solution. EDS analysis was conducted on SnS_2 nanograins on SiO_2 NRs with 500 nm thickness and EDS mappings of Si, O, Sn, and S are shown in Figure 4.10d-g. The uniformly distributed Sn and S components on SiO_2 NRs were clearly identified. EDS mappings for SnS_2 nanograins on SiO_2 NRs with 125 and 250 nm thickness are also presented in Figure 4.12. High-resolution transmission electron microscopy (HRTEM) image and corresponding selected area diffraction (SAED) image are shown in Figure 4.13. Nano-sized grains of SnS_2 can be found on the surface of SiO_2 NRs through the HRTEM image. The SnS_2 nanograins on the surface of the SiO_2 NRs had a fringe interval of 0.32 nm for *d*-spacing of (100) and 0.20 nm for a *d*-spacing of (003). The magnified HRTEM and SAED pattern images in Figure 4.10h and i clearly show *d*-spacing of 0.32 nm for SnS_2.

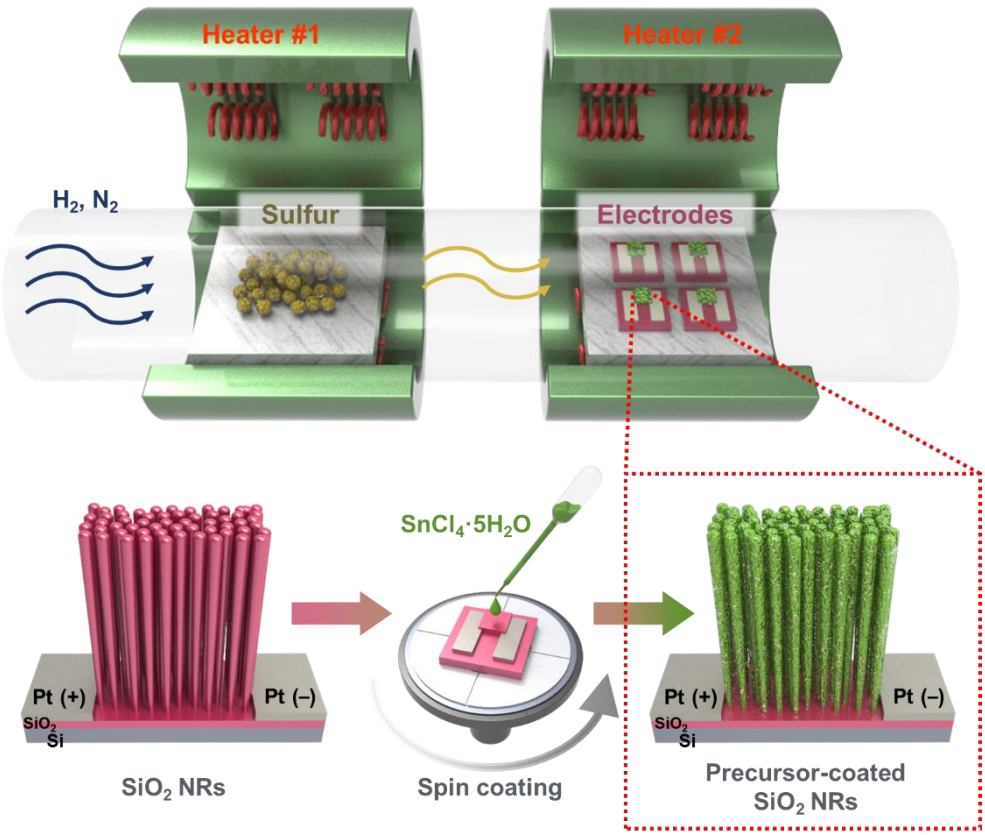

Figure 4.9. Schematic images of fabrication procedure for SnS_2 nanograins on SiO_2 NRs.

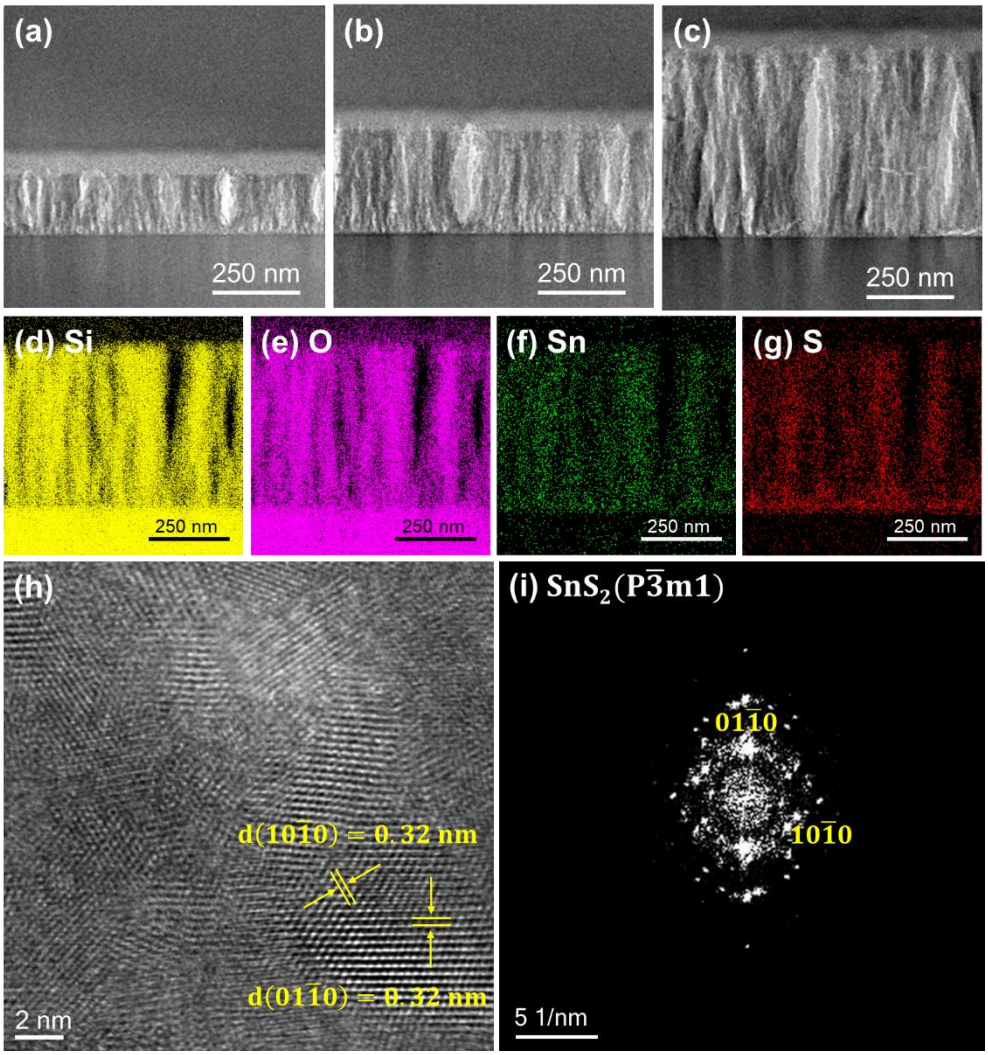

Figure 4.10. STEM images of SnS_2 nanograins on SiO_2 NRs with various thicknesses of SiO_2 NRs: (a) 125 nm, (b) 250 nm, and (c) 500 nm. (d-g) EDS mapping of (d) Si, (e) O, (f) Sn, and (g) S, (h) HRTEM, and (i) SAED pattern images of SnS_2 nanograins on SiO_2 NRs with 500 nm thickness.

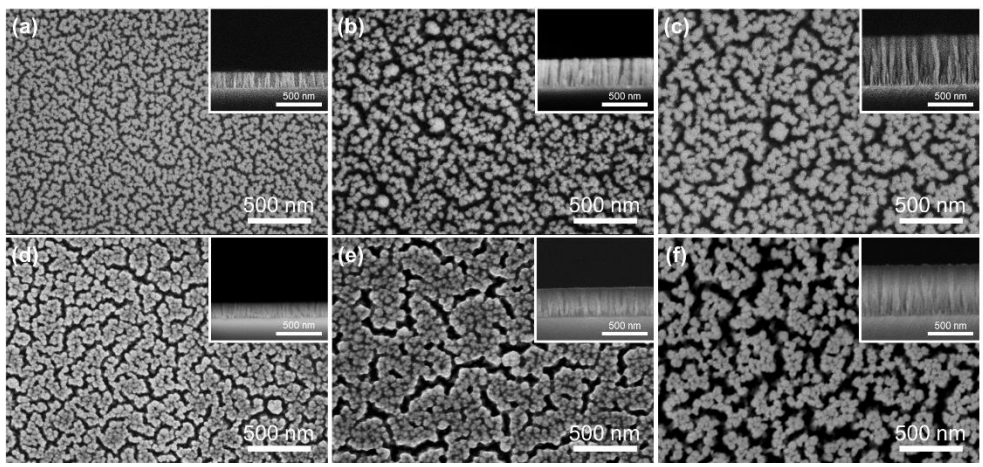

Figure 4.11. SEM images for (a-c) bare SiO_2 NRs and (d-f) SnS_2 nanograins on SiO_2 NRs with different thicknesses: (a, d) 125, (b, e) 250, and (c, f) 500 nm.

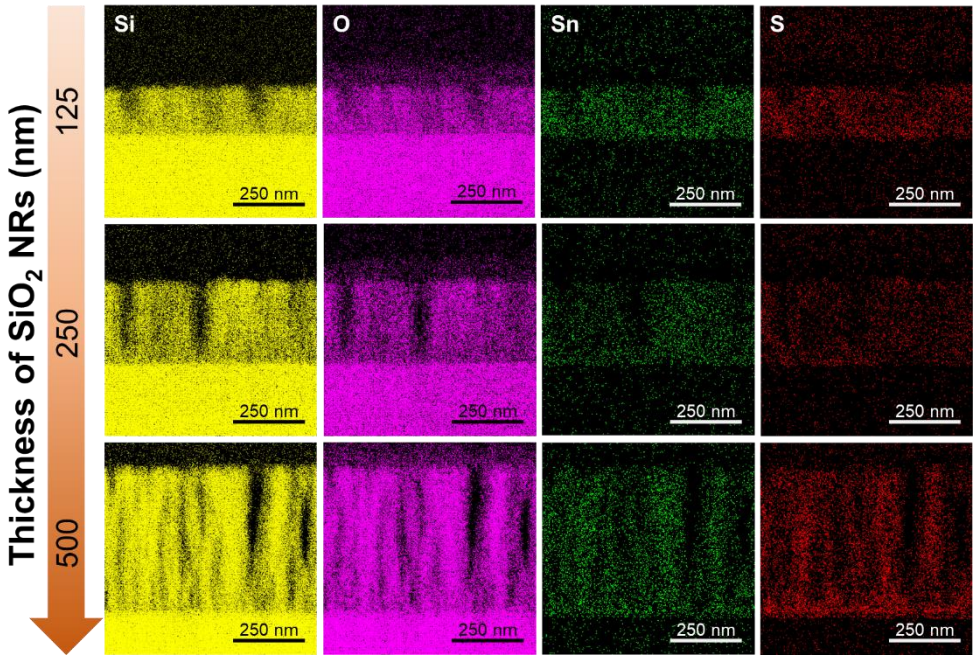

Figure 4.12. EDS mapping for SnS_2 nanograins on SiO_2 NRs with various thicknesses (125, 250, and 500 nm).

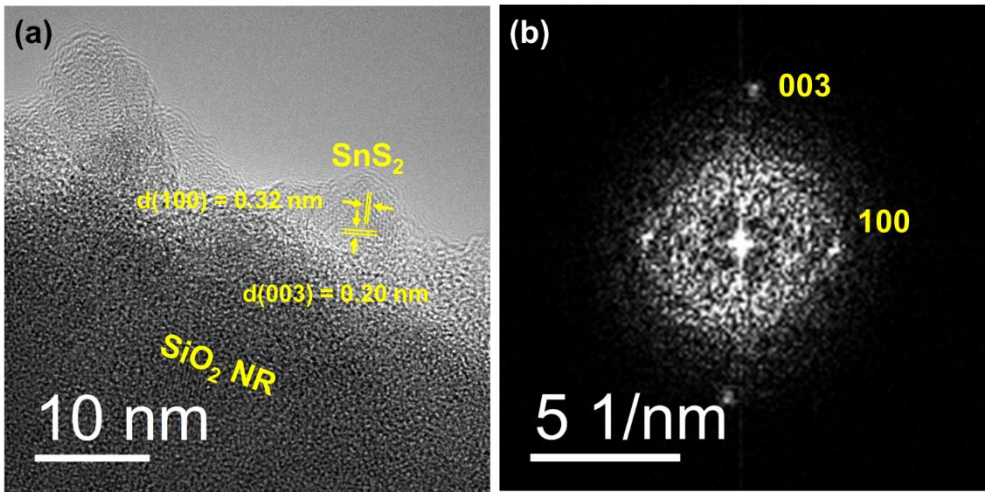

Figure 4.13. (a) HRTEM and (b) SAED pattern images of SnS_2 nanograins on SiO_2 NRs with 500 nm thickness.

AFM and XPS analyses were done to further characterize synthesized SnS_2 (Figure 4.14). In Figure 4.15a and b, the atomic force microscopy (AFM) images of SnS_2 on flat SiO_2 substrates were obtained to examine thickness and rms roughness of the synthesized SnS_2, and they were 17 nm and 0.688 nm, respectively. The XPS analysis was conducted to investigate the chemical composition of the synthesized SnS_2. Sn 3*d* and S 2*p* core-level spectra of SnS_2 synthesized on flat SiO_2 and SiO_2 NRs with different thicknesses are shown in Figure 4.15c and d, respectively. The peaks for Sn $3d_{3/2}$ and Sn $3d_{5/2}$ were observed at approximately 495.8 and 487.5 eV, respectively. Those for S $2p_{3/2}$ and S $2p_{1/2}$ were located at approximately 165.3 and 164.0 eV, respectively. A little peak shift of Sn 3*d* peaks, as shown in Figure 4.15c, originated from the structural factor in the SnS_2 synthesized onto SiO_2 NRs compared with that on flat SiO_2 substrates. From peak intensity and atomic sensitivity factors, atomic composition ratio was calculated for Sn and S. As shown in Figure 4.16, the ratio between Sn and S was consistent for all substrates with a ratio of approximately 30 to 70, which can be reduced to 1:2.33 (Sn:S). Although HRTEM and SAED pattern data supported well-synthesized SnS_2, actual atomic ratio between Sn and S was a little bit higher than 1:2.

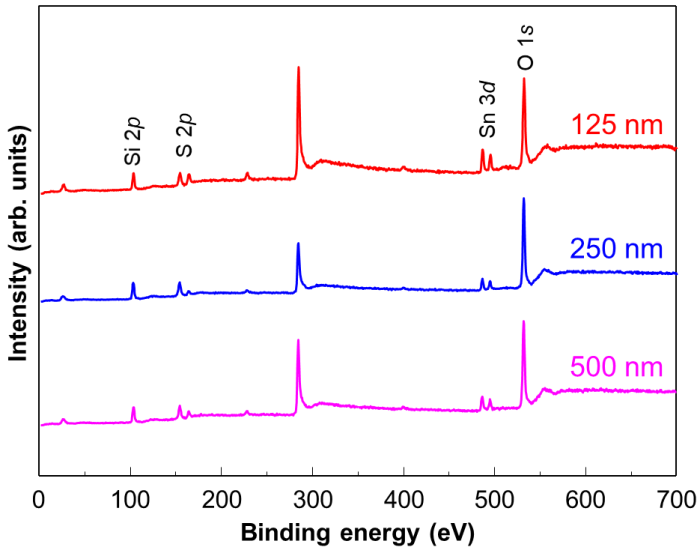

Figure 4.14. Wide scan XPS spectra for SnS_2 nanograins on SiO_2 NRs with 125, 250, and 500 nm thicknesses.

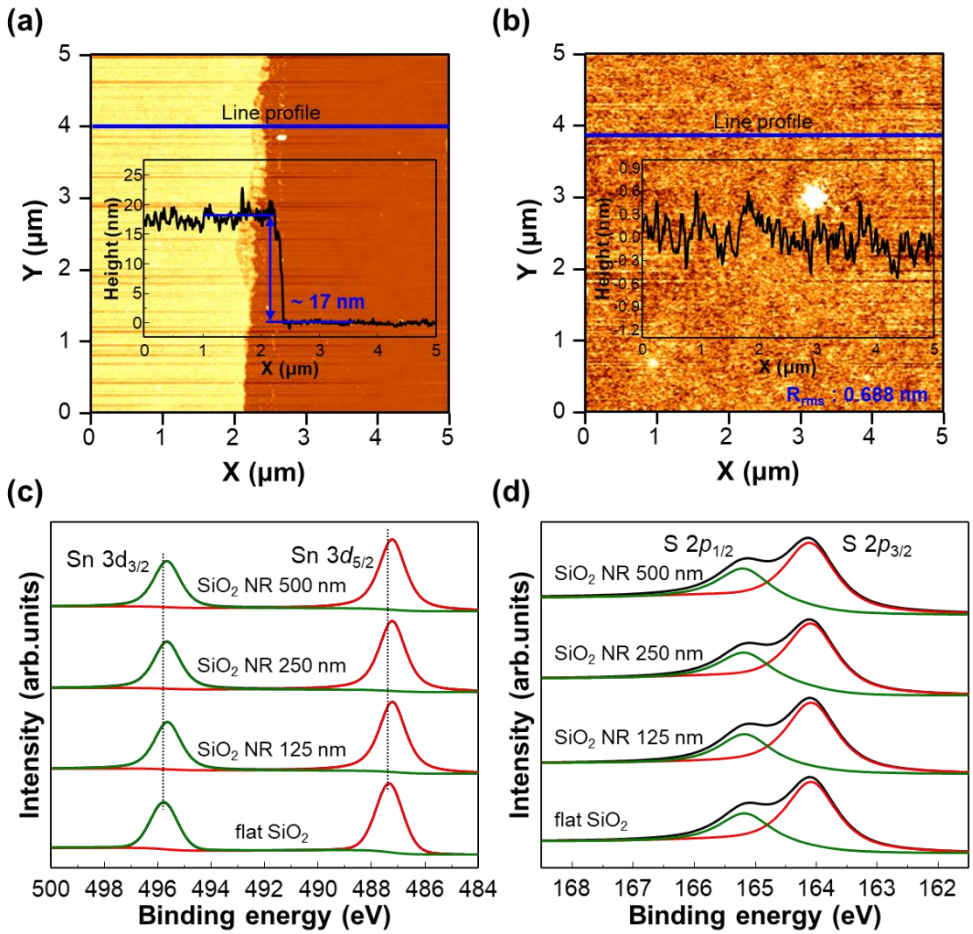

Figure 4.15. (a) Thickness and (b) rms roughness measurement through AFM analysis of synthesized SnS_2 thin film on the flat SiO_2 substrate. The XPS core level spectra of (c) Sn 3*d* and (d) S 2*p*.

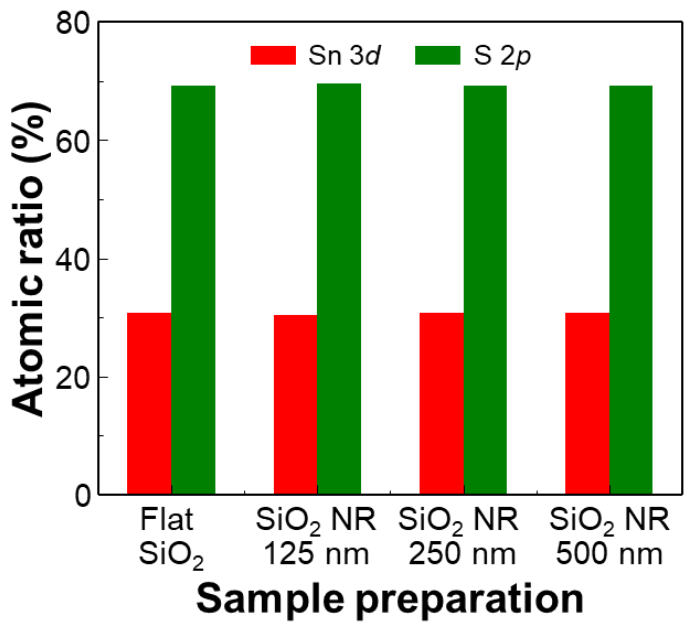

Figure 4.16. The atomic ratio of synthesized SnS_2 on each different substrate.

This sulfur-rich (S-rich) nature of SnS_2 can be attributed to nano-sized grains of SnS_2 with numerous exposed S-termination, which will be discussed later with their effects on gas sensing properties. The SnS_2 nanograins on SiO_2 NRs with different thicknesses were exposed to 10 ppm NO_2 at room temperature to investigate their gas sensing properties. The constant voltage of 1 V was applied to the SnS_2 nanograins on SiO_2 NRs under repeated pulses of synthetic air and NO_2 gas. The gas response was calculated by the ratio between the resistance change upon exposure to target gas molecules and the resistance under target gas, or $(R_{air} - R_{gas}) / (R_{gas}) \times 100$, where R_{air} and R_{gas} stand for the resistance under ambient air and target gas, respectively. As shown in Figure 4.17a, the gas response to 10 ppm NO_2 increased for the SnS_2 distributed on thicker SiO_2 NRs, and SnS_2 on SiO_2 NRs with 500 nm thickness exhibited the highest gas response of 701%. To the best of the author's knowledge, there has been no report on such a high gas response at room temperature using SnS_2 without any additives or heterojunctions according to previous reports (Table 4.2).[12,13,18-25] In addition, SnS_2 nanograins on SiO_2 NRs exhibited excellent recovery after exposure to target gas molecules. The response time and recovery time were calculated to be 272.8 s and 3800.4 s, respectively, which are relatively slow in practical aspects but still promising considering operation at room temperature. The inset in Figure 4.17b shows the baseline resistance increment upon an increase in the thickness of SiO_2 NRs. Since the thicker SiO_2 NRs provide the larger surface area for a larger amount of SnS_2 nanograins to be synthesized on, more gas adsorption sites are present as well as the higher porosity for the better accessibility of the gas molecules. Moreover, our previous study revealed that SiO_2 NRs template

induced more edge sites of 2D materials to be exposed through smaller-sized grains, which is also realized through nano-sized SnS_2 grains in this study.[14] Therefore, more exposed edge sites of SnS_2 nanograins on SiO_2 NRs are expected to have contributed to the enhanced gas sensing properties. At the same time, increased conduction path along the longer SiO_2 NRs increased electrical resistance. Interestingly, the resistance decreased after exposure to 10 ppm NO_2 gas and increased after exposure back to ambient air, meaning *p*-type semiconducting characteristics. According to previous studies, SnS_2 is widely known as an *n*-type semiconductor.[26] For *n*-type TMDs, S vacancies are present as defects on the basal plane of TMDs and function as electron donors, indicating that the Fermi level is shifted toward the conduction band minimum (CBM).[27] On the other hand, when S atoms are rich and metal atoms are relatively deficient, the Fermi level is shifted away from the CBM, exhibiting *p*-type semiconducting properties. Therefore, the *p*-type semiconducting characteristics of SnS_2 nanograins on SiO_2 NRs synthesized in this study can be attributed to S-rich nature, which was already revealed through atomic ratio (Sn:S = 1:2.33) obtained from XPS analysis. In addition to it, Cho and Hahm *et al*. reported *n*-type MoS_2 changing to *p*-type MoS_2 after transferring from sapphire glass to SiO_2/Si substrate.[28] The dangling oxygen bonds on SiO_2/Si substrate can modulate the effective Fermi levels within the bandgap of MoS_2, leading to a change in the conduction type. Since SnS_2 used in this study was also synthesized on SiO_2 NRs, the same phenomenon can possibly have contributed to the *p*-type semiconducting nature of the SnS_2 nanograins. For the further investigation on gas sensing properties of SnS_2 nanograins on SiO_2 NRs, the

detection limit and stability upon repeated exposure to the target gas were tested. As shown in Figure 4.17c, SnS_2 nanograins on SiO_2 NRs were exposed to five consecutive pulses of NO_2 gas with 1, 2, 3, 4, and 5 ppm concentration at room temperature. The gas responses exhibited a linear relationship with the gas concentration, indicating their reliable operation over the tested concentration range (Figure 4.17d). The slope of the concentration-to-response curve was calculated to be 0.462 ppm^{-1} using a linear least-squares fit.[29] Although 1 ppm was the lowest concentration of the tested NO_2 gas, the theoretical detection limit (signal-to-noise ratio higher than 3) was calculated to be approximately 408.9 ppb.

Figure 4.17e shows a stable gas response upon seven consecutive exposures to 10 ppm NO_2 gas at room temperature, demonstrating stability of the fabricated gas sensors. The selectivity toward various gases was also tested for the SnS_2 nanograins on SiO_2 NRs (Figure 4.17f). The fabricated gas sensors were exposed to H_2 (10000 ppm), C_2H_5OH (500 ppm), CO (500 ppm), and NH_3 (500 ppm) at room temperature. Since NO_2 is widely known as one of the most reactive oxidizing gas and other gases are expected to exhibit very low response when the concentration was fixed at the same concentration to NO_2 gas (10 ppm), above gases with the concentration higher than 500 ppm were used for the examination. However, the gas responses to H_2, C_2H_5OH, CO, and NH_3 were significantly lower than the gas response to 10 ppm NO_2 even with the higher concentration indicating strongly selective behavior toward NO_2 by the SnS_2 nanograins on SiO_2 NRs. Additionally, the effects of humidity and external heat supply on gas sensing properties of the SnS_2 nanograins on SiO_2 NRs were investigated as shown in Figure 4.18 and 4.19. With exposure to

a relative humidity of 50% (RH50), the base resistance increased and the recovery characteristic was improved. Since ambient atmosphere is always composed of a certain amount of humidity, this can be promising results considering future practical application of SnS_2 nanograins on SiO_2 NRs. With external heat supply, the response time and recovery time were both improved, but the gas response decreased with increasing temperature. The baseline resistance decreased with increasing operating temperature, which is probably due to thermally activated charge carriers.

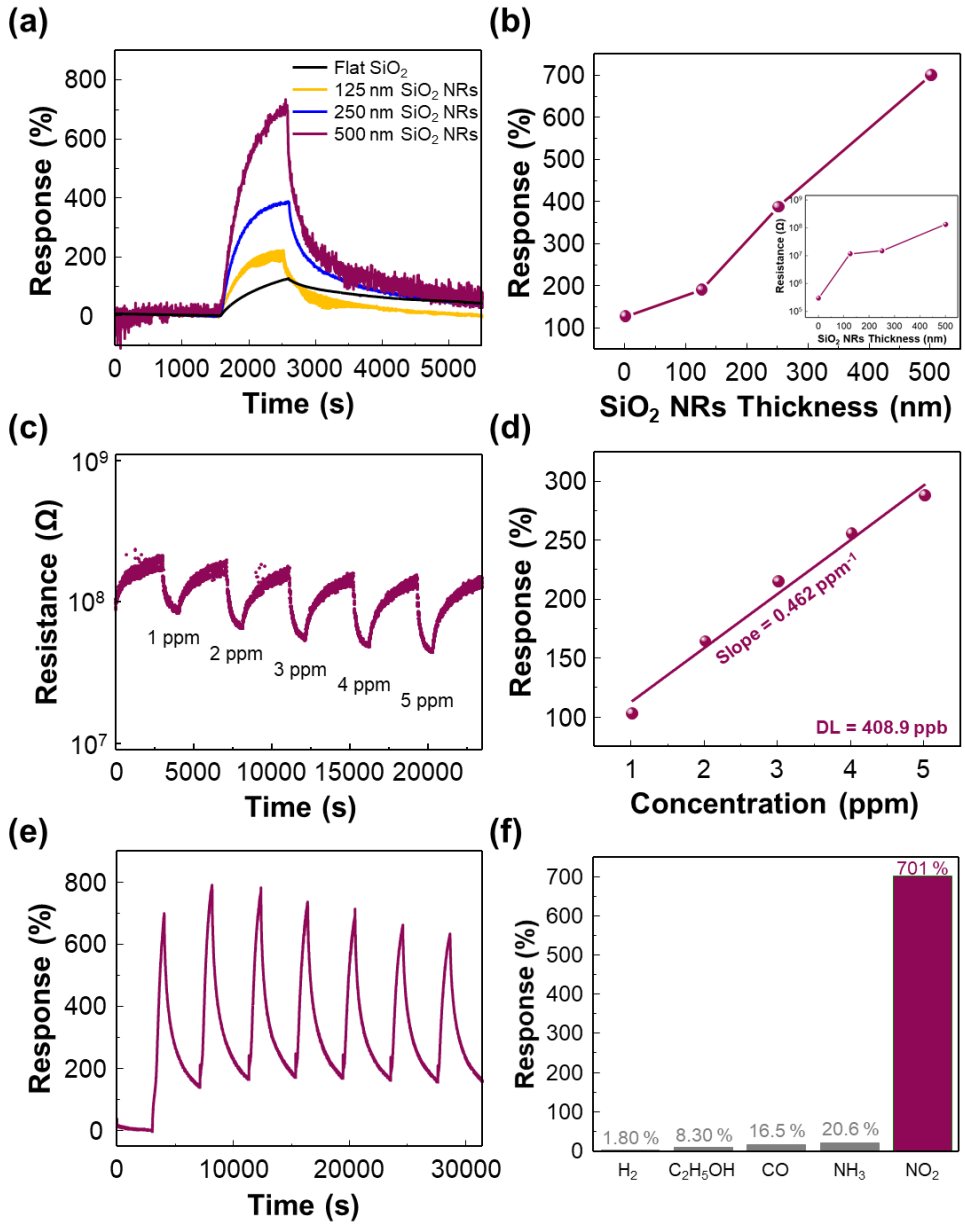

Figure 4.17. (a) Response transient of SnS_2 on each different substrate to 10 ppm of NO_2 at room temperature. (b) Responses depending on the thickness of SiO_2 NRs, and inset indic ates resistance depending on the thickness of SiO_2 NRs. (c) Response curves and (d) calibra tion of responses for SnS_2 nanograins on SiO_2 NRs toward 1−5 ppm of NO_2 at room temper ature. Responses of SnS_2 nanograins on SiO_2 NRs to (e) 7 pulses of 10 ppm of NO_2 and (f) various gases at room temperature.

Table 4.2. Comparison of NO_2 Sensing Performance of the Previously Reported Gas Sensors Based on SnS_2

Structure	Synthesis method	Temp (°C)	Balance gas	Concen. (ppm)	Response (%)	Ref.
Nanograin (SiO_2 NRs platfrom)	**Chemical vapor deposition**	**RT**	**Air**	**10**	**701**	**This work**
Nanoflake	Wet chemical	120	Air	10	3533	[12]
Nanoparticle	Precipitation	300	Air	1	~78	[21]
Nanoflake	Wet chemical	150	Air	1	60	[22]
Nanosheet	Purchased	80	Air	8	~65.3	[18]
Nanopowder	High-energy ball milling	250	N_2	10	1190.1	[23]
Nanosheet	Hydrothermal method	RT	Air	10	~30	[24]
Nanoflower	Hydrothermal method	120	Air	0.5	2440	[25]

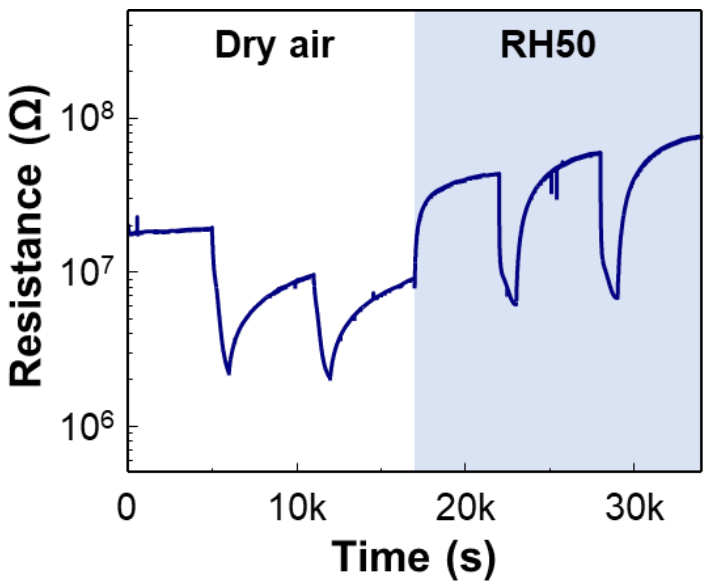

Figure 4.18. Time-transient gas response curves to 5 ppm NO_2 at room temperature under dry air and 50% relative humidity (RH50).

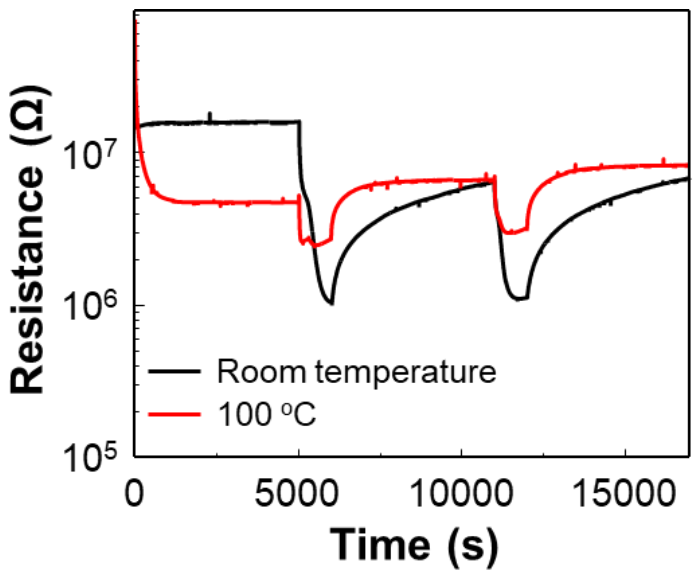

Figure 4.19. Time-transient gas response curves to 10 ppm NO_2 at room temperature and 100 °C.

The promising gas sensing properties of the SnS_2 nanograins on SiO_2 NRs can be attributed to three different factors: i) nanograins of SnS_2 with numerous S-termination ii) O_2-repulsive surface characteristics of SnS_2, and iii) 1D vertically aligned nanostructures of SnS_2 nanograins on SiO_2 NRs. As previously mentioned, S-rich condition was the main reason for the *p*-type semiconducting characteristics of the synthesized SnS_2 used in this study. When SnS_2 experiences S-rich or Sn-deficient conditions, the structural defects are formed according to McDonnell *et al*.[27] They studied non-uniform stoichiometry over a single MoS_2 flake, and revealed that S-rich region exhibits *p*-type semiconducting properties. In addition, a high concentration of dark defects at the S-rich region observed using scanning tunneling microscopy (STM) measurements are expected to be missing layers of MoS_2 to relieve surface strain induced by excessive S. Since the 2D nanostructures of S-sandwiched metal atoms is equivalent for all TMDs including MoS_2 and SnS_2, those defects with missing layers will also be expected to exist on the surface of S-rich SnS_2 and these phenomena can lead to the formation of nano-sized grains of SnS_2 grown on SiO_2 NRs. Moreover, as depicted in Figure 4.20a, nanograins of SnS_2 can expose either Sn-termination or S-termination. However, clean Sn-termination is energetically not favorable, and therefore, Sn atoms prefer to adsorb additional S atoms in their coordination.[30] J. V. Lauritsen *et al*. studied edge terminations of MoS_2 and concluded that S dimers or S monomers at Mo-edge are two possible energetically favorable configurations based on STM images and density functional theory (DFT) calculations.[31] These two configurations of fully coordinated six S atoms to each Mo atom can also be applied to SnS_2 since it has just the same 2D

structures as MoS_2, as previously mentioned (Figure 4.20b and c). Therefore, energetically stable SnS_2 contains either S-terminations or additional S-adsorbed Sn-terminations, leading to a little higher amount of S at the edge sites. These resulted in an overall high Sn:S (1:2.33) ratio exhibited by nano-sized grains of SnS_2 synthesized and utilized in this study. At the same time, S-termination sites can act as energetically more active sites for the chemical reactions, and maximized S-terminations of SnS_2 nanograins resulted in the high gas sensitivity toward NO_2 gas.[32] In addition, SnS_2 has been reported to have positive binding energy toward O_2 and repels O_2 molecules, indicating a different charge transfer mechanism compared to typical metal oxide semiconductors.[12] The metal oxide semiconductors adsorb O_2 components (O_2^-, O^-, or O^{2-} depending on operating temperature) on the surface and charge transfer occurs between adsorbed O_2 components and the gas molecules.[33] On the other hand, SnS_2 does not utilize O_2 components for charge transfer, but SnS_2 itself interacts with the target gas molecules. This can also be supported by the data of gas sensing curves shown in Figure 4.17a. The initial stabilization process for typical metal oxide semiconductors under a constant flow of dry air exhibits saturation of electrical resistance after a gradual increase or decrease of the resistance. However, SnS_2 exhibited no such stabilization process but consistent resistance independent of exposure to dry air, indicating no chemical interaction with O_2 molecules in dry air. Under these unique surface characteristics of SnS_2, NO_2 has the strongest adsorption energy to SnS_2 and exhibits distinct charge transfer from SnS_2 compared to other gases according to the DFT calculation and electronic density of states calculation done by J. Z. Ou *et al*.[12] Therefore, highly

sensitive and selective detection of NO_2 by SnS_2 nanograins on SiO_2 NRs could be achieved. The excellent recovery characteristics of SnS_2 nanograins on SiO_2 NRs can be attributed to *p*-type semiconducting nature of SnS_2 synthesized in this study. When NO_2 molecules are adsorbed on SnS_2, electrons are transferred from SnS_2 to NO_2 to lower the resistance through hole generation. Since S-rich SnS_2 has fewer electrons due to lacking electron donors of S-vacancies than typical SnS_2, desorption process of NO_2 is much more accelerated to supplement lacking electrons from NO_2, contributing to the excellent recovery characteristics at room temperature. Moreover, as mentioned before, the utilization of SiO_2 NRs template resulted in more exposed edge sites of SnS_2 on SiO_2 NRs. This unique configuration of SnS_2 on SiO_2 NRs is also expected to have influenced better recovery characteristics along with electron-deficient nature. Lastly, 1D vertically aligned nanostructure of nanograins on SiO_2 NRs provided an effective platform for gas molecules to get accessed to SnS_2 as illustrated in Figure 4.20d. The 1D nanostructures with high porosity provided maximized surface area for SnS_2 and chance of more gas molecules to get adsorbed to SnS_2 for extremely high gas responses toward NO_2 gas.

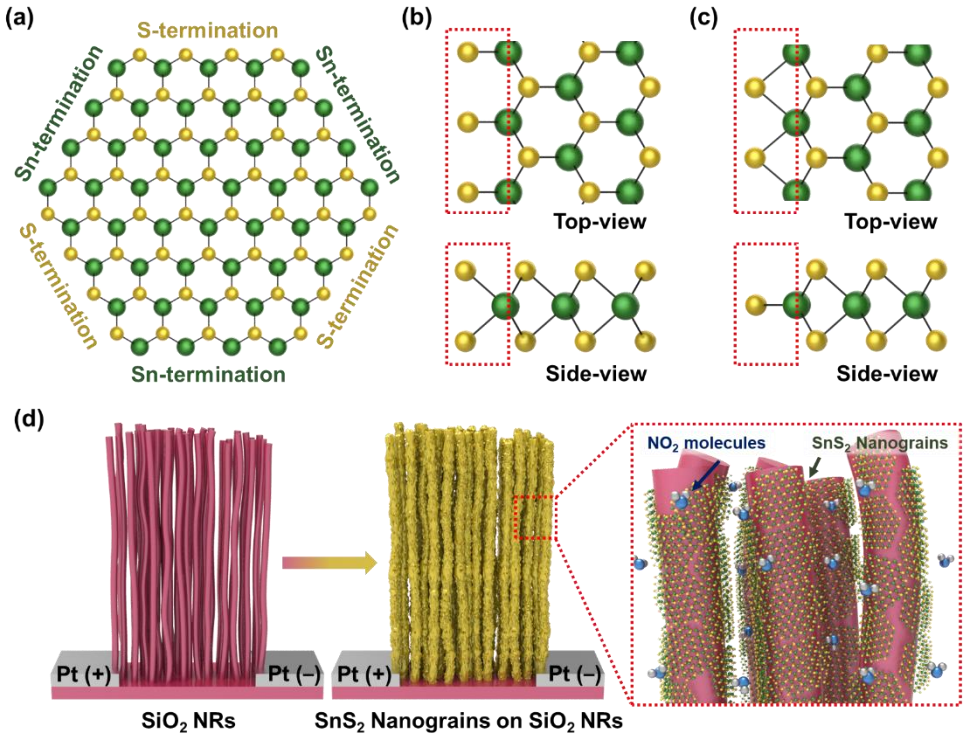

Figure 4.20. (a) Ball model of a hypothetical bulk truncated SnS_2 hexagon exposing both Sn- and S-termination. (b,c) Top-view and side-view ball models of Sn-termination with (b) S dimers and (c) S monomers per Sn-termination. (d) Schematic illustration of bare SiO_2 NRs and SnS_2 nanograins on SiO_2 NRs.

4.2.4. Conclusion

We demonstrated an effective and efficient strategy to dramatically enhance gas sensing properties of SnS_2 through nano-sized grains of SnS_2 and highly porous platform of SiO_2 NRs. The SnS_2 nanograins on SiO_2 NRs exhibited a superior gas sensing performance toward NO_2 gas with a remarkable gas response and excellent recovery characteristics with extremely high selectivity at room temperature. We attribute them to S-rich nature of SnS_2 induced by numerous S-termination of SnS_2 nanograins, unique surface characteristics of SnS_2, and 1D nanostructures of SnS_2 nanograins on SiO_2 NRs. We strongly believe that this study can provide a new perspective toward utilization of nanostructured 2D materials for gas sensor applications.

4.2.5. References

[1] J. Sundell, *Indoor Air* **2004**, 14, 51-58.

[2] B. Buszewski, M. Kęsy, T. Ligor, A. Amann, *Biomed. Chromatogr.* **2007**, 21, 553-566.

[3] A. Baranov, D. Spirjakin, S. Akbari, A. Somov, *Sens. Actuat. A−Phys.* **2015**, 233, 279-289.

[4] R. Moos, K. Sahner, M. Fleischer, U. Guth, N. Barsan, U. Weimar, *Sensors* **2009**, 9, 4323-4365.

[5] J.-M. Jeon, Y.-S. Shim, S. D. Han, D. H. Kim, Y. H. Kim, C.-Y. Kang, J.-S. Kim, M. Kim, H. W. Jang, *J. Mater. Chem. A* **2015**, 3, 17939-17945.

[6] Y.-S. Shim, D. H. Kim, H. Y. Jeong, Y. H. Kim, S. H. Nahm, C.-Y. Kang, J.-S. Kim, W. Lee, H. W. Jang, *Sens. Actuat. B−Chem.* **2015**, 213, 314-321.

[7] Y.-S. Shim, H. G. Moon, D. H. Kim, L. Zhang, S.-J. Yoon, Y. S. Yoon, C.-Y. Kang, H. W. Jang, *RSC Adv.* **2013**, 3, 10452-10459.

[8] K. Lee, R. Gatensby, N. McEvoy, T. Hallam, G. S. Duesberg, *Adv. Mater.* **2013**, 25, 6699-6702.

[9] X. Liu, T. Ma, N. Pinna, J. Zhang, *Adv. Funct. Mater.* **2017**, 27, 1702168.

[10] S. Shi, R. Hu, E. Wu, Q. Li, X. Chen, W. Guo, C. Sun, X. Hu, D. Zhang, J. Liu, *Nanotechnology* **2018**, 29, 435502.

[11] G. Radovsky, R. Popovitz-Biro, M. Staiger, K. Gartsman, C. Thomsen, T. Lorenz, G. Seifert, R. Tenne, *Angew. Chem.* **2011**, 123, 12524-12528.

[12] J. Z. Ou, W. Ge, B. Carey, T. Daeneke, A. Rotbart, W. Shan, Y. Wang, Z. Fu, A. F. Chrimes, W. Wlodarski, *ACS Nano* **2015**, 9, 10313-10323.

[13] K. Xu, N. Li, D. Zeng, S. Tian, S. Zhang, D. Hu, C. Xie, *ACS Appl. Mater. Interfaces* **2015**, 7, 11359-11368.

[14] Y.-S. Shim, K. C. Kwon, J. M. Suh, K. S. Choi, Y. G. Song, W. Sohn, S. Choi, K. Hong, J.-M. Jeon, S.-P. Hong, S. Kim, S. Y. Kim, C.-Y. Kang, H. W. Jang, *ACS Appl. Mater. Interfaces* **2018**, 37, 31594-31602.

[15] J. M. Suh, Y.-S. Shim, D. H. Kim, W. Sohn, Y. Jung, S. Y. Lee, S. Choi, Y. H. Kim, J.-M. Jeon, K. Hong, K. C. Kwon, S. Y. Park, C. Kim, J.-H. Lee, C.-Y. Kang, H. W. Jang, *Adv. Mater. Technol.*, **2017**, 2, 1600259.

[16] J. M. Suh, W. Sohn, Y.-S. Shim, J.-S. Choi, Y. G. Song, T. L. Kim, J.-M. Jeon, K. C. Kwon, K. S. Choi, C.-Y. Kang, H.-G. Byun, H. W. Jang, *ACS Appl. Mater. Interfaces* **2017**, 10, 1050-1058.

[17] A. Ortiz, J. C. Alonso, M. Garcia, J. Toriz, *Semicond. Sci. Technol.* **1996**, 11, 243.

[18] D. Gu, X. Li, Y. Zhao, J. Wang, *Sens. Actuat. B−Chem.* **2017**, 244, 67-76.

[19] R. Li, K. Jiang, S. Chen, Z. Lou, T. Huang, D. Chen, G. Shen, *RSC Adv.* **2017**, 7, 52503-52509.

[20] J. Hao, D. Zhang, Q. Sun, S. Zheng, J. Sun, Y. Wang, *Nanoscale* **2018**, 10, 7210-7217.

[21] A. Gaiardo, B. Fabbri, V. Guidi, P. Bellutti, A. Giberti, S. Gherardi, L. Vanzetti, C. Malagù, G. Zonta, *Sensors* **2016**, 16, 296.

[22] Y. Li, S. G. Leonardi, A. Bonavita, G. Neri, W. Wlodarski, *Procedia Engineering* **2016**, 168, 1102-1105.

[23] Y.-H. Kim, D.-T. Phan, S. Ahn, K.-H. Nam, C.-M. Park, K.-J. Jeon, *Sens. Actuat. B−Chem.* **2018**, 255, 616-621.

[24] Z. Qin, K. Xu, H. Yue, H. Wang, J. Zhang, C. Ouyang, C. Xie, D. Zeng, *Sens. Actuat. B−Chem.* **2018**, 262, 771-779.

[25] D. Liu, Z. Tang, Z. Zhang, *Sens. Actuat. B−Chem.* **2018**, 273, 473-479.

[26] Y. Kumagai, L. A. Burton, A. Walsh, F. Oba, *Phys. Rev. Appl.* **2016**, 6, 014009.

[27] S. McDonnell, R. Addou, C. Buie, R. M. Wallace, C. L. Hinkle, *ACS Nano* **2014**, 8, 2880-2888.

[28] B. Cho, M. G. Hahm, M. Choi, J. Yoon, A. R. Kim, Y.-J. Lee, S.-G. Park, J.-D. Kwon, C. S. Kim, M. Song, Y. Jeong, K.-S. Nam, S. Lee, T. J. Yoo, C. G. Kang, B. H. Lee, H. C. Ko, P. M. Ajayan, D.-H. Kim, *Sci. Rep.* **2015**, 5, 8052.

[29] J. Li, Y. Lu, Q. Ye, M. Cinke, J. Han, M. Meyyappan, *Nano Lett.* **2003**, 3, 929-933.

[30] M. V. Bollinger, K. W. Jacobsen, J. K. Nørskov, *Phys. Rev. B* **2003**, 67, 085410.

[31] J. V. Lauritsen, S. Helveg, E. Lægsgaard, I. Stensgaard, B. S. Clausen, H. Topsøe, F. Besenbacher, *J. Catal.* **2001**, 197, 1-5.

[32] J. Martincová, M. Otyepka, P. Lazar, *Chem. Eur. J.* **2017**, 23, 13233-13239.

[33] H.-J. Kim, J.-H. Lee, *Sens. Actuat. B−Chem.* **2014**, 192, 607-627.

4.3. Sulfurization of 1D tin dioxide

4.3.1. Introduction

The concept of healthcare has been evolving significantly with the development of technologies. In the early stage of healthcare (Healthcare 1.0), a primary goal of healthcare was to prevent epidemics which killed numerous people at a time, therefore, focusing on doctors and medical processes only. In the next stage or Healthcare 2.0, individual diseases of each person had started to be treated for more precise prescription with advanced technologies. In the current stage or Healthcare 3.0, the optimal goal has been to secure the longevity of human life utilizing numerous health-monitoring data acquired from the Internet of Everything (IoE) platform.[1] With numerous healthcare devices developed, all kinds of signals from the human body can be monitored in real-time and IoE platform can efficiently collect and process those data to yield valuable healthcare information. Among various signals from a human body, gas composition in exhaled breath can be great biomarkers for the diagnosis of potential diseases. For example, patients with asthma have nitrogen dioxide (NO_2) and those with renal disease have ammonia (NH_3) in their breath.[2] Therefore, the gas sensors for precise detection of the exhaled breath are highly demanded. To acquire gaseous information from the various environment including exhaled breath, many sensor principles have been suggested and chemoresistive gas sensors have been regarded as the best candidate due to their simplicity in operation and fabrication, low cost, small size, and feasibility of integration into existing circuits, which can secure portability of the sensors and realize real-time monitoring of the exhaled breath.[3]

The most challenging obstacle for the examination of exhaled breath is the highly humid condition of the exhaled breath which is assumed to be as high as 100% relative humidity (RH100).[4] The water molecules are well-known interfering substances during adsorption and desorption of gas molecules on gas sensing materials.[5] Under highly humid conditions, the gas sensing mechanism of chemoresistive gas sensors changes from well-known oxygen absorbates mediated chemical reaction[6] to "hopping charge transport mechanism by absorbed OH-ions" at lower humidity levels and "Grotthuss water physisorption mechanism" at higher humidity levels.[7, 8] Song, et al. reported moderate humidity level can promote gas sensing reaction to yield better performance[9] but no studies have been reported on securing gas sensing properties under a high level of humidity close to RH100 to best of author's knowledge. Although there have been some efforts on developing an ionic liquid filter for humidity effect reduction, these efforts are also limited to a certain level of humidity less than RH90~100.[10]

In the aspect of gas sensing materials, metal oxides are considered not suitable for the IoE application due to their high operating temperature over 300 ℃. As an alternative, 2-dimensional materials (2D) have been widely adopted due to their high surface energy which is advantageous for adsorption and desorption of gas molecules even at low temperatures.[11-13] Among various 2D materials, tin sulfide (SnS) and disulfide (SnS_2) has been attracting great attention for application in electronic devices due to its earth-abundant, nontoxic, and heavy-metal-free characteristics with layered 2D structure as well as superior mechanical properties and remarkable electronic properties.[14] J. Wang *et al*. reported gas sensors based on SnS thin crystals

with highly selective behavior to 1 ppm NO_2 at room temperature. However, the gas response was limited to approximately 60%.[15] One of the effective ways to enhance the gas sensing properties is to utilize unique electronic properties at the interfaces of heterojunctions.[16, 17] Y. Zheng *et al.* reported SnS_2/SnO_2 hetero-structures for excellent performance as an anode material for Li-ion and Na-ion batteries, respectively,[18] and J. J. M. Vequizo and M. Ichimura reported their application to solar cells.[19] However, no further studies have been reported on gas sensing properties of heterojunctions between SnS or SnS_2 with SnO_2 under highly humid conditions to the best of the author's knowledge.

Herein, we focused on chemoresistive type gas sensors with simple structures. The heterojunctions between SnS or SnS_2 with SnO_2 in vertically aligned 1-dimensional (1D) nanostructures were utilized for the gas sensing materials. The heterojunctions were prepared by a direct sulfurization of SnO_2 nanorods (NRs) fabricated through glancing angle deposition (GLAD) method using an e-beam evaporator. They exhibited superior gas response and recovery to 1 ppm NO_2 under RH90 with an extremely low theoretical detection limit. Furthermore, noble metal (Au, Pd, and Co) decoration on sulfurized SnO_2 NRs exhibited a diverse selectivity toward various gases. The gas sensors developed in this study will provide a new perspective of heterojunction nanostructures for the examination of exhaled breath.

4.3.2. Experimental procedures

Fabrication of SnO_2 nanorods. The glancing angle deposition (GLAD) method using e-beam evaporator was utilized to deposit SnO_2 nanorods with 500 nm thickness on Pt-interdigitated electrodes (IDEs). Pt-IDEs were prepared by depositing Pt/Ti (100/30 nm thick) on IDEs-patterned SiO_2(300 μm)/Si substrates through conventional lift-off process using photoresist (AZ 5214E, Merck). SnO_2 grains with 99% purity (Kojundo Chemistry) were used for the deposition. The base pressure of the chamber was maintained at 1×10^{-6} Torr, and the growth rate was 1.0 Å/s. This procedure is illustrated in Figure 4.21.

Sulfurization of SnO_2 nanorods. After deposition of the SnO_2 nanorods, the fabricated samples were sulfurized using chemical vapor deposition (CVD) system (Figure 4.22). The CVD system is composed of two seperate heaters and the quartz tube. The fabricated SnO_2 NRs and the sulfur powder (Merck) were placed inside the quartz tube and both heaters were placed at each position. Constant flow of N_2 and H_2 gas were maintained during whole sulfurization process. The heater placed at SnO_2 NRs (heater #2) was first heated up to 450 °C in 30 min. The heater placed at sulfur powder (heater #1) was moved to the side in order to prevent evaporation of sulfur powder at unexpected temperature. The heater #1 was heated up to 300 °C in 5 min. Then the heater #1 was slid in to evaporate sulfur powder for 5, 15, 30, and 60 min. After sulfurization, both heaters were turned off and the fabricated samples were cooled down for 35 min, resulting in sulfurized SnO_2 NRs (S-SnO_2 NRs).

Characterization. The morphologies of the fabricated pristine SnO_2 NRs (P-SnO_2 NRs) and S-SnO_2 NRs were characterized by a field-emission scanning electron

microscopy (FESEM, SU-70) using an acceleration voltage of 5 kV and a working distance of 8 mm. Bright field and high-resolution images were obtained with a field-emission transmission electron microscopy (FETEM, JEM-2100F) in order to investigate the morphology and structure of the P-SnO_2 NRs and S-SnO_2 NRs. The chemical mapping of S-SnO_2 NRs was also obtained by energy dispersive X-ray spectroscopy (EDS). X-ray diffraction (XRD, D8 Advance) was utilized to investigate crystallographic characteristic of S-SnO_2 NRs.

Gas sensing measurement. Gas sensing measurement was conducted in a quartz tube with external heat source (Lindberg/Blue™ Mini-Mite™ Tube Furnaces). The external heat source was used to maintain the quartz tube at room temperature (25°C). Through automated mass flow controlling system, gas injection was performed in repeating sequence of dry air and target gas (balanced with dry air, Sinjin Gases). For the humidity condition, controlled flow of dry air was injected into the bubbler to produce H_2O vapor. A constant flow of 1000 sccm was maintained throughout whole measurements. A concentration of all gases used in this study was fixed at 5 ppm except NO_2 which was 1 ppm. The response to target gas was precisely measured at a DC bias voltage of 0.5 V using a sourcemeter (Keithley 2400).

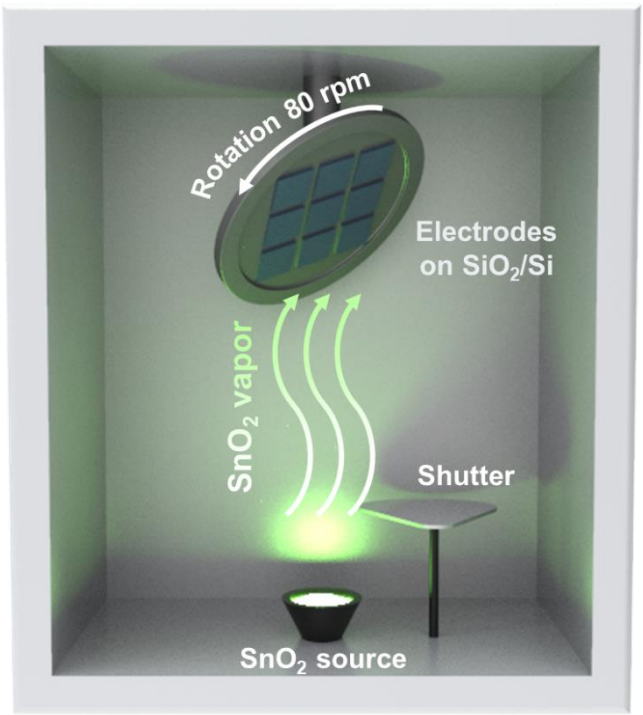

Figure 4.21. Schematic illustration of glancing angle deposition method using e-beam evaporator for deposition of SnO_2 NRs.

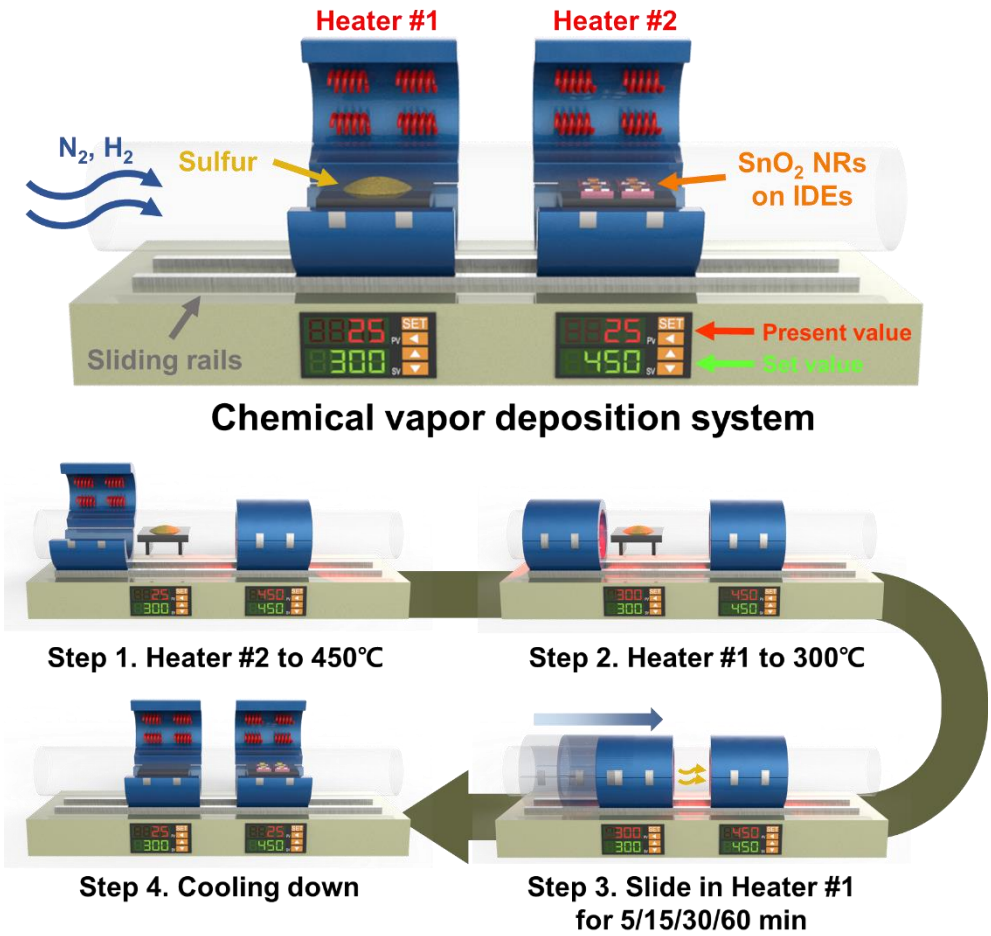

Figure 4.22. Schematic illustrations for fabrication procedures of sulfurized SnO_2 NRs.

4.3.3. Results and discussion

The glancing angle deposition (GLAD) method using an e-beam evaporator was utilized to deposit 500 nm-thick SnO_2 NRs on Pt-IDEs and SiO_2/Si substrates Change in deposition parameters including deposition angle, time, and rotation speed can modulate a diameter, length, and porosity of SnO_2 NRs. Based on our previous studies, a deposition angle of 80° and a rotation speed of 80 rpm was chosen for the deposition of 500 nm-thick SnO_2 NRs.[20, 21] After the deposition of SnO_2 NRs, they were located inside the quartz tube for the sulfurization using a CVD system with dual furnaces as illustrated in Figure 4.22. The ratio of carrier gas and sulfurization temperature were fixed at 1000:100 (N_2:H_2) and 450 °C, respectively. For further optimization of synthesis conditions for sulfurized SnO_2 (S-SnO_2) NRs, sulfurization time (5, 15, 30, and 60 min) were controlled. With the controlled parameters, the sulfurization process was conducted to fabricate S-SnO_2 NRs through a chemical reaction with sulfur vapor from sulfur powder located at heater #1. Detailed procedures are well-explained in the experimental section. Figure 4.23a and b show cross-sectional scanning transmission electron microscopy (STEM) images of the pristine SnO_2 (P-SnO_2) NRs and S-SnO_2 NRs. Vertically aligned 1D nanostructures can be clearly seen, and there is no significant change in morphology after sulfurization. Top-view and cross-sectional SEM images (Figure 4.24) also support no significant change in porosity, diameter, length, or any morphology of the SnO_2 NRs. However, high-resolution TEM (HRTEM) images and selected area diffraction (SAED) images of P-SnO_2 NRs and S-SnO_2 NRs exhibit a clear difference in the composition of the SnO_2 NRs (Figure 4.23c-e). While P-SnO_2 NRs exhibit only

tetragonal SnO_2 with a fringe interval of 0.33 nm and 0.24 nm which correspond to *d*-spacing of (110) and (200), respectively, S-SnO_2 NRs exhibit mixed composition of SnS and SnS_2 with original SnO_2. The orthorhombic SnS with fringe interval of 0.34 nm and 0.32 nm which correspond to the *d*-spacing of (120) and (021), and hexagonal SnS_2 with a fringe interval of 0.32 nm which correspond to the *d*-spacing of $(01\bar{1}0)$. EDS analysis data as shown in Figure 4.25a-d clearly show uniformly distributed sulfur-components over 500 nm-thick S-SnO_2 NRs. In order to further characterize the surface of S-SnO_2 NRs, X-ray photoelectron spectroscopy (XPS) was conducted (Figure 4.26). From the atomic composition data of Sn and S for each S-SnO_2 after different sulfurization times in Figure 4.26c, a decreasing amount of S can be clearly seen. The exposure to H_2 carrier gas during the CVD process is known for its etching effect on already synthesized TMDs.[22] Gradual decrease in S composition ratio indicates etched away S from the surface of S-SnO_2 NRs, and this eventually affects gas sensing properties of S-SnO_2 NRs which will be explained in the following description.

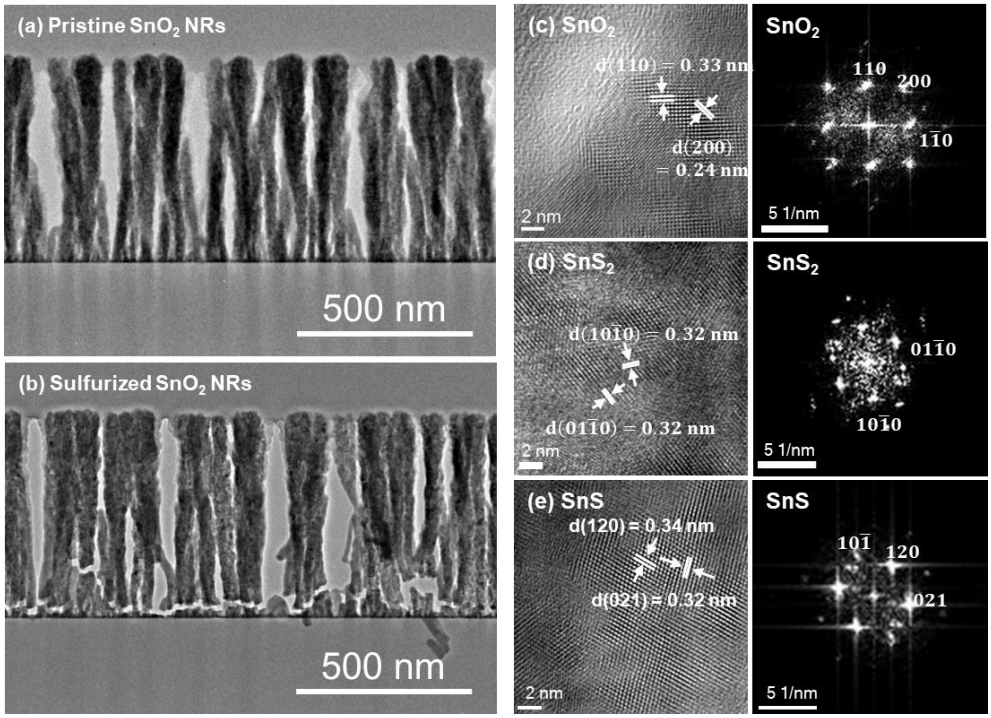

Figure 4.23. (a, b) Cross-sectional scanning transmission electron microscopy (STEM) images of (a) pristine SnO_2 (P-SnO_2) NRs and (b) sulfurized SnO_2 (S-SnO_2) NRs. (c-e) High-resolution TEM and corresponding selected area electron diffraction (SAED) patterns of (c) SnO_2, (d) SnS_2, and (e) SnS.

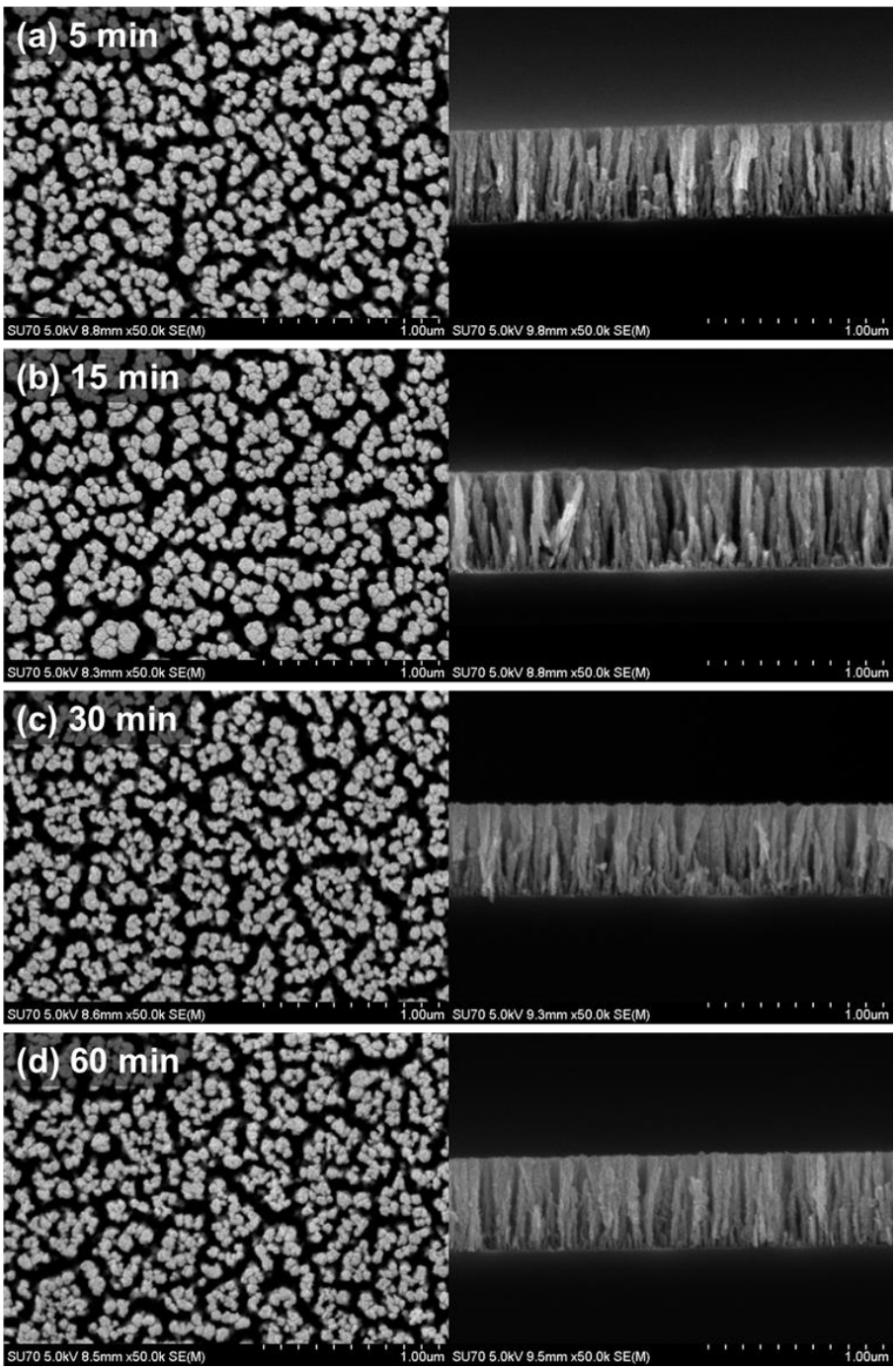

Figure 4.24. Top-view and cross-sectional view scanning electron microscopy (SEM) images of S-SnO_2 NRs after (a) 5 min, (b) 15 min, (c) 30 min, and (d) 60 min sulfurization.

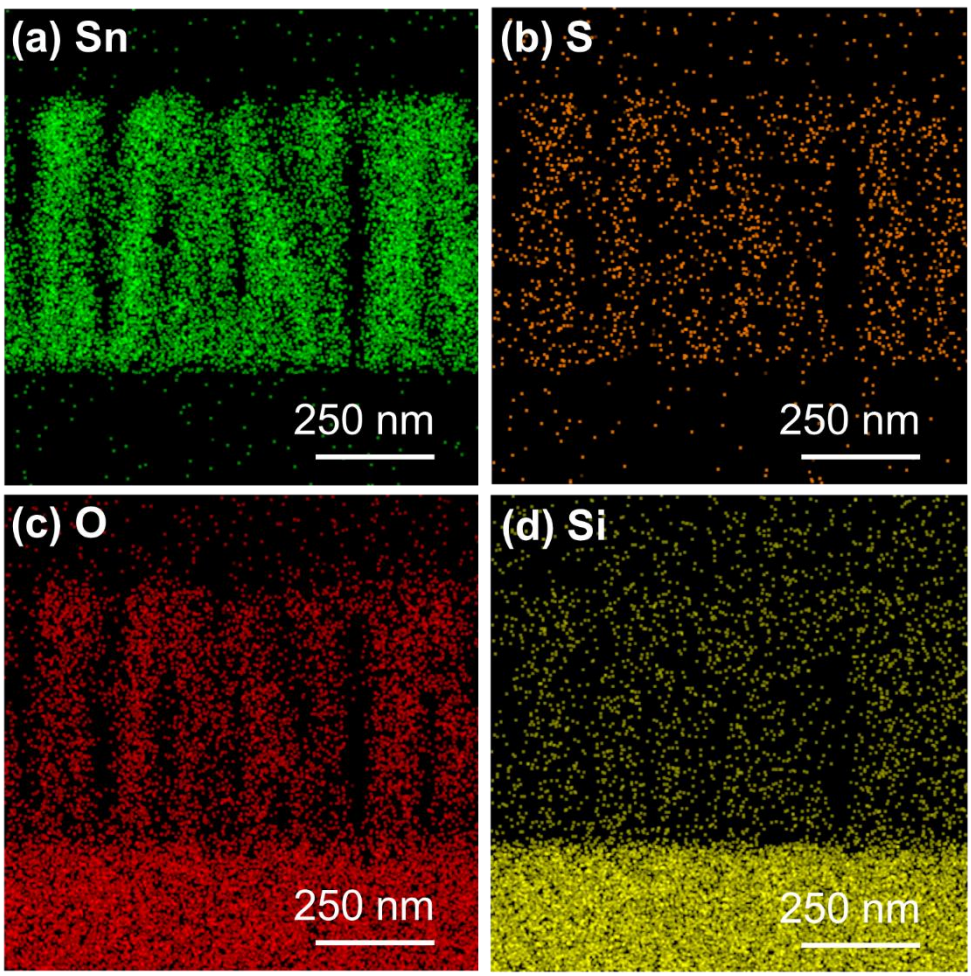

Figure 4.25. Energy-dispersive X-ray spectroscopy (EDS) mapping of (a) Sn, (b) S, (c) O, and (d) Si for S-SnO_2 NRs.

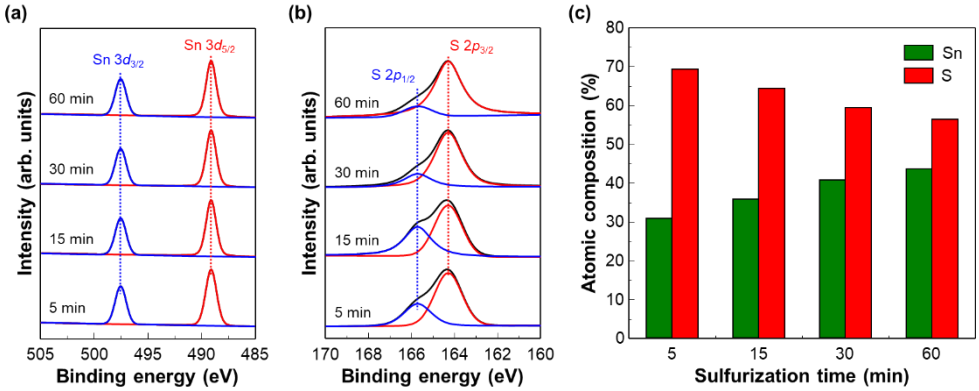

Figure 4.26. The core level X-ray photoelectron spectra (XPS) of (d) Sn 3*d* and (e) S 2*p*. (f) The atomic ratio of S-SnO_2 NRs with different sulfurization times (5, 15, 30, and 60 min).

The fabricated S-SnO_2 NRs were exposed to 1 ppm NO_2 at room temperature to investigate their gas sensing properties. The constant voltage of 0.5V was applied to S-SnO_2 NRs under repeated pulses of synthetic air with humidity and NO_2 gas. The gas sensing curves were obtained at three different atmospheres: i) dry air, ii) RH50, iii) RH90 as shown in Figure 4.27. Interestingly, a stable gas sensing operation even under RH90 was exhibited by S-SnO_2 NRs with sulfurization time of 5 and 15 min. The excessive sulfurization time over 30 min resulted in unreliable gas sensing properties and this can mainly be attributed to the etched away surface of S-SnO_2 as previously discussed. To further investigate promising gas sensing properties under RH90, the gas responses were calculated. The gas responses were calculated by the ratio between the resistance change upon exposure to target gas molecules and the resistance under target gas, or $(R_{air} - R_{gas}) / (R_{gas})$, where R_{air} and R_{gas} stand for the resistance under synthetic air with humidity and target gas, respectively. As shown in Figure 4.28a and b, S-SnO_2 NRs sulfurized for 15 min exhibited the highest gas response under RH90. Those sulfurized for 5 min still exhibited relatively high gas response and the gas response further increased for those sulfurized for 15 min. However, it suddenly decreased after 30 min and exhibited even lower gas response than P-SnO_2 NRs (58.376) (Figure 4.29). As previously mentioned, excessive H_2 concentration etched the surface of S-SnO_2 NRs for longer than 15 min. The change in resistance was exhibited accordingly (Figure 4.28c). The resistance decreased at first due to the formation of sulfides but increased from 30 min due to etching. The S-SnO_2 NRs sulfurized for 60 min are expected to have excessively been etched, resulting in the resistance level similar to P-SnO_2 NRs (1630.1 Ω).

The gas sensing properties of the S-SnO_2 NRs sulfurized under the optimal 15 min sulfurization time were further investigated to find the capability of practical application. For repeatability of the S-SnO_2 NRs, the gas sensors were exposed to ten consecutive pulses of 1 ppm NO_2 under RH90 at room temperature. As shown in Figure 4.30, S-SnO_2 NRs exhibited consistent gas responses, indicating their reliable operation over multiple exposures to target gas. The tested S-SnO_2 NRs were stored for two weeks and exposed to 1 ppm NO_2. The resulting gas sensing curves are shown in Figure 4.30b and revealed their stability upon long-term storage. The gas sensors were also exposed to 200-600 ppb NO_2 for the investigation of the detection limit (Figure 4.30c). The gas responses exhibited evident linearity with the increase in NO_2 concentration, indicating their stable operation over the tested concentration range (Figure 4.30d). The slope of the concentration-to-response curve was calculated to be 346.71 ppm^{-1} using a linear least-squares fit.[23] Even though the lowest concentration of NO_2 tested in this work was 200 ppb, the theoretical detection limit (signal-to-noise ratio higher than 3) was calculated to be approximately 1.67 ppt.

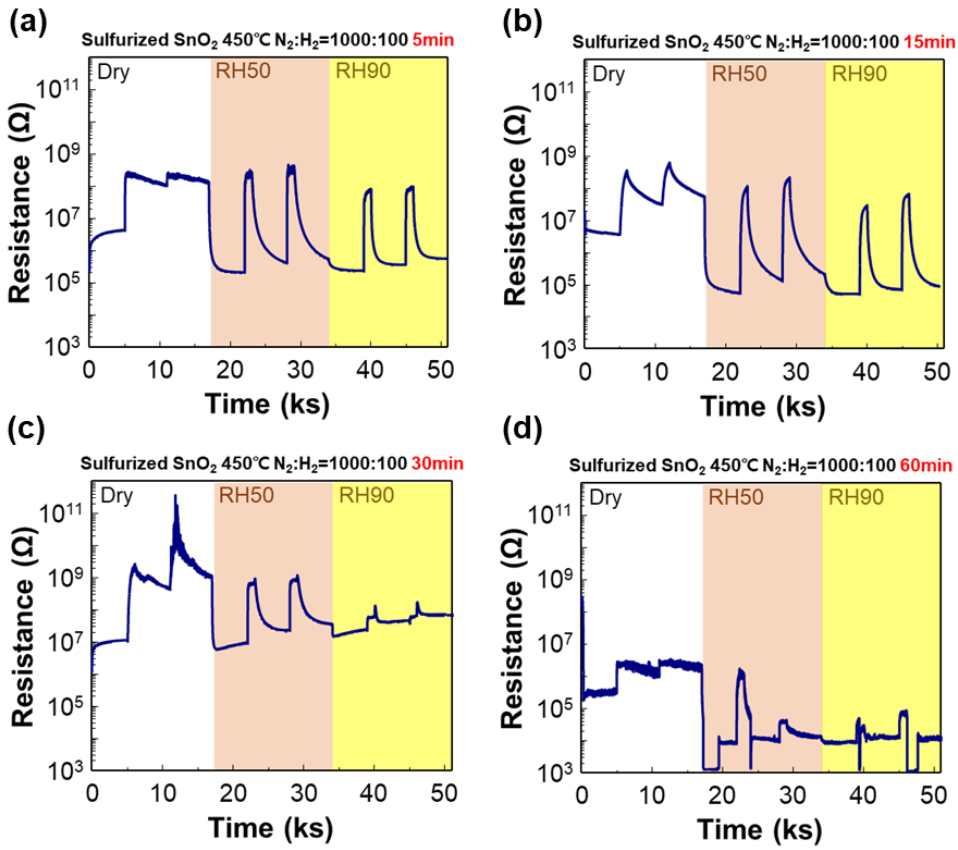

Figure 4.27. Response curves of (a) 5, (b) 15, (c) 30 and (d) 60 min-sulfurized SnO_2 NRs at 450 ℃ under N_2:H_2 ratio of 1000:100 toward 1 ppm NO_2 at room temperature in dry, RH50, and RH90 condition.

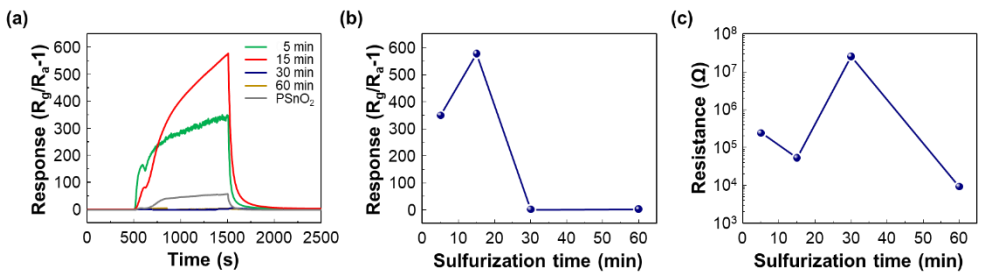

Figure 4.28. (a) Gas response curves of the pristine and 5, 15, 30 and 60 min-sulfurized SnO_2 NRs at 450 ℃ under N_2:H_2 ratio of 1000:100 toward 1 ppm NO_2 at room temperature in RH90 condition. (b) Gas response and (c) resistance as a function of sulfurization time.

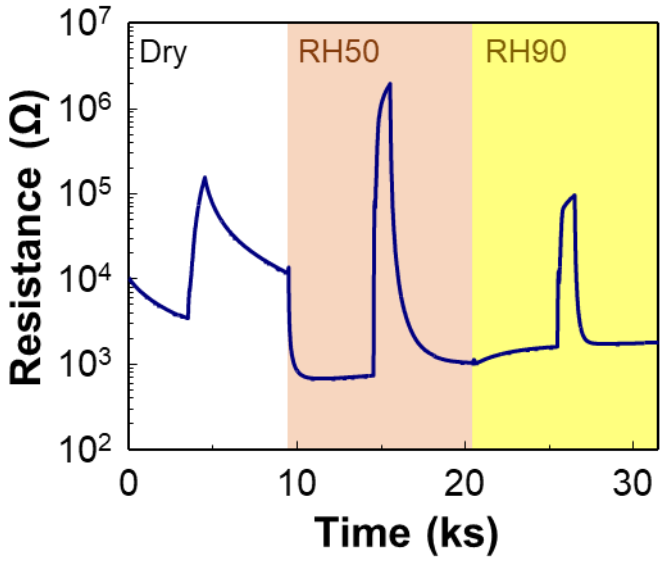

Figure 4.29. Response curves of P-SnO_2 NRs toward 1 ppm NO_2 at room temperature in dry, RH50, and RH90 condition.

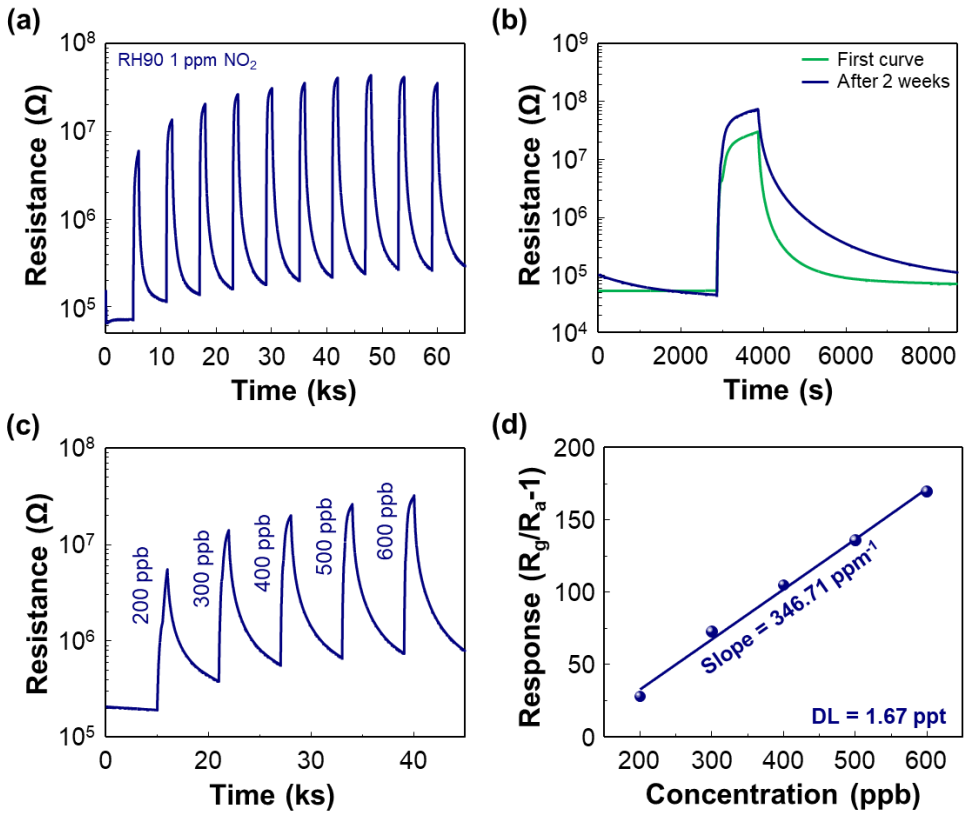

Figure 4.30. (a) Gas response curves toward multiple exposures to 1 ppm NO_2 under RH90 at room temperature. (b) Comparison of gas response curves to 1 ppm NO_2 under RH90 at room temperature before and after 2 weeks storage. (c) Gas response curves toward low concetration NO_2 under RH90 at room temperature and (d) corresponding calibration of responses for the calculation of theoretical detection limit.

The selectivity behavior of S-SnO_2 NRs toward various gases was investigated. The decoration of noble metal catalysts including Au, Pd, and Co is an effective strategy to obtain diverse selectivity toward various gases. Through e-beam evaporation, 2 nm of Au, Pd, and Co were deposited on S-SnO_2 NRs to induce self-agglomeration into nanoparticles, leading to the uniform decoration of noble metal catalysts.[24] The photograph of the fabricated 2 by 2 sensor array is shown in Figure 4.31a. Each electrode pad is connected to the sample holder with Au wire. The fabricated gas sensors were exposed to 1 ppm NO_2, 1 ppm H_2S, 10 ppm NH_3, 10 ppm H_2, and 10 ppm C_2H_5OH under RH90 at room temperature. Firstly, the gas responses for bare S-SnO_2 were summarized in Figure 4.31b. While gas responses to other gases were less than 10, that toward NO_2 was as high as 583.1, indicating extremely selective behavior to NO_2. The gas responses by Au, Pd, and Co-decorated S-SnO_2 NRs were collected and plotted with normalized responses (response of catalysts-decorated S-SnO_2 divided by that of bare S-SnO_2 NRs) as shown in Figure 4.31c-f. Au decoration on S-SnO_2 NRs further enhanced the gas response toward NO_2 but was not effective in detection of other gases. Pd and Co decoration were effective in the detection of H_2 and NH_3, respectively. However, none of them improved gas response toward H_2S and C_2H_5OH.

The gas responses of P-SnO_2 NRs and S-SnO_2 NRs to 1 ppm NO_2 at room temperature under RH90 are summarized in Figure 4.32a to interpret the exact mechanism of the promising NO_2 detection performance. At RH50, P-SnO_2 exhibited better gas responses over S-SnO_2 but worse gas responses at RH90. To interpret it, DFT calculation was conducted to compare binding energies to SnO_2 and

SnS_2 for H_2O and NO_2.In Figure 4.32b and c, binding energies for H_2O physisorption and chemisorption on SnO_2 and SnS_2 are calculated and illustrated with the most favorable lattice configurations. For SnO_2, H_2O chemisorption (-1.99 eV) is preferred to H_2O physisorption (-1.34 eV), indicating H_2O is dissociated into H and OH to get bound to SnO_2 surface. For SnS_2, H_2O physisorption (-0.82 eV) is dominant over H_2O chemisorption (+1.48 eV), indicating molecular H_2O is adsorbed on SnS_2 surface. In Figure 4.32d and e, binding energies for NO_2 adsorption on SnO_2 and SnS_2 at either dry and humid conditions are calculated and illustrated with the most favorable lattice configurations. For both materials, the existence of chemisorbed H and OH from H_2O played a critical role for stronger adsorption of H_2O, but SnS_2 cannot take advantage of it since H_2O chemisorption is calculated not to happen in SnS_2 from the previous calculation. Although S-SnO_2 NRs have both SnS and SnS_2, the calculations were conducted only on SnS_2 but still these results can help to understand precise adsorption behaviors at the surface of S-SnO_2 NRs. The results for SnS_2 are strongly related to S-SnO_2 NRs and can be regarded as properties of S-SnO_2 NRs in terms of understanding the mechanisms. Therefore, in dry condition, SnS_2 has a little bit higher binding energy of NO_2 (0.83 eV) than SnO_2 (-0.60 eV), which corresponds to a little bit higher gas response as shown in Figure 4.32a. At RH50, H_2O starts to get adsorbed through chemisorption on P-SnO_2 NRs (-1.99 eV) and physisorption on S-SnO_2 NRs (-0.82 eV). Under moderate humidity, chemisorbed H_2O-assisted NO_2 adsorption is dominant for P-SnO_2 NRs (-1.52 eV) while direct NO_2 adsorption occurs for S-SnO_2 NRs with lower binding energy (-0.83 eV), leading to much higher gas response for P-SnO_2 NRs at RH50. However,

in RH90, all chemisorbed H_2O are covered with further adsorbed molecular H_2O over chemisorbed H_2O, leaving only a few available OH and H for NO_2 adsorption, resulting in extremely low gas response for P-SnO_2 NRs (58.375). On the other hand, SnS_2 has almost the same binding energies for both H_2O (-0.82 eV) and NO_2 (-0.83 eV), indicating a competitive relationship between H_2O and NO_2. As a result, even in RH90, S-SnO_2 NRs have a capacity of NO_2 adsorption leading to less decreased gas response (583.27) compared to that in RH50. In summary, S-SnO_2 NRs provided active sites for NO_2 adsorption even at extremely high humidity conditions according to DFT calculation and that resulted in promising gas sensing properties demonstrated in this study.

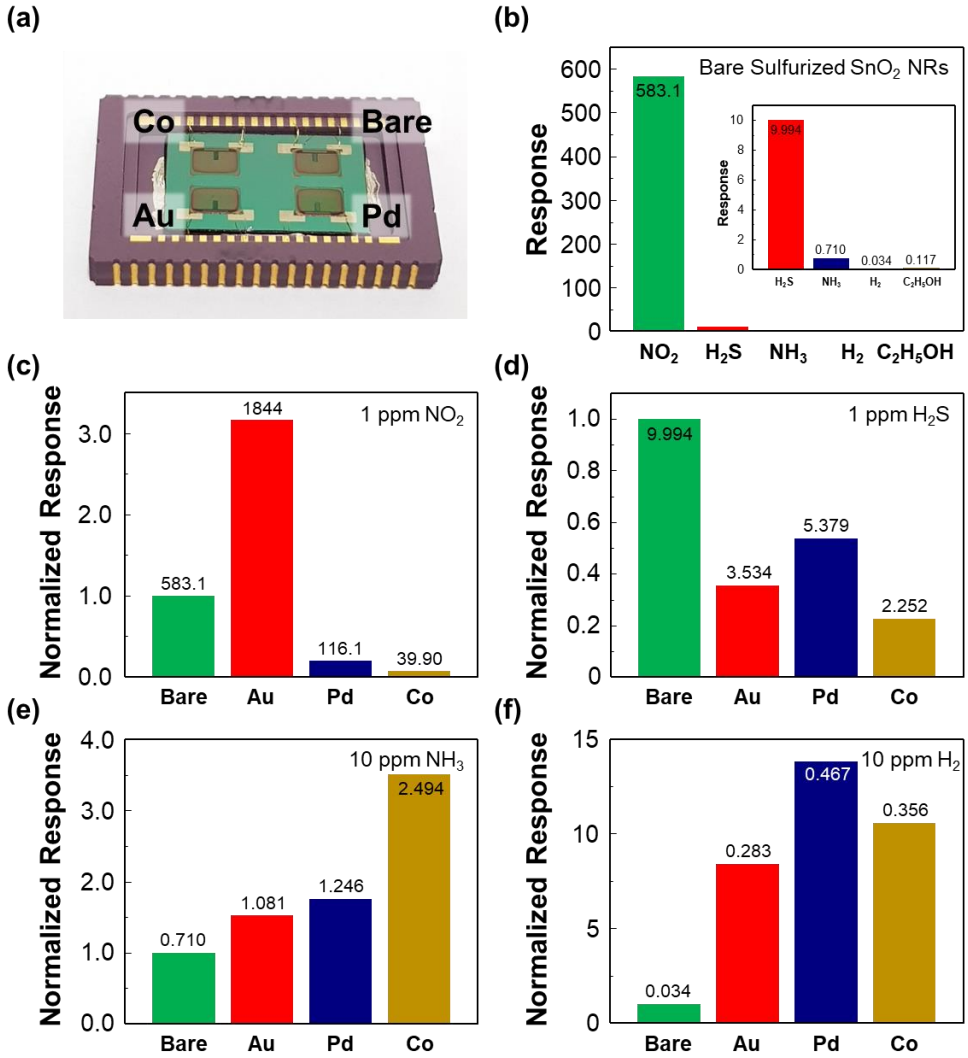

Figure 4.31. (a) Photograph of bare S-SnO_2 NRs and Co-, Au-, Pd-decorated S-SnO_2 NRs on 2 by 2 sensor array substrate. (b) Gas responses of bare S-SnO_2 NRs toward five different gases (NO_2, H_2S, NH_3, H_2, C_2H_5OH) and inset magnifies gas responses with lower value. (c-f) Normalized gas responses of bare S-SnO_2 NRs and Co-, Au-, Pd-decorated S-SnO_2 NRs toward (c) 1 ppm NO_2, (d) 1 ppm H_2S, (e) 10 ppm NH_3, (f) 10 ppm H_2 under RH90 at room temperature.

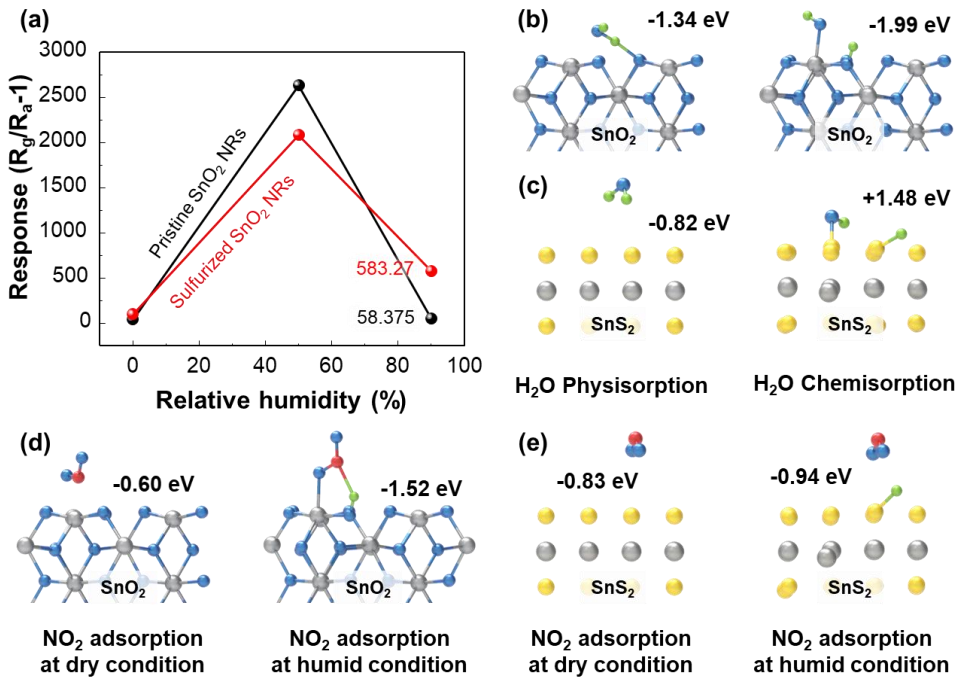

Figure 4.32. (a) Gas response of P-SnO_2 NRs and S-SnO_2 NRs toward 1 ppm NO_2 under different relative humidity at room temperature. (b-c) DFT calculation results on binding energy between (b) SnO_2 and H_2O, (c) SnS_2 and H_2O for physisorption and chemisorption cases. (d-e) DFT calculation results on binding energy between (d) SnO_2 and NO_2, (e) SnS_2 and NO_2 at dry and humid conditions.

4.3.4. Conclusion

We demonstrated a novel type of gas sensors based on sulfurized SnO_2 1D nanostructures with precisely controlled sulfurization parameters. The fabricated sulfurized SnO_2 NRs exhibited a superior gas sensing performance toward 1 ppm NO_2 with excellent recovery under the highly humid condition of 90% relative humidity at room temperature. Moreover, the decoration of noble metal catalysts (Au, Pd, and Co) on sulfurized SnO_2 nanorods resulted in a diverse selectivity toward various gases including H_2S, NH_3, H_2, and C_2H_5OH. We strongly believe that this study can provide a new perspective for nanostructures with surface treatments for the detection of target gas under the highly humid conditions at room temperature and further be applied to the examination of exhaled breath.

4.3.5. References

[1] P. A. Ubel, D. A. Comerford, E. Johnson, *Obstet. Gynecol. Surv.* **2015** 70(6), 373-375.

[2] M. Fleischer, E. Simon, E. Rumpel, H. Ulmer, M. Harbeck, M. Wandel, C. Fietzek, U. Weimer, H. Meixner, *Sens. Actuat. B−Chem.* **2002**, 83(1-3), 245-249.

[3] H. G. Moon, Y.-S. Shim, D. H. Kim, M. Jeong, J. Y. Jung, S. M. Han, J. K. Kim, J.-S. Kim, H.-H. Park, J.-H. Lee, H. L. Tuller, S.-J. Yoon, H. W. Jang, *Sci. Rep.* **2012**, 2, 588.

[4] E. Mansour, R. Vishinkin, S. Rihet, W. Saliba, F. Fish, P. Sarfati, H. Haick, Sens. Acutat. *B−Chem.* **2020**, 304(1), 127371.

[5] M. Bouhadid, N. Redon, H. Plaisance, J. Desbrieres, S. Reynaud, *Macromol. Symp.* **2008**, 268, 9-13.

[6] H.-J. Kim, J.-H. Lee, *Sens. Actuat. B−Chem.* **2014**, 192, 607.

[7] P. Srinivasan, D. Prakalya, B. G. Jeyaprakash, *J. Alloy. Compd.* **2020**, 819, 152985.

[8] Q. Geng, X. Lin, R. Si, X. Chen, W. Dai, X. Fu, X. Wang, *Sens. Actuat. B−Chem.* **2012**, 174, 449-457.

[9] Y. G. Song, Y.-S. Shim, J. M. Suh, M.-S. Noh, G. S. Kim, K. S. Choi, B. Jeong, S. Kim, H. W. Jang, B.-K. Ju, C.-Y. Kang, *Small* **2019**, 15, 1902065.

[10] A. Favard, X. Yan, S. Anguille, P. Moulin, J.-L. Seguin, K. Aguir, M. Bendahan, *Sens. Transducers* **2018**, 222(6), 6-11,

[11] K. Lee, R. Gatensby, N. McEvoy, T. Hallam, G. S. Duesberg, *Adv. Mater.* **2013**, 25, 6699-6702.

[12] X. Liu, T. Ma, N. Pinna, J. Zhang, *Adv. Funct. Mater.* **2017**, 27, 1702168.

[13] S. Shi, R. Hu, E. Wu, Q. Li, X. Chen, W. Guo, C. Sun, X. Hu, D. Zhang, J. Liu, *Nanotechnology* **2018**, 29, 435502.

[14] G. Radovsky, R. Popovitz-Biro, M. Staiger, K. Gartsman, C. Thomsen, T. Lorenz, G. Seifert, R. Tenne, *Angew. Chem.* **2011**, 123, 12524-12528.

[15] J. Wang, G. Lian, Z. Xu, C. Fu, Z. Lin, L. Li, Q. Wang, D. Cui, C.-P. Wong, *ACS Appl. Mater. Interfaces* **2016**, 8, 9545-9551.

[16] J. M. Suh, Y.-S. Shim, D. H. Kim, W. Sohn, Y. Jung, S. Y. Lee, S. Choi, Y. H. Kim, J.-M. Jeon, K. Hong, K. C. Kwon, S. Y. Park, C. Kim, J.-H. Lee, C.-Y. Kang, H. W. Jang, *Adv. Mater. Technol.* **2017**, 2, 1600259.

[17] J. M. Suh, W. Sohn, Y.-S. Shim, J.-S. Choi, Y. G. Song, T. L. Kim, J.-M. Jeon, K. C. Kwon, K. S. Choi, C.-Y. Kang, H.-G. Byun, H. W. Jang, *ACS Appl. Mater. Interfaces* **2017**, 10, 1050-1058.

[18] Y. Zheng, T. Zhou, C. Zhang, J. Mao, H. Liu, Z. Guo, *Angew. Chem.* **2016**, 128, 3469-3474.

[19] J. J. M. Vequizo, M. Ichimura, *Jpn. J. Appl. Phys.* **2012**, 51, 10NC38.

[20] Y.-S. Shim, K. C. Kwon, J. M. Suh, K. S. Choi, Y. G. Song, W. Sohn, S. Choi, K. Hong, J.-M. Jeon, S.-P. Hong, S. Kim, S. Y. Kim, C.-Y. Kang, H. W. Jang, *ACS Appl. Mater. Interfaces* **2018**, 10, 31594-31602.

[21] K. C. Kwon, J. M. Suh, T. H. Lee, K. S. Choi, K. Hong, Y. G. Song, Y.-S. Shim, M. Shokouhimehr, C.-Y. Kang, S. Y. Kim, H. W. Jang, *ACS Sens.* **2019**,

4, 678-686.

[22] K. N. Kang, K. Godin, E.-H. Yang, *Sci. Rep.* **2015**, 5, 13205

[23] J. Li, Y. Lu, Q. Ye, M. Cinke, J. Han, M. Meyyappan, *Nano Lett.* **2003**, 3, 929-933.

[24] Y.-S. Shim, H. G. Moon, D. H. Kim, L. Zhang, S.-J. Yoon, Y. S. Yoon,C.-Y. Kang, H. W. Jang, *RSC Adv.* **2013**, 3, 10452.

Chapter 5

3D Metal Oxide Nanostructures

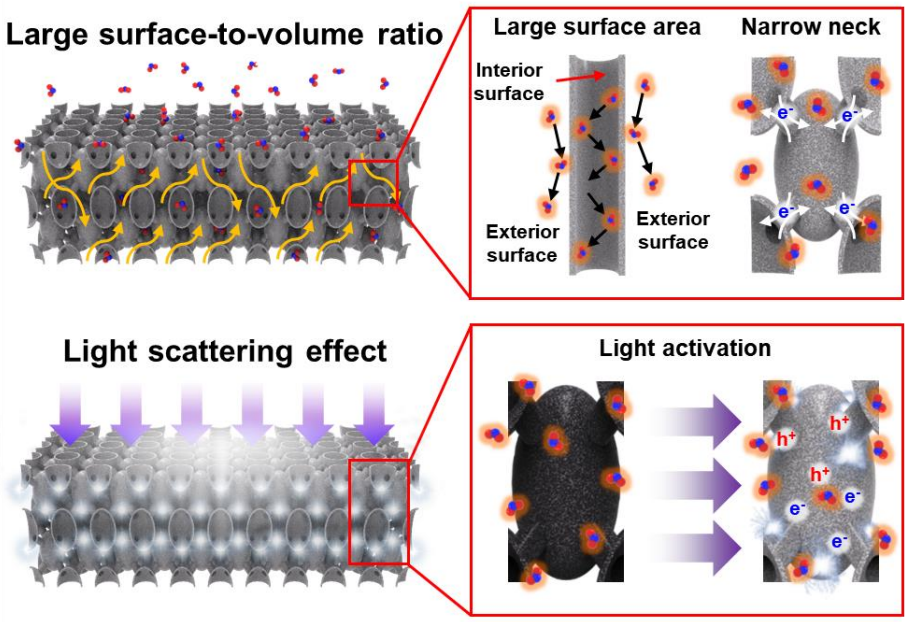

Manuscripts under preparation

5.1. 3D titanium dioxides

5.1.1. Introduction

The semiconductor or chemoresistive-type gas sensor based on metal oxides has been one of the most intensively studied and developed technology with a growing demand from the Internet of Everything (IoE) market.[1] The IoE application requires the gas sensors to exhibit a low power consumption for their installation in mobile devices, not to mention an excellent gas-sensing performance. To achieve low power consumption, the heaters, more than anything else, should be removed from the current chemoresistive-type gas sensor structures. The heaters operate at approximately 200–400 °C with temperature uncertainty, thermally degrade the neighboring electronic components during operation, raise issues upon the miniaturization of device, and have also been a primary reason for the low reliability of the current sensor systems.[2] Therefore, numerous studies have focused on discovering alternative materials capable of operation at near room-temperature[3, 4] or other chemical-activation routes for sensing that consume less power than the thermal heaters.[5, 6]

One of the notable research directions in low temperature gas sensors is the use of light sources, particularly light-emitting diodes (LEDs), for energy-efficient activation of semiconducting sensor materials. Light sources with higher energy than the bandgap energy of the semiconductors can excite internal charge carriers to participate in the chemical reaction and accelerate the interaction between the semiconductor and the gas molecules. The previous studies on light-activated gas sensors have repeatedly reported relatively improved gas responses and faster

recovery characteristics under light illumination.[7, 8] Considering the high-performance requirements for gas sensors in IoE applications, further modifications of the sensory materials, other than just relying on their bulk properties, should precede the full utilization of the given light energy. In response, there have been numerous efforts reported to date with various strategies for light-activated gas sensors including i) heterojunction engineering[9], ii) noble metal decoration[10], iii) utilization of non-oxide materials (2D, inorganic perovskites)[11, 12], iv) incorporation of plasmonic nanoparticles[13], and v) development of effective nanostructures[14]. Despite their active gas-sensing performances, few studies suggest the possibility of improving the sensor's performance by adding structural factors to maximize the optoelectronic properties of the light-activated gas sensors.

In this study, we systematically designed highly periodic three-dimensional (3D) thin-shell TiO_2 nanostructures (denoted as "3D TiO_2") whose symmetry is body-centered tetragonal (BCT) and the shell thickness is 30 nm. The nanostructure can make unique use of light by multiple scatterings within the optimal total thickness of 6 μm, which is first proven by finite element analysis (FEA) of the electromagnetic field (E-field) distribution over 3D TiO_2 by unit cell modeling. The optimized light-scattering effects by 3D thin-shell TiO_2 on the enhancement of NO_2 gas-sensing performance were verified through the measurement of resistance change. The thin-shell and film thickness of 3D TiO_2 were precisely controlled for the optimization (thin-shell thickness from 30 to 100 nm and film thickness from 3 to 15 μm, respectively). As a result, the fabricated 3D TiO_2 exhibited significantly increased light absorption compared to that of the planar TiO_2 thin film, with a

thickness of 6 μm, yielding dramatically enhanced light-activated gas responses with faster and complete recovery characteristics toward 5 ppm NO_2. More interestingly, the gas response was further enhanced up to 4 times under a relative humidity of 50% due to the neutralization of hydroxyl groups under UV illumination.[15, 16] Finally, a notable observation is that the fabricated 3D TiO_2 exhibited light-activated characteristics even under visible light illumination due to the defective nature of the atomic layer deposition (ALD)-coated TiO_2 thin-shell, such as O vacancies, interstitial Ti, and carbon residues. To the best of our knowledge, there has been no systematic attempt to design a structural platform for the effective utilization of the illuminated LED light (< 800 μW) for gas sensor applications operating in a highly humid environment at room temperature. The light-activated, ultra-sensitive (theoretical detection limit down to ~202 parts per trillion (ppt) level) gas-sensing properties of 3D TiO_2 proven by the optical simulation in this study will certainly open a new perspective toward future chemoresistive-type gas sensors operating at room temperature without any heating unit.

5.1.2. Experimental procedures

Fabrication of a 3D polymeric template on an IDEs substrate. Interdigitated electrodes (IDEs) with 5 μm spacing were fabricated by depositing platinum (100 nm) and titanium (30 nm) on a SiO_2/Si substrate using photolithography and e-beam evaporation techniques.[3, 4] After cleaning the IDEs substrate by dipping and sonicating in acetone and ethanol in sequence, the substrate was dried and treated by air plasma (CUTEMP, Femtoscience) at a flow rate of 45 s.c.c.m., pressure of 40 mTorr, and power of 60 W for 120 s. Afterward, the edges of the electrodes were selectively concealed with commercial adhesives (3M tape) to avoid contamination during the following photoresist (PR) spin-casting step. First, a thin layer (~2 μm) of the PR (SU-8 2, Microchem) was spin-coated onto a plasma-treated substrate as an adhesion-promoting layer. After removing the pre-deposited tape, the adhesion layer was patterned into the open-window structure at the electrode pattern and hard-baked on a hot plate at 210 °C for 5 min. Then, a relatively thick layer (~10 μm) of the PR (SU-8 10, Microchem) was spin-coated on the adhesion layer again. The PR layer was carefully soft baked in 2 steps: 65 °C for 30 min and 95 °C for 30 min. Then, the substrate was induced to soft contact with a conformal phase mask designed to have a square array of holes (with a diameter of ~480 nm, a depth of ~400 nm, and a periodicity of ~600 nm).[17, 20, 24, 25] After the 3D nanopatterning process using the proximity-field nanopatterning (PnP) technique, conventional lithographic procedures including a post-baking step with a 65 °C hot plate for 7 min, a developing step (SU-8 developer, Microchem), and a rinsing step with deionized water and a drying process were performed.

Material conversion into a 3D TiO_2. A thin TiO_2 layer (0–100 nm) was conformally deposited on the pre-fabricated 3D template by atomic layer deposition (ALD) technique at 90 °C (Atomic-Classic, CN1 Co., Ltd).[24] Tetrakis-dimethyl-amido titanium (TDMAT) (UP Chemical) was used as a precursor and H_2O was used as a reactant, respectively. The deposition cycles were controlled to modify the deposited TiO_2 thickness with the deposition rate of approximately 0.75 Å per cycle. Then, the 3D polymeric template was placed in a furnace at 500 °C to obtain the 3D TiO_2 hollow nanostructure by thermally decomposing the 3D polymeric template and annealing the TiO_2 in a single thermal step.

Characterization. The morphologies of the 3D TiO_2 samples were characterized using field-emission scanning electron microscopy (FESEM, S-4800, Hitachi) operating at an accelerating voltage of 5–10 kV. The structural features of the fabricated 3D TiO_2 were obtained by field emission transmission electron microscopy (FE-TEM) using a Tecnai F20 (FEI Company) at an accelerating voltage of 200 kV. The crystallographic analysis of the samples was performed by high-resolution powder X-ray diffraction (XRD) using SmartLab (RIGAKU). Elemental mapping measurements were collected via energy dispersive spectroscopy (EDS, Magellan 400, FEI). The absorbance measurements were performed using UV-VIS spectrophotometry (SolidSpec-3700, Shimadzu). The spectra of photoluminescence (PL) were collected by a fluoro-spectrophotometer using an F-7000 (Hitachi) with an excitation source for Xe lamp (150 W). The chemical bonding and core-electron binding energy of the 3D nanostructured TiO_2 film samples were investigated by in-situ X-ray photoelectron spectroscopy (XPS) using an Axis-Supra (Kratos) with

automated monochromatic X-ray source. To compensate for the surface charging, we used a low energy electron flood gun (charge neutralizer).

Gas-sensing measurement. The gas-sensing measurement was conducted in a quartz tube with a gas injection line and a ventilation line. The breadboard with commercial LEDs (PL-UVA521CMK (Photron Co., Ltd), 513SBC3Z, 513UGC, 513UYC3 (Britestone)) was placed on top of a quartz tube with the help of plastic support. The gas injection was conducted using an automated mass flow controller repeating a sequence of dry air for 3000 s and the target gas (balanced with dry air, Sinjin Gases) for 500 s. The gas flow was maintained at 1000 s.c.c.m. throughout the whole measurements. The gas responses toward the target gas were precisely measured at a DC bias voltage of 5.0 V using a source meter (Keithley 2400). Additional experimental details about the gas-sensing measurement can be found in our previous works.[31]

Simulations. The optical modeling and calculations were performed by commercial finite differential time-domain (FDTD, Lumerical Solutions Ltd.). The PnP process with a square array phase mask (period: 600 nm) was simulated in the set of a 5-nm cubic mesh and refractive indices of each component (PDMS mask: 1.4, SU-8 photoresist: 1.66) with a 355 nm plane wave source assuming periodic boundaries. The resulting 3D interference image in photoresist was modeled to the 3D SU-8 polymer template by the level-set method to possess a fill factor of 50%.[18] To consider the TiO_2 thin-shells on the template by ALD deposition, the thin-shell structures were generated to conformally cover the SU-8 template with the measured refractive index by ellipsometry. For the optical responses of the TiO_2 optical mazes,

the electrical intensity field distributions of each model were calculated to visualize and further analyzed to select intensities only in the TiO_2 thin-shell regions.

5.1.3. Results and discussion

Design concept and fabrication of 3D TiO_2 chemoresistors

Figure 5.1a presents the overall experimental approach used in this study and the developed highly periodic 3D TiO_2. In brief, the optic system with a conformal phase mask for 3D nanofabrication, which generates light diffraction and interference in a proximity-field, provides 3D periodic intensity distribution of the incident light through a pre-fabricated photopolymer thin film by the Talbot effect (Figure 5.2).[17-20] The details can be found in the experimental section. Compared to other competing techniques such as self-assembly, electrospinning, and many other bottom-up methods, one of the notable technical advantages of this microelectromechanical system-integrated method is the direct patterning of 3D scaffolds on the electrodes.[21-23] Therefore, the further TiO_2 deposition using ALD can be done without any additional transferring steps, which generally lead to poor contact issues between the electrodes and the deposited functional materials.[24, 25] To apply 3D TiO_2 to gas sensors, we fabricated 3D TiO_2 on a SiO_2/Si substrate with Pt interdigitated electrodes (IDEs). Figure 5.1b shows schematic illustrations and photographs of the 3D TiO_2 on the IDEs-patterned SiO_2/Si substrates and gas-sensing measurement system, respectively. The active area is 1 mm × 1 mm and the number of interdigitated fingers is 20 with 5 μm interspacing. The cross-sectional scanning electron microscopy (SEM) images of the fabricated 3D TiO_2 on a SiO_2/Si substrate with Pt IDEs show the direct construction of the sensory material without any structural degradation, such as collapse and delamination (Figure 5.1c). For a clear observation of 3D TiO_2, cross-sectional high-resolution transmission electron

microscopy (HR-TEM) images were carefully obtained, and they present a highly periodic BCT symmetry of 3D TiO_2 (inset in Figure 5.1c). In addition, the in-situ elemental mapping by energy-dispersive X-ray spectroscopy (EDS) proves the uniform deposition of TiO_2 over the complicated 3D nanostructure during the ALD procedure, resulting in a monolithic 3D TiO_2 nanostructure (Figure 5.1d and e). After the heating process for the polymeric template removal and the annealing of TiO_2 in a single step,[24, 25] 3D TiO_2 resulted in the anatase phase. Likewise, the observed lattice fringes of 0.17 nm for *d*(105) and 0.27 nm for *d*(110) with a fast Fourier transform (FFT) pattern in Figure 5.1f indicate the anatase phase (JCPDS #21-1272) and correspond to the X-ray diffraction (XRD) analysis in Figure 5.1g.

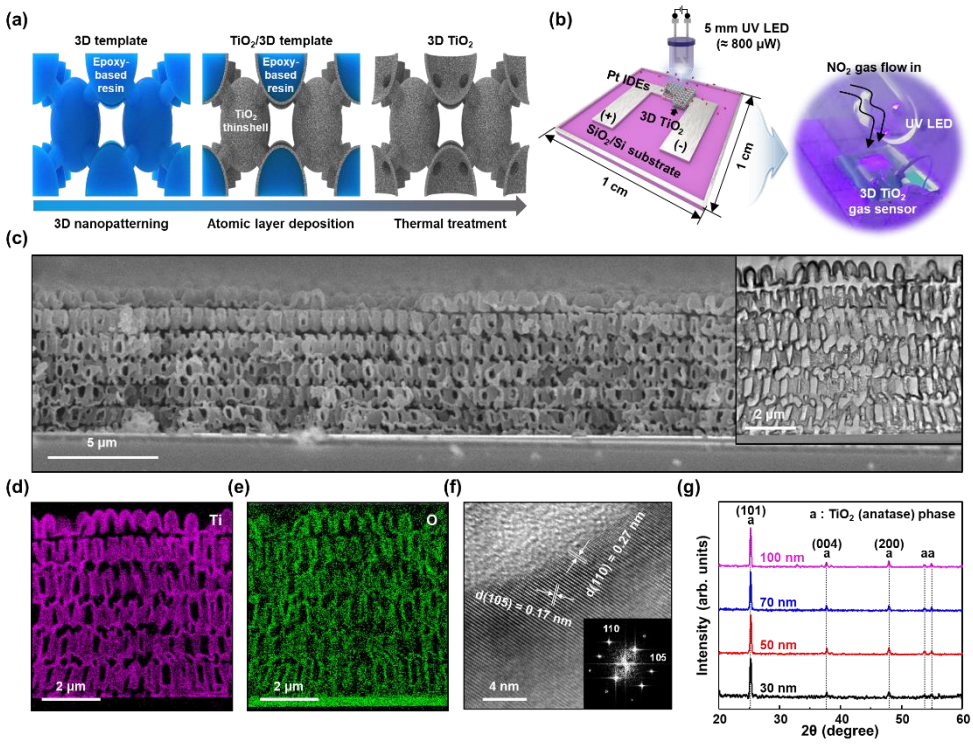

Figure 5.1. Design concept of and fabrication procedures for 3D TiO_2 gas sensor. (a) Schematic illustrations showing the fabrication of a 3D TiO_2 gas sensor. (b) Schematic illustrations and photographs of 3D TiO_2 on the Pt IDEs patterned SiO_2/Si substrates and gas-sensing measurement system. (c) Cross-sectional SEM image of 3D TiO_2 with 100 nm TiO_2 thin-shell thickness. The inset shows the HR-TEM image of 3D TiO_2. In-situ elemental mapping results of (d) Ti and (e) O from the inset in (c) analyzed by EDS. (f) FFT and lattice fringe images of the 3D TiO_2. (g) Comparison of XRD results of the fabricated 3D TiO_2 with thin-shell thicknesses of 30, 50, 70, and 100 nm, respectively.

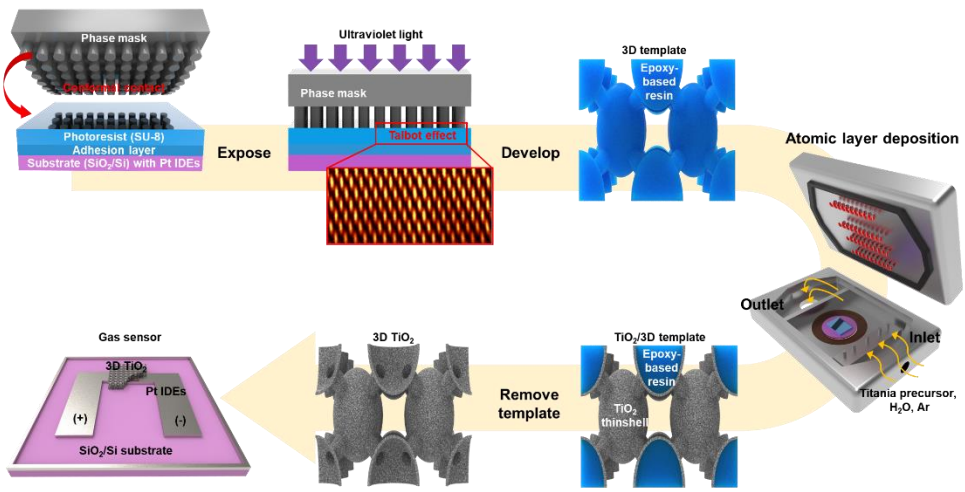

Figure 5.2. Schematic illustrations for the overall fabrication process of 3D TiO_2 gas sensor.

Geometric advances of 3D TiO_2 for the light-activated chemoresistors

The resultant 3D periodic porous TiO_2 thin-shell network with the periodicity of 600 nm offers the three major factors for ideal gas-sensing performance: (i) utility factor, (ii) transducer function, and (iii) receptor function.[26] As the BCT unit cell of 3D TiO_2 consists of two types of embodiments, a hollow ellipsoid core (center) and eight inter-necks connecting with the neighboring 1/8 parts of the hollow ellipsoids, these thin-shell inter-necks allow the target gases to access both the exterior and interior surfaces of the 3D nanostructure (utility factor). It is noted that A. Sanger *et al.* reported the contribution of the hollow tubular structure with high-aspect-ratio to the significant improvement of the NO_2 molecule collision frequency, which directly corresponds with our unprecedented enhancement of the sensing performances.[27] In addition, the inter-necks in the unit cell also play an important role in the enhancement of the semiconducting performances of the TiO_2. The junctions between the TiO_2 thin-shell networks narrow the conduction channels with double-Schottky junctions originated from the depletion layers formed by the adsorption of ionized oxygen from the air.[28] The inter-necks further narrow the conduction channel, which significantly enhances a transducer function that contributes to more efficient modulation of the electrical resistance upon exposure to target gases (Figure 5.3a). For the receptor function, the light-scattering effects induced by the 3D nanostructure facilitate the significantly improved photo-activation of 3D TiO_2, resulting in numerous photo-generated electron–hole pairs for reaction with NO_2 molecules (Figure 5.3b).

To effectively utilize the large surface area of 3D TiO_2 in terms of the light-

activated gas sensors, the total film thickness of 3D TiO_2 and the TiO_2 thin-shell thickness should be carefully defined. As the film thickness of 3D TiO_2 increases, the numerous repeatedly existing layers in the tri-axial directions of 3D TiO_2 gradually inhibit both an effective photo-activation and gaseous passage. The thicker TiO_2 thin-shell reduces the inter-space between TiO_2 thin-shells and the porosity of the overall film, while its light absorption characteristics are expected to be improved due to the decreased transmittance through the TiO_2 nanostructure. To find an optimal combination of the above conditions, the film thickness of 3D TiO_2 was controlled as 3, 6, and 15 μm, and the TiO_2 thin-shell thickness was controlled as 30, 50, 70, and 100 nm. The dependencies of both thicknesses of 3D TiO_2 in terms of light-scattering effects were investigated by defining the unit cell models for each case using a commercial finite-difference time-domain (FDTD) simulation software (Lumerical). It is noteworthy that this numerical approach for finding the optimal conditions was valid owing to the exceptional structural uniformity, which is one of the distinctions of this work. Overall simulation data dependent on the film thickness of the 3D TiO_2 (Figure 5.4a) confirms that the E-field enhancement in UV by the 3D TiO_2 is significantly improved owing to its optical maze-like architecture that leads to effective UV light absorption. In particular, the periodicity of the structure and the refractive index mismatch at the interfaces between air (refractive index ≈ 1) and TiO_2 (refractive index ≈ 1.7) induce the light interference resulting in an active E-field enhancement along the 3D nanostructure. In fact, there is a saturation point to utilize the incident UV light through 3D TiO_2 because of the considerable scattering effect from a thicker 3D nanostructure. For example, the degree of E-field

enhancement in UV intensively increases until the total thickness reached 6 μm, but beyond that total thickness, this effect is saturated at approximately 70% (Figure 5.4b). It indicates that the excess of film thickness over 6 μm is not useful for photo-activation. Thus, there should be an effective total thickness between 3 and 15 μm, and it is controlled as 6 μm in this work.

The TiO_2 thin-shell thickness affects the effective refractive index[29] and porosity of 3D TiO_2[24], which significantly contribute to both the E-field enhancement and gas accessibility. Thus, we controlled the TiO_2 thin-shell thickness in the range from 30 nm to 100 nm by varying the deposition cycles of the ALD. The variation of light-matter interaction from the controlled TiO_2 thin-shell thicknesses generates complex E-field intensity distributions (Figure 5.3c). As the thin-shell thicknesses become thicker, the deeper regions of 3D TiO_2 have relatively weaker intensities due to decreased transmission of light. For a clear understanding of the E-field enhancement effect on UV absorption, the total sum of intensity for 3D TiO_2 (film thickness 6 μm as the function of thin-shell thickness) and planar TiO_2 thin films are calculated with each thin-shell thickness (Figure 5.5). The light confinement is defined as the sum of intensity values in 5-nm cubic voxels consisting of TiO_2 regions in the FDTD simulation. As the thin-shell thickness increases, the increments in total E-field are more prominent for 3D TiO_2 than for the planar TiO_2 films, which is originated from the porosity differences between the planar TiO_2 thin films and 3D TiO_2. Therefore, the overall light-activated gas-sensing performance should be determined considering both the nanostructural and light-scattering effects.

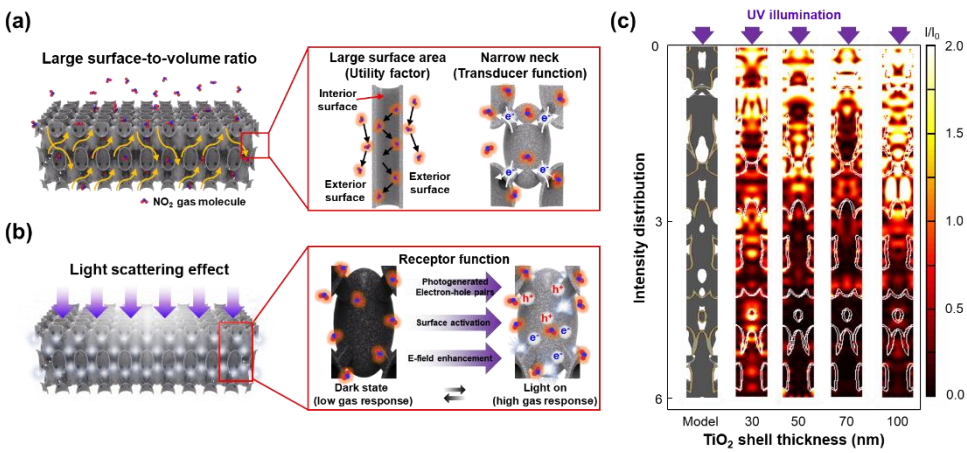

Figure 5.3. The geometric advances of 3D TiO_2 gas sensor for detecting NO_2 gas molecules. Schematic illustrations of (a) highly periodic TiO_2 nanonetworks for effective NO_2 gas permeation and (b) light-scattering effects induced from 3D nanostructures enhancing E-field of the incident UV light. (c) Comparison of the E-field intensity distributions when UV light passes through 3D TiO_2 simulated by finite element modeling as a function of TiO_2 thin-shell thickness.

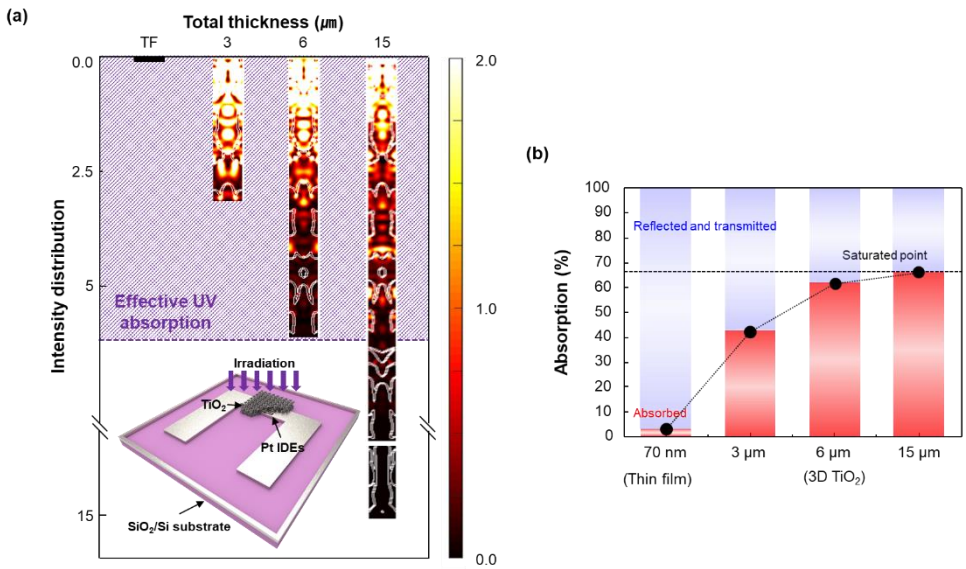

Figure 5.4. (a) Simulated depth profile of 3D TiO_2 with E-field distribution along the cross-section of the samples. (b) Calculated UV absorption depending on the total thickness of 3D TiO_2.

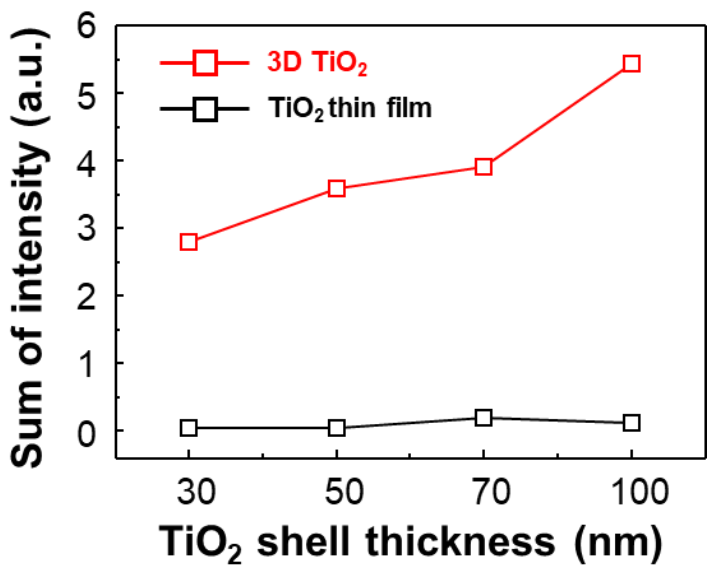

Figure 5.5. Simulated total sum of intensity for 3D TiO_2 and planar TiO_2 thin films.

Optimization of key structural factors in 3D TiO_2

After the fabrication of 3D TiO_2 using various combinations with the total film thickness of 3, 6, and 15 μm and thin-shell thickness of 30, 50, 70, and 100 nm, 3D TiO_2 was exposed to 5 ppm NO_2 under ultraviolet (UV) illumination at room temperature to investigate its gas-sensing properties. An illumination power to the sample of less than 800 μW from a commercial 5-mm UV micro-LED was sufficient to photo-activate the sensor. It is worth mentioning that no illumination result on TiO_2 chemoresistors has ever achieved high performance under this illumination condition. The extremely low energy consumption is a key factor for miniaturization and integration to IoE devices. Figure 5.6a and b show top-view and cross-sectional view of SEM images of 6 μm-thick 3D TiO_2 with 30, 50, 70, and 100 nm thin-shell thickness. A clear decrease in porosity can be verified for the thicker TiO_2 thin-shells and is expected to significantly affect the gas-sensing properties along with the light-scattering effects. Figure 5.6c-e show the gas-response curves to 5 ppm NO_2 for each 3D TiO_2. The resistance increased instantly upon the initial exposure to the NO_2, which indicates the behavior of an *n*-type semiconductor. Compared to the planar TiO_2 thin film exhibiting almost no gas response under the dark condition and a very little response under UV illumination, 3D TiO_2 exhibited significantly improved gas response and full recovery to the baseline resistance (Figure 5.7). In addition, both samples exhibited decreased base resistance under UV illumination compared to that under dark condition, which indicates the photo-generation of electron–hole pairs. The gas response can be calculated dividing the changes in saturated resistance before and after exposure to NO_2 (R_{air} and R_{gas}, respectively) by the baseline

resistance (R_{air}), expressed as ($R_{gas} - R_{air}$) / R_{air} × 100 (%).[30, 31] The gas responses of 3D TiO_2 with the different thickness combinations toward 5 ppm NO_2 under UV illumination are summarized in Figure 5.6f. The total thickness of 6 μm exhibited higher gas response for all TiO_2 thin-shell thickness conditions than that for 3D TiO_2 with 3 and 15 μm, which is well-matched with the simulation data. For example, low response with non-stability was observed for the 15-μm sample because of the considerable volume of the unexposed region at the bottom, which is regarded as a dead volume. The gas responses kept decreasing as the TiO_2 thin-shell thickness increased up to 70 nm but increased again as it went up to 100 nm. As the TiO_2 thin-shell thickness increases, the volume fraction of vacancy compared to the TiO_2 area, calculated from the top-view SEM images in Figure 5.6a, decreases as shown in Figure 5.6g, indicating less porous nanostructures and less TiO_2-gas molecule interactions. Up to 70 nm, this nanostructural effect dominates the gas-sensing properties of 3D TiO_2, but for a thicker TiO_2 thin-shell, over 70 nm, it starts to become dominated by the light-scattering effects from the complex 3D nanostructures. Thus, it is evident that both the levels of photo-activation and gas dynamics are crucial factors for the light-activated gas sensors. Although the calculated total sum of intensity was the highest for 3D TiO_2 with 100-nm thickness of thin-shell, the overall gas-sensing performance considering both the nanostructural effect and E-field enhancement was the best for the 6-μm 3D TiO_2 with 30-nm thin-shell thickness. It has a nearly 55 times higher sum of intensity compared to that of the planar TiO_2 thin film upon UV illumination, which is sufficient to take advantage of the complex 3D nanostructure designed in this study.

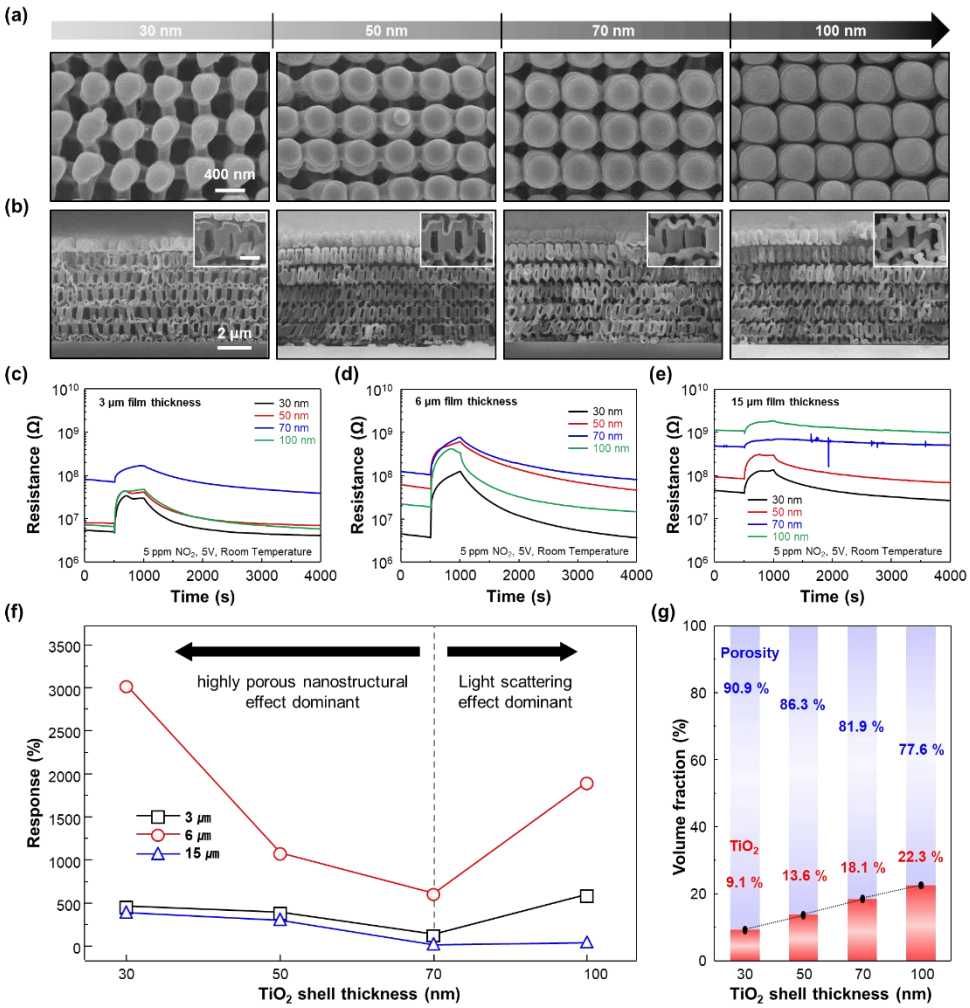

Figure 5.6. Optimization of total film thickness and TiO_2 thin-shell thickness. (a) Top-view and (b) cross-sectional SEM images of 3D TiO_2 with increasing TiO_2 thin-shell thickness: 30, 50, 70, and 100 nm. Resistance change curves of (c) 3 μm, (d) 6 μm, and (e) 15 μm film thickness of the 3D TiO_2 to 5 ppm NO_2 under UV illumination as a function of controlled TiO_2 thin-shell thickness. (f) Calculated responses of 3D TiO_2 to 5 ppm NO_2 under UV illumination with various TiO_2 thin-shell thickness and film thickness. (g) Comparison plot for the volume fraction of air and TiO_2, as a function of TiO_2 thin-shell thickness.

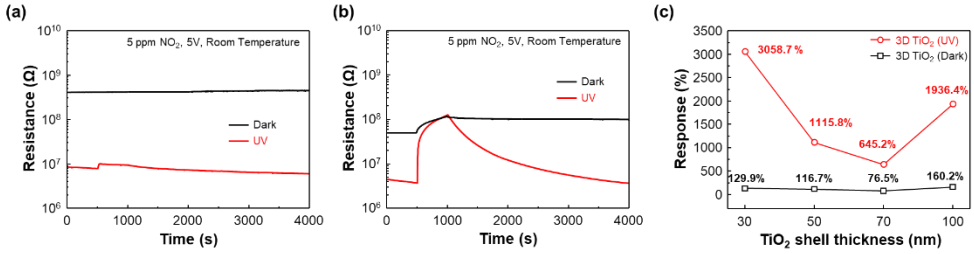

Figure 5.7. Resistance change plots of (a) planar TiO_2 thin film and (b) 3D TiO_2 with and without UV illumination. (c) Gas responses of 3D TiO_2 as a function of TiO_2 thin-shell thickness with and without UV illumination.

Super-sensitive chemoresistive response of 3D TiO_2 to NO_2 gas molecule

To verify further the gas-sensing properties such as stability and detection limit of 3D TiO_2 with a total thickness of 6 μm and a thin-shell thickness of 30 nm, the sample was exposed to multiple pulses of NO_2 at various concentrations under UV illumination (Figure 5.8a). The gas responses showed an excellent linear relationship (slope = 2.75 ppm^{-1}) with gas concentration as described in Figure 5.8b. Although the lowest concentration of NO_2 tested in this work was 400 ppb, the theoretical detection limit can be calculated by extrapolating the linear relationship to where the signal to noise ratio is equal to 3.[32] Accordingly, the theoretical detection limit was calculated to be as low as 202 ppt, which may be advantageous for detection of extremely low concentration of target gases, such as those of explosives and narcotics. In Figure 5.8c, the measurement under a relative humidity of 50% (RH50) revealed the exceptional gas response of 3D TiO_2 to 5 ppm NO_2, as high as 12200%. While exhibiting promising gas responses under UV illumination both at dry and humid conditions, a relatively slow response time (the time required to reach 90% of the saturated resistance under gas exposure, 428 s) might need to be improved for certain applications. In that case, some amount of external heating can accelerate the kinetics of gas molecules to yield faster response time, but this study will focus on light activation without any external heating.

The selectivity toward five different gas species (50 ppm CH_3COCH_3, H_2, C_2H_5OH, NH_3, and 5 ppm NO_2) was tested on the 3D TiO_2 sensor. As shown in Figure 5.8d, exceptionally selective detection of NO_2, even with the lowest concentration, was achieved. It is well-known that the absorbed ionized oxygen

species (O_2^-, O^-, O^{2-}) on the surface of TiO_2 are the key to the electronic interaction between 3D TiO_2 and the gas molecules. Although oxygen molecules ($O_{2(gas)}$) have very low chance to be ionized on the surface of TiO_2 at room temperature[28], several studies have experimentally proved the existence of ionized oxygen species ($O_{2(ads)}^-$) on the surface of metal oxides even at room temperature by comparing conductance under either pure O_2 and pure N_2 without any photo-activation.[7, 15] Under UV illumination, the $O_{2(ads)}^-$ recombine with photogenerated holes ($h_{(photo)}^+$) and become desorbed from the surface ($h_{(photo)}^+ + O_{2(ads)}^- \leftrightarrow O_{2(gas)}$). The desorption of $O_{2(gas)}$ is considered advantageous to gas-sensing properties as it supplies the available reactive sites of 3D TiO_2, and the trapped electrons result in the decrease in resistance.[7, 33] Meanwhile, some of the photo-generated electrons ($e_{(photo)}^-$) can interact with the adsorbed $O_{2(gas)}$ to form photo-generated oxygen ions ($O_{2(gas)} + e_{(photo)}^- \leftrightarrow O_{2(photo)}^-$). It should be clear that $O_{2(ads)}^-$ desorption would overwhelm $O_{2(photo)}^-$ adsorption. Otherwise, the resistance would not decrease under UV illumination.[15] The $O_{2(photo)}^-$ is expected to be weakly bound to 3D TiO_2 and have higher reactivity compared to the naturally chemisorbed $O_{2(ads)}^-$, which is thermally stable and less reactive at room temperature.[34] Therefore, NO_2 sensing and recovery are more likely to be accelerated under UV illumination ($NO_2 + O_{2(photo)}^- \leftrightarrow NO_{2(ads)}^- + O_{2(gas)}$) as demonstrated in the measurement. As there are already excessive photo-generated electrons trapped in TiO_2, reducing gases like CH_3COCH_3, H_2, C_2H_5OH, and NH_3, which produce electrons when interacting with $O_{2(photo)}^-$, are less likely to exhibit as much improved gas response as an oxidizing gas such as NO_2, which consumes electrons, resulting in high NO_2 selectivity. When in humid condition, H_2O

molecules become ionized on the surface of TiO_2 ($H_2O_{(gas)} + Ti + O_{lattice} \leftrightarrow (Ti^+ - OH^-) + (OH)_{lattice}^+ + e^-$)[35]. Following exposure to NO_2, NO_2 is adsorbed on the surface of 3D TiO_2 ($(Ti^+ - OH^-) + (OH)_{lattice}^+ + e^- + NO_2 \leftrightarrow (Ti^+ - NO_2^-) + H_2O + O_{lattice}$).[16] Under UV illumination, the neutralization of the hydroxyl groups (OH^-) is possible with photo-generated holes ($OH^- + h_{(photo)}^+ \leftrightarrow OH_{(photo)}$), and $OH_{(photo)}$ can accelerate the above reaction and further improve NO_2 gas response.[15] That is the most-widely accepted conduction mechanism under a moderate amount of humidity[16, 36, 37] other than the hopping charge transport mechanism. When compared to other previously reported light-activated gas sensors, the exceptional sensing performances of the fabricated 3D TiO_2 greatly exceed them, as shown in Figure 5.8e.[38-46] In terms of IoE application, the humidity-boosted gas-sensing capabilities can significantly contribute to the development of disease diagnosis devices, which collect disease biomarkers from humid sources such as the exhaled breath.

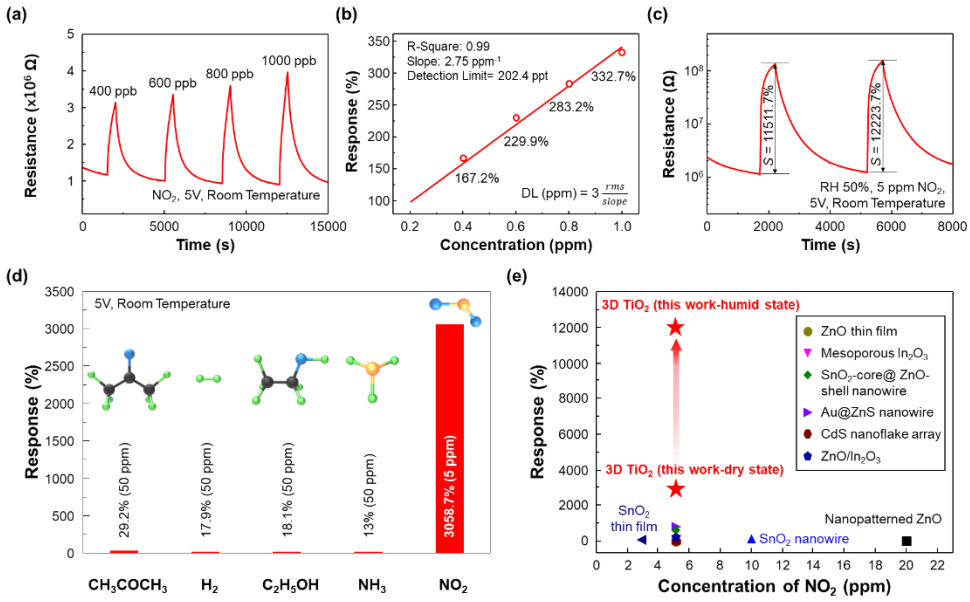

Figure 5.8. Sensing performances of 3D TiO_2 gas sensors with 30 nm thin-shell thickness and 6 μm film thickness. (a) Response curves to different NO_2 concentrations at 5.0 V. (b) Linear fit of the responses as a function of NO_2 concentration at 5.0 V. (c) Resistance curve of the fabricated gas sensors under exposure of humidity of 50%. (d) Selective NO_2-sensing performance of 3D TiO_2 gas sensors. (e) Comparison of gas-sensing properties with those in other previous works.

Extension of photo-activation range from UV to visible light range

Interestingly, 3D TiO_2 exhibited unconventional absorbance at wavelengths longer than that corresponding to the intrinsic bandgap of TiO_2, 3.2 eV, while the planar TiO_2 thin film did not exhibit any absorbance at wavelengths longer than 380 nm (Figure 5.9a). As the thin-shell thickness of 3D TiO_2 increases up to 100 nm, the unconventional absorbance of the visible light is significantly enhanced (>2,900% for the 100 nm thickness at a wavelength of 600 nm), which is mainly due to the large portion of incident light not reaching the UV/vis spectra detector because 3D TiO_2 is an effective optical maze for light scattering. However, when exposed to 5 ppm NO_2 under visible light, 3D TiO_2 exhibited improved gas-sensing properties compared to that under dark conditions, which should not happen considering the bandgap energy of TiO_2 (Figure 5.9b). The gas responses to red light (680 nm), green light (532 nm), and blue light (470 nm) were 295.9%, 103.5%, and 370.8%, respectively (Figure 5.9c), due to its structure-induced light-scattering effect, which was not proportional to the wavelength of the incident light.[47] In other words, the visible light was actually absorbed by 3D TiO_2 for the photo-activation.

To interpret these unusual photo-activation behaviors of 3D TiO_2, further FDTD simulation was carried out to calculate the E-field enhancement for each wavelength and transmission depending on the diffracted orders (Figure 5.10). As shown in Figure 5.9d, the E-field enhancement under blue light was the highest, that under red light was the second-highest, and that under green light was the lowest, which corresponds to the sequence in gas response data. In other words, the defective nature of the ALD-deposited 3D TiO_2 provided an intermediate energy state in the

forbidden zone of the 3D TiO_2 band structure, and the excellent light scattering of 3D TiO_2 leading to E-field enhancement provided a high possibility of light absorption through the intermediate energy state. This would not have happened in a planar TiO_2 thin film, which does not have any E-field enhancement. To verify the intermediate energy state of 3D TiO_2, photoluminescence (PL) spectra were acquired for the optimized 3D TiO_2 (with total thickness of 6 μm and thin-shell thickness of 30 nm) and unconventional photoluminescence at several wavelengths was identified (Figure 5.11), indicating actual absorption of visible light wavelengths. Among the many deconvoluted peaks, the predominant emission peak at below 400 nm indicates the slightly shifted main peak of the TiO_2 anatase phase, and the many extra peaks explain the intermediate energy states that correspond to various visible wavelengths (Figure 5.9e). According to the calculated intermediate energy states, the band diagram of 3D TiO_2 was reconstructed as shown in Figure 5.9f. It can be explained by considering the interstitial Ti defects (Ti_i) and oxygen vacancies (V_{oS}) during the ALD procedure.[48] According to the O 1*s* scan of the X-ray photoelectron spectroscopy (XPS) analysis, there are three major deconvoluted peaks originating from the lattice (530 eV), -OH (531 eV), and C=O (532 eV), respectively (Figure 5.12). Comparing with the planar TiO_2 thin film, the suppression of the C=O peak for 3D TiO_2 proves the increase in the O vacancies. In addition, the inevitable existence of the carbon atom during the heat treatment provides the additional intermediate band states that ensure that the unique activation range is extended from UV to the wide band of the visible light range. Thus, the inherent defects of 3D TiO_2 facilitated light-activated gas-sensing properties, even at the visible wavelength,

with the help of the superb light-scattering effects of the intricate 3D TiO_2 nanostructures. This implies that the photoactivation under the desired wavelength could also be achieved without any attributes from defects, but through the systematic design of the band structure through various strategies such as catalyst decoration or formation of heterojunctions.

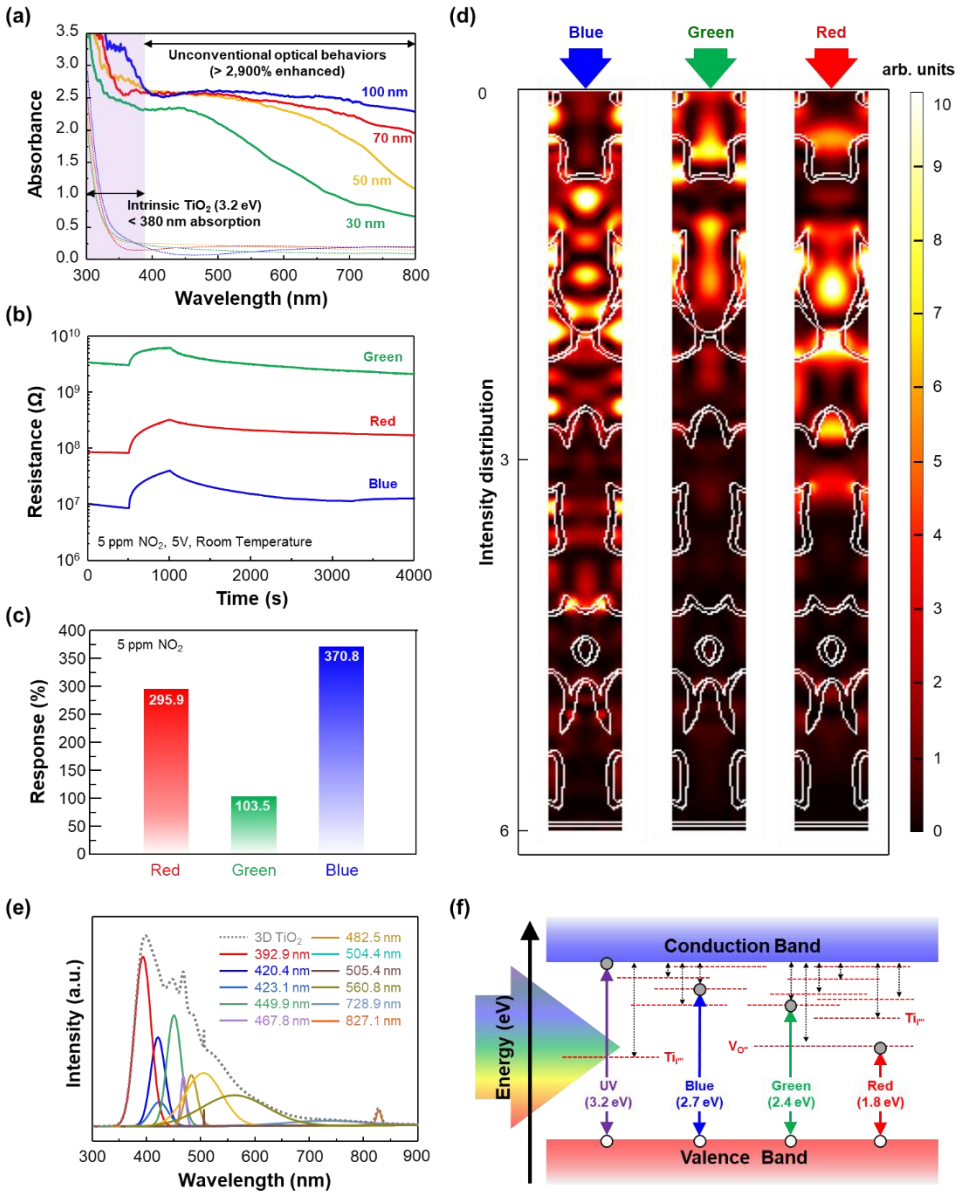

Figure 5.9. Unconventional NO_2 gas response of 3D TiO_2 under the illumination of visible light. (a) UV/vis absorbance spectra of 3D TiO_2 and planar TiO_2 thin films with different thin-shell thicknesses. (b) Resistance change curves and (c) gas responses of the 3D TiO_2 to 5 ppm of NO_2 under LED irradiation of visible lights (red, green, and blue). (d) Calculated E-field intensity distributions through 3D TiO_2 under illumination of various visible lights such as blue (470 nm), green (532 nm), and red (680 nm), respectively. (e) Photoluminescence spectra with λ_EX = 295 nm for 3D TiO_2. (f) Reconstructed band diagram of 3D TiO_2 from the measured PL data in (e).

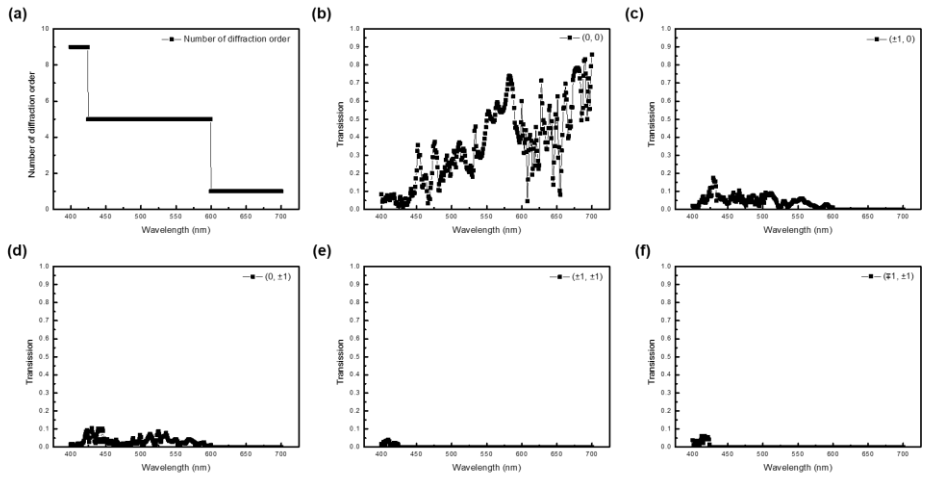

Figure 5.10. Calculated transmissions through 3D TiO_2. (a) Number of diffraction order through 3D TiO_2 and transmission at (b) 0th order, (c–d) 1st order, and (e–f) 2nd order of the diffracted lights.

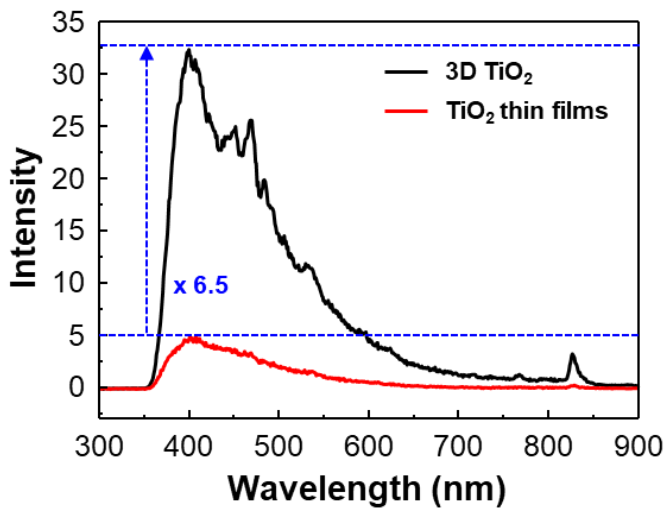

Figure 5.11. Comparison of PL spectra between 3D TiO_2 and planar TiO_2 thin film.

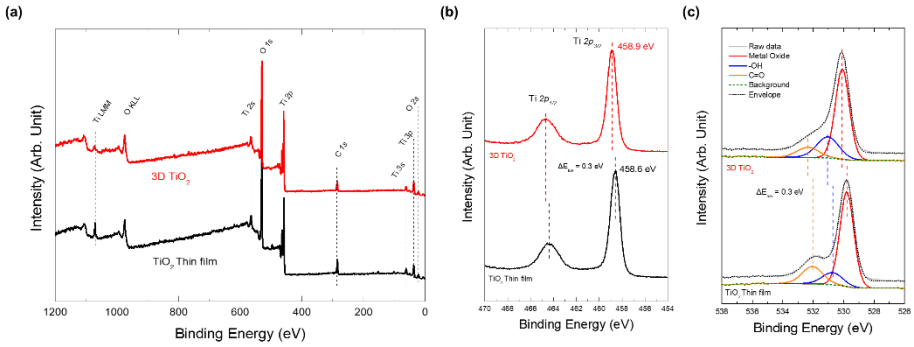

Figure 5.12. (a) Survey, (b) Ti 2*p* spectra, and (c) O 1*s* spectra from XPS analysis of the chemical bonding for 3D TiO_2 and the planar TiO_2 thin film.

5.1.4. Conclusion

In conclusion, the realization of the highly periodic 3D TiO_2 is of fundamental significance to state-of-the-art light-activated gas sensor applications. The high degree of freedom to optimize the governing structural factors of the chemoresistive materials offers new design opportunities to overcome the bottlenecks of the conventional method for light-activated gas sensors, which hinder the simultaneous employment of the gas dynamics and light utilization. Owing to its perfect structural uniformity, the two crucial factors, TiO_2 thin-shell thickness and total thickness, were precisely optimized as 30 nm and 6 μm, respectively, based on the FEA analysis. With these attributes, the open porous, interconnected 3D nanonetwork leads to significantly enhanced utilization of the incident light, which was experimentally verified with the exceptional NO_2-sensing performance having a theoretical detection limit of ~200 ppt and stable operation at room temperature using low power consumption of a micro-LED, less than 800 microwatts, for irradiation of not only UV but also visible lights. A remaining technical barrier in the application of this technology is the fabrication of denser 3D structures in terms of optical and chemical activities. The explorations of other symmetries, such as the wood-pile structure, and material designs for controlling the band structure represent other promising research directions for the future. Therefore, the concept of the MEMS integrable 3D nanopatterning that can generate the effective light-activated gas sensor platform presented in this work holds great promise as a rational strategy for developing general oxide-based gas sensors in IoE applications.

5.1.5. References

[1] R. A. Potyrailo, *Chem. Rev.* **2016**, 116, 11877-11923.

[2] R. Prajesh, N. Jain, A. Agarwal. *Microsyst. Technol.* **2016**, 22, 2185-2192.

[3] Y.-S. Shim, K. C. Kwon, J. M. Suh, K. S. Choi, Y. G. Song, W. Sohn, S. Choi, K. Hong, J.-M. Jeon, S.-P. Hong, S. Kim, S. Y. Kim, C.-Y. Kang, H. W. Jang, *ACS Appl. Mater. Interfaces* **2018**, 10, 31594-31602.

[4] K. C. Kwon, J. M. Suh, T. H. Lee, K. S. Choi, K. Hong, Y. G. Song, Y.-S. Shim, M. Shokouhimehr, C.-Y. Kang, S. Y. Kim, H. W. Jang, *ACS Sens.* **2019**, 4, 678-686.

[5] Y. H. Kim, S. J. Kim, Y.-J. Kim, Y.-S. Shim, S. Y. Kim, B. H. Hong, H. W. Jang, *ACS nano* **2015**, 9, 10453-10460.

[6] H. Chen, Y. Chen, H. Zhang, D. W. Zhang, P. Zhou, J. Huang, *Adv. Funct. Mater.* **2018**, 28, 1801035.

[7] B. Liu, Y. Luo, K. Li, H. Wang, L. Gao, G. Duan, *Adv. Mater. Interf.* **2019**, 6, 1900376.

[8] M. M. Hashemi, A. Nikfarjam, H. Hajghassem, N. Salehifar, *J. Phys. Chem. C* **2020**, 124, 322-335.

[9] H. Wang, L. Zhoi, Y. Liu, F. Liu, X. Liang, F. Liu, Y. Gao, X. Yan, G. Lu, *Sens. Actuat. B−Chem.* **2020**, 305, 127498.

[10] Q. A. Drmosh, A. H. Hendi, M. K. Hossain, Z. H. Yamani, R. A. Moqbel, A. Hezam, M. A. Gondal, *Sens. Actuat. B−Chem.* **2019**, 290, 666-675.

[11] H. Chen, M. Zhang, R. Bo, C. Barugkin, J. Zheng, Q. Ma, S. Huang, A. W. Y. Ho-Baillie, K. R. Catchpole, A. Tricoli, *Small* **2018**, 14, 1702571.

[12] D. Gu, X. Wang, W. Liu, X. Li, S. Lin, J. Wang, M. N. Rumyantseva, A. M. Gaskov, S. A. Akbar, *Sens. Actuat. B−Chem.* **2020**, 305, 127455.

[13] Y. Zhou, C. Zou, X. Lin, Y. Guo, *Appl. Phys. Lett.* **2018**, 113, 082103.

[14] J. Cui, L. Shi, T. Xie, D. Wang, Y. Lin, *Sens. Actuat. B−Chem.* **2016**, 227, 220-226.

[15] L. Liu, X. Li, P. K. Dutta, J. Wang, *Sens. Actuat. B−Chem.* **2013**, 185, 1-9.

[16] Y. G. Song, Y.-S. Shim, J. M. Suh, M.-S. Noh, G. S. Kim, K. S. Choi, B. Jeong, S. Kim, H. W. Jang, B.-K. Ju, C.-Y. Kang, *Small* **2019**, 15, 1902065.

[17] D. Cho, J. Park, J. Kim, T. Kim, J. Kim, I. Park, S. Jeon, *ACS Appl Mater Inter.* **2017**, 9, 17369-17378.

[18] J. K. Hyun, J. Park, E. Kim, L. J. Lauhon, S. Jeon, *Adv. Opt. Mater.* **2014**, 2, 1213-1220.

[19] J. Park, K.-I. Kim, K. Kim, D.-C. Kim, D. Cho, J. H. Lee, S. Jeon, *Adv. Mater.* **2015**, 27, 8000-8006.

[20] S. Jeon, J.-U. Park, R. Cirelli, S. Yang, C. E. Heitzman, P. V. Braun, P. J. A. Kenis, J. A. Rogers, *P. Natl. Acad. Sci. USA* **2004**, 101, 12428-12433.

[21] J. Zhang, Y. Li, X. Zhang, B. Yang, *Adv. Mater.* **2010**, 22, 4249-4269.

[22] M.-H. Seo, J.-Y. Yoo, M.-S. Jo, J.-B. Yoon, *Adv. Mater.* **2020**, 1907082.

[23] S.-J. Choi, I.-D. Kim, *Electron. Mater. Lett.* **2018**, 14, 221-260.

[24] C. Ahn, J. Park, D. Kim, S. Jeon, *Nanoscale* **2013**, 5, 10384-10389.

[25] S. Cho, C. Ahn, J. Park, S. Jeon, *Nanoscale* **2018**, 10, 9747-9751.

[26] N. Yamazoe, G. Sakai, K. Shimanoe, *Catal. Surv. Asia* **2003**, 7, 63-75.

[27] A. Sanger, S. B. Kang, M. H. Jeong, M. J. Im, I. Y. Choi, C. U. Kim, H. Lee,

Y. M. Kwon, J. M. Baik, H. W. Jang, K. J. Choi, *Adv. Sci.* **2018**, 5, 1800816.

[28] N. Barsan, U. Weimar, *J. Electroceram.* **2001**, 7, 143-167.

[29] X. A. Zhang, A. Bagal, E. C. Dandley, J. Zhao, C. J. Oldham, B.-I. Wu, G. N. Parsons, C.-H. Chang, *Adv. Func. Mater.* **2015**, 25, 6644-6649.

[30] J.-H. Lee, *Sens. Actuat. B−Chem.* **2009**, 140, 319-336.

[31] J. M. Suh, Y.-S. Shim, D. H. Kim, W. Sohn, Y. Jung, S. Y. Lee, S. Choi, Y. H. Kim, J.-M. Jeon, K. Hong, K. C. Kwon, S. Y. Park, C. Kim, J.-H. Lee, C.-Y. Kang, H. W. Jang, *Adv. Mater. Technol.* **2017**, 2, 1600259.

[32] J. Li, Y. Lu, Q. Ye, M. Cinke, J. Han, M. Meyyappan, *Nano Lett.* **2003**, 3, 929-933.

[33] R. Kumar, N. Goel, M. Kumar, *ACS Sens.* **2017**, 2, 1744-1752.

[34] X. Tian, X. Yang, F. Yang, T. Qi, *Colloid. Surface. A* **2019**, 578, 123621.

[35] N. D. Chinh, C. Kim, D. Kim, *J. Alloy. Compd.* **2019**, 778, 247-255.

[36] P. Srinivasan, D. Prakalya, B. G. Jeyaprakash, *J. Alloy. Compd.* **2020**, 819, 152985.

[37] Q. Geng, X. Lin, R. Si, X. Chen, W. Dai, X. Fu, X. Wang, *Sens. Actuat. B−Chem.* **2012**, 174, 449-457.

[38] E. Comini, G. Faglia, G. Sberveglieri, *Sens. Actuat. B−Chem.* **2001**, 78, 73-77.

[39] E. Espid, F. Taghipour, *Sens. Actuat. B−Chem.* **2017**, 241, 828-839.

[40] B. Fabbri, A. Gaiardo, A. Giberti, V. Guidi, C. Malagu, A. Martucci, M. Sturaro, G. Zonta, S. Gherardi, P. Bernardoni, *Sens. Actuat. B−Chem.* **2016**, 222, 1251-1256.

[41] S.-W. Fan, A. K. Srivastava, V. P. Dravid, *Sens. Actuat. B−Chem.* **2010**, 144, 159-163.

[42] H.-Y. Li, J.-W. Yoon, C.-S. Lee, K. Lim, J.-W. Yoon, J.-H. Lee, *Sens. Actuat. B−Chem.* **2018**, 255, 2963-2970.

[43] S. Park, S. An, H. Ko, S. Lee, C. Lee, *Sens. Actuat. B−Chem.* **2013**, 188, 1270-1276.

[44] S. Park, S. An, Y. Mun, C. Lee, *ACS Appl Mater Inter.* **2013**, 5, 4285-4292.

[45] J. D. Prades, R. Jimenez-Diaz, F. Hernandez-Ramirez, S. Barth, A. Cirera, A. Romano-Rodriguez, S. Mathur, J. R. Morante, *Sens. Actuat. B−Chem.* **2009**, 140, 337-341.

[46] T. Wagner, C.-D. Kohl, C. Malagu, N. Donato, M. Latino, G. Neri, M. Tiemann, *Sens. Actuat. B−Chem.* **2013**, 187, 488-494.

[47] J. Park, S. Yoon, K. Kang, S. Jeon, *Small* **2010**, 6, 1981-1985.

[48] F. Kayaci, S. Vempati, I. Donmez, N. Biyikli, T. Uyar, *Nanoscale* **2014**, 6, 10224-10234.

Chapter 6

Summary

The various strategies for improving gas selectivity and power consumption of chemoresistive gas sensors based on nanostructured semiconducting materials have been demonstrated in this thesis. In Chapter 3, gas sensing properties of 1-dimensional (1D) nanostructured *p*-type metal oxides having heterojunctions with either *n*-type metal oxides (*p*−*n* heterojunctions of NiO and α-Fe_2O_3) or *p*-type metal oxides (*p*−*p* heterojunctions of Co_3O_4 and NiO) were investigated. As a result, each heterojunction exhibited a promising gas selectivity to toluene (C_7H_8) and benzene (C_6H_6) with the extremely high value, respectively. In Chapter 4, gas sensing properties of TMDs including WS_2 and SnS_2 synthesized on the 1D SiO_2 nanorods template and sulfurized SnO_2 nanorods were demonstrated. As a result, TMDs synthesized on the 1D SiO_2 nanorods exhibited extremely sensitive and selective detection of nitrogen dioxide (NO_2) at room temperature, and sulfurized SnO_2 nanorods exhibited extremely sensitive and selective detection of NO_2 at room temperature under highly humid condition, respectively. In Chapter 5, gas sensing properties of 3D TiO_2 nanostructures under UV light irradiation were investigated. The systematically designed 3D TiO_2 nanostructures exhibited extremely sensitive and selective detection of NO_2 at room temperature under UV and visible light irradiation. The studies in this thesis can provide a new perspective toward the realization of human smell senses to complete electronic mimick of human five senses and real-life application of the sensors in modern life in the IoE era.

List of Publications

Participated as 1st author

[1] **J. M. Suh**†, Y.-S. Shim†, D. H. Kim, W. Sohn, Y. Jung, S. Y. Lee, S. Choi, Y. H. Kim, J.-M. Jeon, K. Hong, K. C. Kwon, S. Y. Park, C. Kim, J.-H. Lee, C.-Y. Kang, and H. W. Jang, "Synergetically Selective Toluene Sensing in Hematite Decorated Nickel Oxide Nanocorals", *Adv. Mater. Technol.* 2(3), 1600259, **2017**.

[2] **J. M. Suh**, H. W. Jang, "Fabrication of 1D Metal Oxide Nanostructures using Glancing Angle Deposition for High Performance Gas Sensors", *J. Sens. Sci. Technol.* 26(4), 228-234, **2017**.

[3] **J. M. Suh**†, W. Sohn†, Y.-S. Shim, J. S. Choi, Y. G. Song, T. L. Kim, C.-Y. Kang, H.-G. Byun, H. W. Jang, "p-p Heterojunction of Nickel Oxide Decorated Cobalt Oxide Nanorods for Enhanced Sensitivity and Selectivity toward Volatile Organic Compounds", *ACS Appl. Mater. Interfaces* 10(1), 1050-1058, **2017**.

[4] **J. M. Suh**, D. H. Kim, H. W. Jang, "Synthesis of Nanoporous Metal Oxide Films Using Anodic Oxidation and Their Gas Sensing Properties", *J. Sens. Sci. Technol.* 27(1), 13-20, **2018**.

[5] K. Zhang†, **J. M. Suh**†, J.-W. Choi, H. W. Jang, R. S. Varma, M. Shokouhimehr, "Recent Advances in the Nanocatalysts-assisted $NaBH_4$ Reduction of Nitroaromatics in water", *ACS Omega* 4(1), 483-495, **2019**.

[6] K. C. Kwon†, **J. M. Suh**†, K. S. Choi, T. H. Lee, K. Hong, Y. G. Song, Y.-S. Shim, M. Shokouhimehr, C.-Y. Kang, H. W. Jang, "Nano-grain SnS_2-coated SiO_2 Nanorods for Highly Sensitive NO_2 Sensor at Room temperature with Excellent Recovery", *ACS Sens.* 4(3), 678-686, **2019**.

[7] **J. M. Suh**†, Y.-S. Shim†, K. C. Kwon†, Y. G. Song, J.-M. Jeon, T. H. Lee, M. Shokouhimehr, C.-Y. Kang, H. W. Jang, "Au and Pd-decorated MoS_2 Gas Sensors for Enhanced Selectivity", *Electron. Mater. Lett.* 15(3), 368-376, **2019**.

[8] K. Hong†, M. Sjjadi†, **J. M. Suh**†, K. Zhang, M. Nasrollahzadeh, H. W. Jang, R. S. Varma, M. Shokouhimehr, "Palladium Nanoparticles on Assorted Nanostructured Supports: Applications for Suzuki, Heck, and Sonogashira Cross–Coupling Reactions", *ACS Appl. Nano Mater. Interfaces* 3(3), 2070-2103, **2020**.

[9] D. Cho†, **J. M. Suh**†, S.-H. Nam, S. Y. Park, M. Park, T. H. Lee, K. S. Choi, C. Ahn, H. W. Jang, Y.-S. Shim, S. Jeon, "Optically Activated 3D Thin-Shell TiO_2 for Super-sensitive Chemoresistive Responses: Toward Visible Light Activation", submitted, **2020.**

[10] **J. M. Suh**, K. C. Kwon, T. H. Lee, C. Kim, C. W. Lee, Y. G. Song, S. H. Cho, M. Shokouhimehr, C.-Y. Kang, Y.-S. Shim, D. Lee, H. W. Jang, "Edge-exposed WS_2 Nanorods for High-Performance NO_2 sensor at Room Temperature", submitted, **2020**.

Participated as contributing author

[1] J. Choi†, S. Park†, J. Lee, K. Hong, D.-H. Kim, C. W. Moon, G. D. Park, **J. Suh**, J. Hwang, S. Y. Kim, H. S. Jung, N.-G. Park, S. Han, K. T. Nam, and H. W. Jang, "Organolead Halide Perovskites for Low Operating Voltage Multilevel Resistive Switching", *Adv. Mater.* 28(31), 6562-6567, **2016**.

[2] D. H. Kim, D. M. Andoshe, Y. S. Shim, C. W. Moon, W. Sohn, S. Choi, T. L. Kim, M. Lee, H. K. Park, K. T. Hong, K. C. Kwon, **J. M. Suh**, J. S. Kim, J. H. Lee, and H. W. Jang, "Toward High Performance Hematite Nanotube Photoanodes: Charge Transfer Engineering at Heterointerfaces", *ACS Appl. Mater. Interfaces* 8(36), 23793-23800, **2016**.

[3] K. C. Kwon†, S. Choi†, K. Hong, D. M. Andoshe, **J. M. Suh**, J. H. Oh, C. Kim, K. S. Choi, S. Y. Kim, H. W. Jang, "Tungsten Disulfide Thin Film/p-type Si heterojunction photocathode for Efficient Photochemical Hydrogen Production", *MRS Commun.* 7(2), 272-279, **2017**.

[4] Y.-S. Shim†, B. Jang†, **J. M. Suh**, M. S. Noh, S. Kim, D. H. Kim, C.-Y. Kang, H. W. Jang, W. Lee, "Nanogap-controlled Pd Coating for Hydrogen Sensitive Switches and Hydrogen Sensors", *Sens. Actuat. B−Chem.* 255, 1841-1848, **2018**.

[5] D. M. Andoshe†, G. Jin†, C.-S. Lee†, C. Kim†, K. C. Kwon, S. Choi, W. Sohn, C. W. Moon, S. H. Lee, **J. M. Suh**, S. Kang, J. Park, H. Heo, J. K. Kim, S. Han, M.-H. Jo, H. W. Jang, "Directly Assembled 3D Molybdenum Disulfide on Silicon Wafer for Efficient Photoelectrochemical Water Reduction", *Adv. Sust. Sys.* 2(3), 1700142, **2018**.

[6] S. Y. Park, Y. H. Kim, S. Lee, W. Sohn, Y.-S. Shim, D. H. Kim, K. C. Kwon, **J. M. Suh**, J. E. Lee, J.-H. Lee, M. H. Lee, and H. W. Jang, "Highly Selective and Sensitive Chemoresistive Humidity Sensors Based on rGO/MoS_2 Van der Waals Composites", *J. Mater. Chem. A* 6, 5016-5024, **2018**.

[7] K. Hong†, T. H. Lee†, **J. M. Suh**, H. Kwon, J.-S. Park, H.-I. You, H. W. Jang, "Direct Observation of Surface Potential Distribution in Insulation Resistance Degraded Acceptor-doped $BaTiO_3$ Multilayer Ceramic Capacitors", *Electron. Mater. Lett.* 14(5), 629-635, **2018**.

[8] S. B. Kang†, K. C. Kwon†, K. S. Choi, R. Lee, K. Hong, **J. M. Suh**, M. J. Im, A. Sanger, I. Y. Choi, S. Y. Kim, J. C. Shin, H. W. Jang, K. J. Choi, "Transfer of Ultrathin Molybdenum Disulfide and Transparent Nanomesh Electrode onto Silicon for Efficient Heterojunction Solar Cells", *Nano Energy* 50, 649-658, **2018**.

[9] S. S. M. Bhat, **J. M. Suh**, S. Choi, S.-P. Hong, S. A. Lee, C. Kim, C. W. Moon, M. G. Lee, H. W. Jang, "Substantially Enhanced Front Illumination Photocurrent in Porous SnO_2 Nanorods/Networked $BiVO_4$ Heterojunction Photoanodes", *J. Mater. Chem. A* 6(30), 14633-14643, **2018**.

[10] M. Shokouhimehr, K. Hong, T. H. Lee, C. W. Moon, S.-P. Hong, K. Zhang, **J. M. Suh**, K. S. Choi, R. Varma, H. W. Jang, "Magnetically Retrievable

Nanocomposite Adorned with Pd Nanocatalysts: Efficient Reduction of Nitroaromatics in Aqueous Media", *Green Chem.* 20(16), 3809-3817, **2018**.

[11] D. H. Kim, T. H. Kim, W. Sohn, **J. M. Suh**, Y.-S. Shim, K. C. Kwon, K. Hong, S. Choi, J.-H. Lee, H. W. Jang, "Au Decoration of Vertical Hematite Nanotube Arrays for Further Selective Detection of Acetone in Exhaled Breath", *Sens. Actuat. B−Chem.* 274, 587-594, **2018**.

[12] Y.-S. Shim†, K. C. Kwon†, **J. M. Suh**, K. S. Choi, Y. G. Song, W. Sohn, S. Choi, J.-M. Jeon, S.-P. Hong, S. Kim, S. Y. Kim, C.-Y. Kang, H. W. Jang, "Synthesis of Numerous Edge Sites in MoS_2 via SiO_2 Nanorods Platform for Highly Sensitive Gas Sensor", *ACS Appl. Mater. Interfaces* 10(37), 31594-31602, **2018**.

[13] S. S. M. Bhat, S. A. Lee, **J. M. Suh**, S.-P. Hong, H. W. Jang, "Triple Planar Heterojunction of $SnO_2/WO_3/BiVO_4$ with Enhanced Photoelectrochemical Performance under Front Illumination", *Appl. Sci.* 8(10), 1765, **2018**.

[14] Y. G. Song, J. Y. Park, **J. M. Suh**, Y.-S. Shim, S. Y. Yi, H. W. Jang, S. Kim, J. M. Yuk, B.-K. Ju, C.-Y. Kang, "Heterojunction based on Rh-decorated WO_3 Nanorods for Morphological Change and Gas Sensor Application using Transition Effect", *Chem. Mater.* 31(1), 207-215, **2018**.

[15] K. Zhang, K. Hong, **J. M. Suh**, T. H. Lee, O. Kwon, M. Shokouhimehr, H. W. Jang, "Facile Synthesis of Monodispersed Pd Nanocatalysts Decorated on Graphene Oxide for Reduction of Nitroaromatics in Aqueous Solution", *Res. Chem. Intermediat.* 45(2), 599-611, **2019**.

[16] S. Y. Yi†, Y. G. Song†, J. Y. Park, **J. M. Suh**, G. S. Kim, Y.-S. Shim, J. M. Yuk, S. Kim, H. W. Jang, B.-K. Ju, C.-Y. Kang, "Morphological Evolution Induced through Heterojunction of W-decorated NiO nanoigloos: Synergistic Effect on High-performance Gas Sensors", *ACS Appl. Mater. Interfaces* 11(7), 7529-7538, **2019**.

[17] K. Hong, C. W. Moon, **J. M. Suh**, T. H. Lee, S.-I. Kim, S. Lee, H. W. Jang, "Daylight-induced Metal-Insulator Transition in Vanadium Dioxide", *ACS Appl. Mater. Interfaces* 11(12), 11568-11578, **2019**.

[18] K. C. Kwon, **J. M. Suh**, R. S. Varma, M. Shokouhimehr, H. W. Jang, "Electrocatalytic Water Splitting and CO_2 Reduction: Sustainable Solutions via Single-Atom Catalysts Supported on 2D Materials", *Small Methods*, 1800492, **2019**.

[19] K. Zhang, **J. M. Suh**, T. H. Lee, J. H. Cha, J.-W. Choi, H. W. Jang, R. S. Varma, M. Shoukouhimehr, "Copper Oxide-Graphene Oxide Nanocomposite: Efficient Catalyst for Hydrogenation of Nitroaromatics in Water", *Nano Convergence* 6(1), 6, **2019**.

[20] Y. G. Song†, Y.-S. Shim†, **J. M. Suh**, G. S. Kim, K. S. Choi, B. Jeong, S. Kim, H. W. Jang, B.-K. Ju, C.-Y. Kang, "Ionic-activated Chemiresistive Gas Sensors for Room-temperature Operation", *Small* 15(40), 2902065, **2019**.

[21] K. Hong†, T. H. Lee†, **J. M. Suh**, S.-H. Yoon, H. W. Jang, "Perspective and

Challenges in Multilayer Ceramic Capacitors for Next Generation Electronics", *J. Mater. Chem. C* 7, 9782-9802, **2019**.

[22] Y. H. Kim†, K. C. Kwon†, S. Kang†, C. Kim, T. Kim, S.-P. Hong, S. Y. Park, **J. M. Suh**, M.-J. Choi, S. Han, H. W. Jang, "Two-dimensional NbS_2 Gas Sensors for Selective and Reversible NO_2 Detection at Room Temperature", *ACS Sens.* 4(9), 2395-2402, **2019**.

[23] S. S. M. Bhat†, S. A. Pawar†, D. Potphode, C.-K. Moon, **J. M. Suh**, C. Kim, S. Choi, D. S. Patil, J.-J. Kim, J. C. Shin, H. W. Jang, "Substantially enhanced photoelectrochemical performance of TiO_2 nanorods/CdS nanocrystals heterojunction photoanode decorated with MoS_2 nanosheets", *Appl. Catal. B-Environ.* 259(15), 118102, **2019**.

[24] S. Choi†, C. Kim†, **J. M. Suh**, H. W. Jang, "Reduced Graphene Oxide-based Materials for Electrochemical Energy Conversion Reactions", *Carbon Energy* 1(1), 85-108, **2019**.

[25] C. W. Lee, **J. M. Suh**, H. W. Jang, "Chemical Sensors based on 2-Dimensional Materials for Selective Detection of Ions and Molecules in Liquid", *Frontiers in Chemistry* 7, 708, **2019**.

[26] S. Choi, J. Hwang, T. H. Lee, H.-H. Kim, S.-P. Hong, C. Kim, M.-J. Choi, H. K. Park, S. S. M. Bhat, **J. M. Suh**, J. Lee, K. S. Choi, S.-H. Hong, J. C. Shin, H. W. Jang, "Photoelectrochemical Hydrogen Production at Neutral pH Phosphate Buffer Solution using TiO_2 Passivated InAs Nanowire/p-Si Heterostructure Photocathode", *Chem. Eng. J.* 392(15), 123688, **2020**.

[27] H. Kim, M.-J. Choi, **J. M. Suh**, J. S. Han, S. G. Kim, Q. V. Le, S. Y. Kim, H. W. Jang, "Quasi-2D Halide Perovskites for Resistive Switching Devices with ON/OFF Ratios above 109", *NPG Asia Mater.* 12(1), 1-11, **2020**.

[28] K. Zhang, K. O. Kirlikovali, **J. M. Suh**, J.-W. Choi, H. W. Jang, R. S. Varma, O. K. Farha, M. Shokouhimehr, "Recent Advances in Rechargeable Aluminum-Ion Batteries and Considerations for Their Future Progress", *ACS Appl. Energ. Mater.* **2020**.

국문 초록

사물인터넷 (Internet of Everything) 시대의 도래와 함께 저 소비전력 고감도 가스 센서 기술에 대한 수요가 매우 증가하고 있다. 이미 인간의 수용체를 능가하는 수준의 기술력으로 모방된 다른 인간의 오감 (촉각, 시각, 청각, 미각)과 달리, 후각은 아직 오늘 날의 전자 기술로 완벽히 모방되지 못했다. 이를 극복하기 위해 다양한 가스 센서 원리가 제안되었지만 그 중에서도 저항 변화식 가스 센서가 뛰어난 센서 특성은 물론 간단한 동작 원리와 이에 따른 간단한 제작 공정 및 작은 크기로 인해 사물인터넷에 가장 적합한 후보로 주목받고 있다. 하지만, 상대적으로 부족한 가스 선택성과 높은 소비 전력은 문제로 지목되고 있으며 이를 극복하기 위한 다양한 노력이 다음과 같이 제안되고 있다: ① 나노구조체 형성, ② 촉매 장식, ③ 이종 접합 형성, ④ 대체 재료 사용 (금속 산화물, 이차원 물질, 전도성 폴리머, 또는 유기-무기 복합 페로브스카이트), 또는 ⑤ 히터가 아닌 대체 활성 에너지원 사용.

본 학위 논문에서는 저항 변화식 가스 센서의 가스 선택성과 소비 전력을 개선하기 위한 여러 가지 전략을 포함하고 있다. 본 학위 논문에 포함되는 연구에서 사용하는 저항 변화식 가스 센서는 반도체 물질 (금속 산화물과 전이 금속 칼코게나이드)의 나노구조체에 기반하고 있으며 이는 제한된 전극 영역에 극대화된 표면적을 이용한 센서 특성의

향상을 도모한다.

제 3장에서는, 저항 변화식 가스 센서의 가스 선택성을 향상시키기 위한 방법으로, p타입 금속 산화물의 1차원 나노구조체와 *p–n* 이종 접합 (NiO와 α-Fe_2O_3) 및 *p–p* 이종 접합 (Co_3O_4와 NiO)을 활용하였다. p타입 금속 산화물의 다원자가 전기적 특성은 휘발성 유기 화합물에 대한 다양한 선택성 확보에 기여할 수 있다. 그 결과, 각 이종 접합은 각각 톨루엔 (C_7H_8)과 벤젠 (C_6H_6)에 매우 뛰어난 가스 선택성을 보였다. 이러한 특성 향상은 ① 다공성 나노구조, ② 재료 자체의 촉매 효과, ③ 이종 접합 계면에서의 전하 운반체 공핍층, 그리고 ④ 이종 접합 형성 이후에 변화된 선호 결정 방향이 고르게 기여했을 것으로 판단된다.

제 4장에서는, 저항 변화식 가스 센서의 소비 전력을 향상시키기 위한 방법으로, 금속 산화물의 대체 물질로 2차원 물질을 활용하였다. 2차원 물질은 표면 에너지가 높아 저온에서의 가스 분자 흡탈착에 유리하여 상온 센서로 활용이 가능하다. 본 연구에서는 단순히 2차원 물질의 표면 에너지를 활용하는 것을 넘어, 1차원 나노구조체 템플릿을 활용하여 극대화된 표면적을 구현하여 가스 센서 특성의 향상을 목표로 하였다. 이에 첫 번째 전략으로, 전이금속 칼코게나이드 중 WS_2와 SnS_2를 1차원 SiO_2 나노구조체 위에 합성하였고, 두 번째 전략으로 미리 준비된 SnO_2 나노로드를 화학 기상 증착 장비를 통해 표면을 황화 처리하였다. 첫 번째 전략의 결과, 고감도 고선택성 이산화질소 (NO_2) 감지가 상온에서

구현되었다. 이는 다공성 구조와 함께 반응도 높은 전이금속 칼코게나이드의 엣지 영역이 SiO_2 나노로드 템플릿 상에서 성장 시 더 많이 노출되는 때문으로 확인되었다. 두 번째 전략의 결과, 고습도 환경에서 고감도 고선택성 NO_2 감지가 상온에서 구현되었다. 이는 SnO_2 나노로드 상의 수분과 결합이 우세한 영역이, 황화처리를 통해 수분과 NO_2가 경쟁적으로 결합할 수 있는 영역으로 일부 바뀌며 가능해진 것으로 확인되었다.

제 5장에서는 저항 변화식 가스 센서의 소비 전력을 향상시키기 위한 또 다른 방법으로, 히터의 대체 활성 에너지원으로 LED를 사용하였다. 비록 빛 활성 가스 센서에 대한 연구는 광범위하게 진행되고 있으나, 조사되는 빛을 충분히 활용하기 위한 센서 물질의 3차원 나노구조체에 대한 연구는 아직 미흡한 것으로 판단된다. 본 연구에서는 페이즈 마스크를 통과한 빛이 광반응성 폴리머를 투과할 때 발생하는 Talbot 효과 및 TiO_2의 원자층 증착을 이용하여 3차원 TiO_2 나노구조체를 구현하였다. 3차원 TiO_2 나노구조체의 구조적 효과와 광학적 효과가 가스 감지 특성에 기여하는 바를 FDTD 시뮬레이션과 함께 확인하였다. 그 결과, 자외선 파장의 LED 조사 하에 상온에서 고감도 고선택성 NO_2 감지가 구현되었고, 이는 LED 조사 하 전기장 증폭 영역이 극대화되도록 체계적으로 설계한 3차원 TiO_2 나노구조체에 기인한 것으로 볼 수 있다. 더 나아가, 원자층 증착 과정 중에 구현된 TiO_2의 결함들로 인해 가시광

영역에서도 흡수가 이루어져 가시광으로 활성화되는 가스 감지 특성 역시 확인할 수 있었다.

학번: 2014-22519

서 준 민